UNIVERSITÀ
DEGLI STUDI
DI TRIESTE

Dipartimento di Fisica

CORSO DI LAUREA MAGISTRALE
INTERATENEO IN FISICA

Curriculum Fisica della Materia

TESI DI LAUREA MAGISTRALE

Investigation of thermal and magnetic phase transitions in Ruthenates by Static and Time-Resolved Raman Spectroscopy

Laureando:
Giovanni Tartaglia

Relatore:
Prof. Daniele Fausti

Correlatori:
Dott. Giacomo Jarc

ANNO ACCADEMICO 2024-2025

UNIVERSITÀ
DEGLI STUDI
DI TRIESTE

Dipartimento di Fisica

CORSO DI LAUREA MAGISTRALE
INTERATENEO IN FISICA

Curriculum Fisica della Materia

TESI DI LAUREA MAGISTRALE

Studio delle transizioni di fase termiche e magnetiche nei Rutenati tramite spettroscopia Raman statica e dinamica

Laureando:
Giovanni Tartaglia

Relatore:
Prof. Daniele Fausti

Correlatori:
Dott. Giacomo Jarc

ANNO ACCADEMICO 2024-2025

CONTENTS

ABSTRACT

This thesis investigates thermal and magnetic phase transitions in ruthenate compounds ($Ca_xSr_{2-x}RuO_4$) by combining static and time-resolved Spontaneous Raman spectroscopy. Raman scattering, a powerful probe of vibrational, magnetic, and electronic excitations, can be used both as a fingerprint of the microscopic properties of matter and as an effective thermometer of collective excitations. After establishing the static Raman response of Sr_2RuO_4, Ca_2RuO_4, and three different Sr-doped Ca-based $Ca_xSr_{2-x}RuO_4$ compounds ($x = 0.1, 0.2, 0.3$ Sr doping), we identify the polarization dependence and temperature evolution of phonons, magnons, and electronic modes, revealing signatures of spin–orbital transitions, electron–phonon interactions, and structural transition across phase boundaries.

Magnetic-field-dependent Raman experiments reveal new collective phenomena in Ca_2RuO_4, including hysteretic behavior of both an emerging magnetic mode coupled to the magnetic field and an amplitude oscillation (Higgs mode) of the antiferromagnetic state. To move beyond equilibrium, a novel platform for time-resolved spontaneous Raman spectroscopy is developed, enabling measurements of out-of-equilibrium dynamics with picosecond resolution and tunable pump pulses in the near-IR and mid-IR. Using this setup, we study the antiferromagnetic state of Ca_2RuO_4 under resonant and off-resonant optical pumping with $d-d$ orbital transitions, disentangling the magnetic and vibrational relaxation channels.

Overall, this work demonstrates that Spontaneous Raman spectroscopy, extended to the ultrafast regime, provides a unique window on the interplay of lattice, spin, orbital, and electronic degrees of freedom in ruthenates. More broadly, this research paves the way for studying photo-induced phases and cavity-control of both quantum materials and strongly correlated systems. By uniquely accessing the effective temperature of excitations, Raman spectroscopy could thus give crucial insights on how light–matter interactions can steer phase transitions.

SOMMARIO

Questo lavoro di tesi indaga le transizioni di fase termiche e magnetiche nei composti a base di rutenati ($Ca_xSr_{2-x}RuO_4$) combinando spettroscopia Raman spontanea statica e risolta in tempo. Lo scatterin Raman, una potente sonda delle eccitazioni vibrazionali, magnetiche ed elettroniche, può essere utilizzata sia come impronta digitale delle proprietà microscopiche della materia, sia come termometro "efficace" delle eccitazioni collettive. Dopo aver caratterizzato la risposta Raman statica di Sr_2RuO_4, Ca_2RuO_4 e di tre composti $Ca_xSr_{2-x}RuO_4$ con diverso contenuto di Sr ($x = 0.1, 0.2, 0.3$), vengono identificate la dipendenza dalla polarizzazione e l'evoluzione in temperatura di fononi, magnoni e modi elettronici, rivelando tracce di transizioni spin–orbitali, interazioni elettrone–fonone e transizioni strutturali attraverso i confini delle transizioni di fase.

Esperimenti Raman dipendenti dal campo magnetico esterno mettono in luce nuovi fenomeni collettivi in Ca_2RuO_4, tra cui un comportamento isteretico sia di un modo magnetico emergente con il campo magnetico sia di un' oscillazione di ampiezza (modo di Higgs) dello stato antiferromagnetico. Per andare oltre lo studio all' equilibrio, è stata sviluppata una piattaforma originale di spettroscopia Raman spontanea risolta in tempo, che permette di misurare dinamiche fuori equilibrio con risoluzione dell'ordine dei picosecondi e impulsi di pompa modificabili sia nel vicino infrarosso che nel medio infrarosso. Con questo setup è stato studiato lo stato antiferromagnetico del Ca_2RuO_4 sotto eccitazione ottica risonante e non risonante, separando i diversi canali di rilassamento.

Complessivamente, questo lavoro dimostra che la spettroscopia Raman spontanea, estesa al regime ultrarapido, offre una prospettiva unica sull'interazione tra i gradi di libertà reticolari, di spin, orbitali ed elettronici nei rutenati. Più in generale, questa ricerca apre la strada allo studio di fasi fotoindotte e al controllo in cavità di materiali quantistici e di sistemi fortemente correlati. Accedendo in modo unico alla temperatura efficace delle eccitazioni, la spettroscopia Raman spontanea rivela come l'interazione luce–materia possa guidare le transizioni di fase.

INTRODUCTION

Light is fascinating. It underlies a wide range of natural phenomena essential to life: it regulates our circadian rhythms, drives photosynthesis in plants, and ultimately sustains all life on Earth. Most importantly, through its interaction with matter, light gives rise to the colors of the universe we perceive. Indeed, when light interacts with the natural world, it scatters, and its rays are captured by our "eyes"—our natural "spectroscopic tool." This "tool" enables us to see our surroundings and, as physicists, to begin to interpret them. Despite this, our eyes have limitations: they cannot resolve the microscopic structure of matter. We cannot directly observe how individual atoms are moving, how quickly they are vibrating, or how they influence one another under different conditions as when they are densely packed together in solid systems.

To probe these microscopic details, we need a different kind of "vision": **Raman spectroscopy**. Just as our eyes allow us to perceive the visible colors of objects, Raman spectroscopy reveals their hidden "microscopic colors"—the unique vibrational, magnetic, and electronics fingerprints of matter. To do so, this technique is based on one type of inelastic scattering of light, the so called– Raman Scattering. This effect happens everytime a beam of light interacts with a material. A small fraction of the quantum of light (photons) are scattered into photons with different energies. To give an idea, only $10^{-8} - 10^{-10}$ with respect to the incident ones contribute to this process. By studying their characteristic energies, it is possible to extract the specific excitations of the system and thereby to unveil its "microscopic colors".

Since in this thesis-work we focus on this technique, it is important to spend few worlds to explain why Raman spectroscopy is an *elegant* and *powerful* tool to investigate materials. It is *elegant* because the idea of the process is based simply in only two main Raman scattering processes. In the first one (Stokes), the scattered photons have lower energy than that of the incoming ones. Since the energy must be conserved, after the scattering process the system is left in an excited state. On the other hand, in the second type (Anti-Stokes), the scattered photons have higher energy and therefore excitations are annihilated in the system after the scattering mechanism. Therefore, it is easy to understand that the Anti-Stokes process is strongly dependent on whether-or not excitations are present. As an example, a crystal at $0\,\mathrm{K}$, has no excitations and thereby the Anti-Stokes will be estinguished. On the other hand, Raman spectroscopy is also *powerful* because it acts in the two following ways:

- as "finger print" of the system, giving us the information on
  - the energy of the excitations
  - the symmetry of the excitations by combining polarization dependence measurements
  - the nature of the excitations by distinguishing magnetic (magnons), vibrational (phonons), or electronic one;
- as "thermodynamic termometer" for the investigated excitations, monitoring selectively the effective population of a selected excitation.

Since its discovery by Raman in 1930 [1], Raman spectroscopy continues to be widely used, highlighting its versatility and scientific importance. In this thesis, we aim to extend the technique one step further: bringing conventional Raman spectroscopy into the **time-resolved spontaneous Raman spectroscopy** (TRSR). This allows us to extract the same information as in standard Raman spectroscopy, but on the characteristic picosecond timescales at which atoms move and out-of-equilibrium processes occur.

Our focus is on **complex systems** (or quantum materials), where macroscopic properties emerge from the delicate interplay among different degrees of freedom: vibrational, magnetic, orbital, and electronic. With TRSR, it becomes possible to track the effective temperatures of these excitations. Moreover, by simultaneously monitoring both the intrinsic properties of a system and its temperature, TRSR provides a unique tool for investigating the nature of dynamical processes in matter, allowing us to distinguish between thermal and non-thermal mechanisms.

A case study is the family of **ruthenate** compounds ($Ca_{2-x}Sr_xRuO_4$), where small changes in the crystal structure steer the material between very different electronic behaviors and give rise to a rich phase diagram. This diagram features exotic phenomena such as superconductivity, metal–insulator transitions, antiferromagnetism, Fermi-liquid behavior, and Hund-metal properties.

To implement time-resolved spontaneous Raman, one of the few examples in the world, we use a unique platform that combines ultrashort, tunable laser pulses. Our setup allows us to collect Raman spectra at different picosecond delays while exciting the system with two independent tunable pulses: one in the visible/near-IR range and the other in the mid-IR. This configuration provides complementary information in two key areas: (i) the broad and rich field of "light-induced" exotic phases—such as superconductivity [2–4], ferroelectricity [5], optical trasparency [6], and chirality [7]—and (ii) the emerging field of cavity control of quantum materials [8] both in theory [9, 10] and experiments

[11]. In both fields, the effective temperatures of selected excitations, whether driven out of equilibrium by light or placed in a strong-coupling regime by a cavity, play a crucial role in understanding the underlying mechanisms, which is accessible only through TRSR.

SUMMARY

The thesis is organized as follows:

- **Chapter 1:** introduces the Raman effect from both classical and quantum perspectives and reviews the main excitations revealed by Raman spectroscopy, with particular enphasis to magnetic excitations (magnons) and their scattering processes.
- **Chapter 2:** describes the two complementary Raman platforms used in the q4q laboratory at the Max Planck Institute for the Science of Light (Erlangen). After presenting the static spontaneous Raman setup in its two configurations (room-temperature and low-temperature magneto-Raman), we outline the time-resolved apparatus, focusing on key components such as the amplified laser system, tunable pump and probe beams, and acquisition scheme. Both setups are benchmarked with silicon measurements.
- **Chapter 3:** provides an overview of the ruthenate family, focusing on the structural and electronic properties of Sr_2RuO_4, Ca_2RuO_4, and the broader $Ca_{2-x}Sr_xRuO_4$ series, highlighting their phase diagrams and magnetic behavior.
- **Chapter 4:** presents static Raman measurements on Sr_2RuO_4, Ca_2RuO_4, and $Ca_{2-x}Sr_xRuO_4$ with $x = 0.1, 0.2, 0.3$. Room-temperature polarization studies are followed by temperature-dependent symmetry-resolved experiments, where we identify Raman modes and discuss distinctive features such as magnetic excitations and spin–orbital transitions in Ca_2RuO_4, electronic scattering in Sr_2RuO_4, and structural phase transitions in $Ca_{2-x}Sr_xRuO_4$.
- **Chapter 5:** presents Raman measurements under external magnetic fields. After validating the setup through Faraday rotation in Sr_2RuO_4, we analyze field-induced effects in Ca_2RuO_4, including the emergence of a new mode, its temperature dependence, and a hysteretic Raman feature linked to amplitude oscillations (Higgs mode) between magnetic ordered states.
- **Chapter 6:** reports time-resolved Raman experiments on the antiferromagnetic state of Ca_2RuO_4. We compare the system's response to res-

onant and off-resonant pumping, provide a detailed analysis of the dynamics of electronic, vibrational, and magnetic excitations, and conclude with pump-wavelength dependent measurements that reveal their distinct decay channels.

1

RAMAN SPECTROSCOPY TO STUDY COMPLEX MATERIALS

Raman spectroscopy—in our case spontaneous Raman spectroscopy—is a materials-analysis technique based on the inelastic scattering of monochromatic light by a sample. Following Adolf Smekal's 1923 prediction [12], the effect was observed almost simultaneously by C. V. Raman and K. S. Krishnan in liquids [13], and by G. Landsberg and L. Mandelstam in crystals [14]. For this discovery Raman received the Nobel Prize in 1930 [1]. The first comprehensive theoretical treatment was given by George Placzek in 1934 [15].

In Raman scattering, the energy of the scattered photon differs from that of the incident photon. Energy is conserved by exchanging a small amount with internal excitations of the sample. When the scattered photon has *lower* energy, the difference creates an excitation (Stokes process); when it has *higher* energy, the photon annihilates a pre-existing excitation (Anti-Stokes). A sketch of these processes is shown in Figure 1.1, where a lattice vibration is present.

The excitations that appear in a Raman spectrum have characteristic energies and show up as peaks in the measured intensity versus frequency shift. They include vibrational (phonons), magnetic (magnons), and, in some cases, electronic modes. The Raman spectrum thus acts as a *fingerprint* of a material and is widely used in chemistry, biology, and materials science to identify phases and molecular species. In condensed-matter physics, it is especially valuable for "complex materials", where lattice, spin, orbital, and charge degrees of freedom interact on comparable energy scales. Such interplay can produce rich phase diagrams and unusual phases—e.g., metal–insulator transitions, superconductivity, and magnetic order. A representative situation is the case under studied in this thesis-work: the ruthenate family $Ca_{2-x}Sr_xRuO_4$, where substituting Ca with Sr generates a particularly rich phase diagram.

Beyond qualitative "fingerprinting", Raman spectroscopy offers quantitative insight into dynamics and couplings (via shifts, splittings, and linewidths of Raman modes) under controlled conditions of temperature, pressure, magnetic

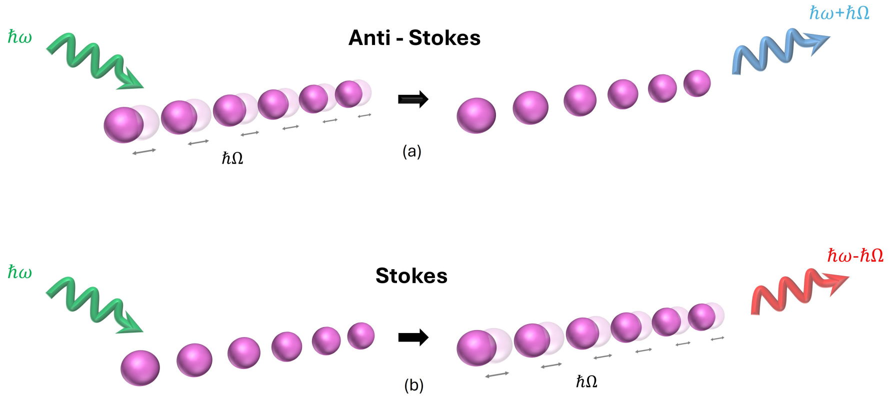

Figure 1.1: Sketch of Raman processes. (a) shows the Anti-Stokes process, where an incident photon (green) of energy ħω is absorbed by the system where a lattice vibration is present. The emitted photon (light-blue) has higher energy, which is equal to the sum of the energy of the incident photon and the lattice vibration. (b) displays the Stokes process, which consists in the opposite scenario of its "brother": after the absorption of a incident photon, it is emitted a photon with lower energy (red) and simultaneously the creation of a lattice vibration.

field, or optical cavity environment. A key advantage of *spontaneous* Raman spectroscopy is that, under suitable assumptions (stable matrix elements and near-equilibrium populations), the ratio of Anti-Stokes to Stokes intensities yields an *effective mode temperature*. This permits us to track how specific excitations are populated and how they respond to external stimuli, such as photo-induced metastable state or cavity–mediated thermal phase transitions.

In this Chapter, we begin with a concise classical description of Raman scattering and selection rules, and then introduce the quantum description. We next survey the main excitations that appear in Raman spectra, with an emphasis on magnetic excitations and the mechanisms of one- and two-magnon Raman scattering.

1.1 RAMAN SCATTERING

1.1.1 *Classical description*

Raman scattering can be understood on the basis of classical electromagnetic theory. The key idea is that the scattering is originated from a change in the polarizability of molecules by the excited quasi-particles, most tipically optical phonons. To make a clear comparison with absoprtion spectroscopy, in Raman spectroscopy it is crucial the induced modulation of the dipole by the vibrations. A molecule with a significant dipole moment gives high absoprtion but can lead to zero Raman scattering if it is not oscillating. In other worlds, it is important that intensity of the induced modulation rather than the dipole strenght itself. In the following, we use the approach described in [16, 17]. Assuming a two-atomic molecule with linear polarizability (α_0), for an applied field $E(\omega)$ the polarizability α_0 gives to a dipole moment:

$$P_D(\omega) = \alpha_0 E(\omega)$$

which acts as the source of the scattered field. If the molecule is oscillating with frequency Ω the distance between the two atoms (A and B) changes periodically (Figure 1.2).

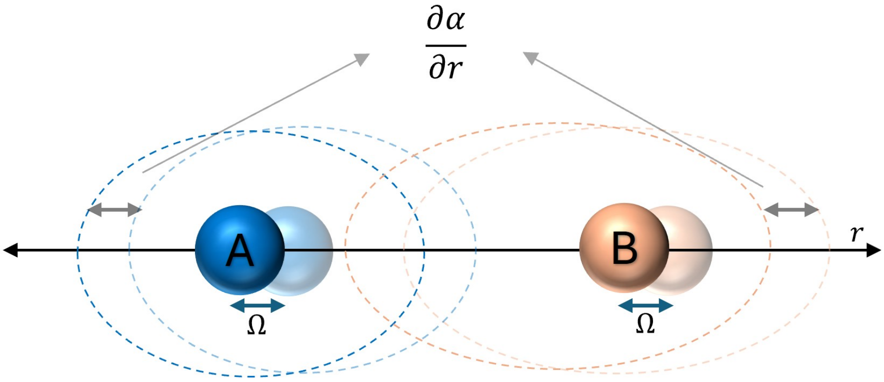

Figure 1.2: Schematic demonstration of the Raman effect for a two-atomic molecule. Ω is the frequency of the oscillation which modifies the distance r between the two atoms (A and B) and therefore modulates the polarizability α of the molecule, which is sketched as dotted lines.

Therefore, the polarizability will be modulated with an additional term $\alpha_1 = d\alpha/dr$ and the resulting total dipole moment will have the form:

$$P_D(\omega) = \big(\alpha_0 + \alpha_1 \cos \Omega t\big) E_0 \cos \omega t$$

where α_1 is always many orders of magnitude smaller than α_0, which means that the modulations are usually very weak. From trigonometric sum rules[1], we obtain:

$$P_D(\omega) = \alpha_0 E_0 \cos \omega t + \frac{\alpha_1 E_0}{2} \left[\cos\big((\omega + \Omega)t\big) + \cos\big((\omega - \Omega)t\big)\right]. \qquad (1.1)$$

---

[1]
$$P_D(\omega) = \alpha_0 E_0 \cos \omega t + \alpha_1 E_0 \big(\cos \Omega t \, \cos \omega t\big).$$

Use the product-to-sum identity

$$\cos A \, \cos B = \tfrac{1}{2}\big[\cos(A+B) + \cos(A-B)\big],$$

with $A = \Omega t$ and $B = \omega t$:

$$\cos \Omega t \, \cos \omega t = \tfrac{1}{2}\Big[\cos\big((\omega+\Omega)t\big) + \cos\big((\omega-\Omega)t\big)\Big].$$

Therefore, the scattered field originated by Equation 1.1 oscillates at three different frequencies. The first term corresponds to elastic (Rayleigh) scattering, while the second term produces inelastic sidebands because vibrations modulate the molecular polarizability. Consequently, variations in polarizability generate components at frequencies $\omega \pm \Omega$: the sideband at $\omega + \Omega$ is the *Anti-Stokes* term, while the sideband at $\omega - \Omega$ is the *Stokes* term.

Now we generalize this approach used fo a single molecule to larger systems as crystals. In this view, the role of the molecular polarizability α_0 is replaced by the susceptibility of the crystals χ, and the molecule's oscillations are replaced by the collective oscillations (phonons) of all the molecules of the crystals (Figure 1.3).

Following [16], crystal Raman scattering can be treated by expanding the susceptibility tensor χ_{ij} in the phonon normal coordinates Q_k rather than in the atomic displacements of Eq. 1.1. To first order, we have

$$\chi_{ij} = (\chi_{ij})_0 + \sum_k \left.\frac{\partial \chi_{ij}}{\partial Q_k}\right|_0 Q_k + \cdots .$$

where

$$\chi_{\ ij,\ k} = \frac{\partial \chi_{ij}}{\partial Q_k} \tag{1.2}$$

is the so called – *Raman tensor*. The scattered light intensity depends on the square of this tensor. It has three indices: i and j, which represent the three spatial directions, and k, which labels the vibrational modes. Since a unit cell with N atoms has $3N - 3$ normal vibrational modes, k runs over all the optical modes at the center of the Brillouin zone ($q = 0$). Raman spectroscopy can only probe values around the center of the Brillouin zone for two main reasons. First, due to momentum conservation in the scattering process, the maximum allowed value is approximately $2k_{in}$ (under backscattering conditions). Second, since for visible light k is on the order of 10^5, whereas typical boundary values of the Brillouin zone are on the order of 10^8, only excitations with momentum k close to zero can be observed.

Therefore, the Raman tensor is a rank-three object describing these zone-center vibrations. In particular, for a single vibrational mode (fixed k) it reduces to a 3×3 matrix, whose elements are determined from the changes in the material's susceptibility χ.

For an apply field $\mathbf{E}_l^i(t) = \mathbf{E}_{l,0}^i \cos(\omega t)$ and by expressing the phonon as $Q_k(t) = Q_{k0} \cos(\Omega_k t))$, the induced dipole moment which accounts for the emission of the Stokes/Anti-Stokes terms is

$$P_{Dj}^s(\omega \pm \Omega_k) = \epsilon_0 \chi_{jl,k} \, V_u \, E_{l0}^i \, Q_{k0} \cos\big((\omega \pm \Omega_k)t\big) \tag{1.3}$$

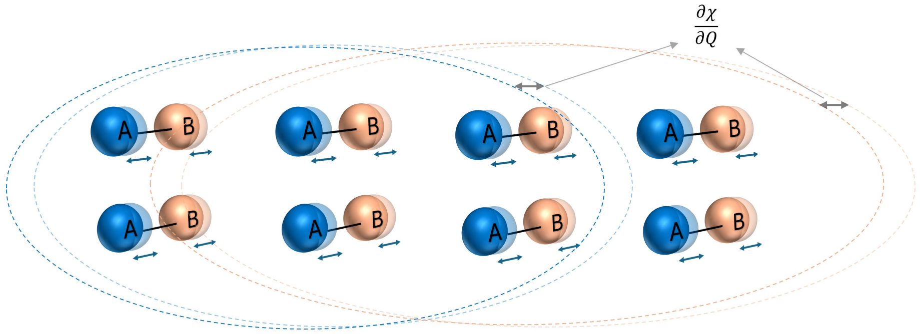

Figure 1.3: Schematic demonstration of the Raman effect for a crystal lattice of two-atomic molecules. The role of the polarizability α in single molecule (Figure 1.2) is replaced by the susceptibility χ, sketched as dotted lines. Q is the normal coordinate of the lattice, which describes the collective displacement of the atoms.

where V_u is the volume of the unit cell. For a given mode k and a selected polarization direction e^s of the scattered light, the scattering intensity is given by the square of the projection of $\mathbf{P^s_D}$ on $\mathbf{e^s}$:

$$\phi(k) = C\left|\mathbf{e^s}\cdot\mathbf{P^s_D}\right|^2 = C\left|\sum_j e^s_j\ P^s_{Dj}(k)\right|^2 \tag{1.4}$$

where P^s_{Dj} are the components of the dipole moment induced by the Raman sidebans described in Equation 1.3. It follows that the scattering intensity can be written in terms of the Raman tensor $\boldsymbol{\chi}^{(k)}$ as

$$\phi(k) = \tilde{C}\left|\sum_{j,l} e^s_j\,\chi_{j\,l,k}\,e^s_l\right|^2 = \tilde{C}\left|\mathbf{e}_s^T\chi^{(k)}\mathbf{e}_\ell\right|^2. \tag{1.5}$$

Equation 1.5 displays two important concepts: (i) the intensity of the Raman scattered light is proportional to the square of the Raman tensor $\boldsymbol{\chi}^{(k)}$ and (ii) how it is possible to measure any component of $\boldsymbol{\chi}^{(k)}$ by selecting the proper combination of the incoming and scattered polarization.

1.1.2 *Selection Rules*

This brief introduction of selection rules in crystals is taken from [17]. Crystals can be classified according to the symmetry operations required to generate the entire crystal structure (with atoms at their equilibrium positions) from a single atom or a basis. The complete set of these symmetry operations forms a mathematical group, known as the *space group*.

Group theoretical methods provide a systematic way to determine the number and symmetry of vibrational modes, as well as the selection rules governing infrared and Raman absorption. Scalar properties of a crystal, such as temperature and density, remain invariant under all group operations. In contrast, vector and tensor properties transform under these operations: vectors (e.g., dipole moments) transform like the Cartesian coordinates (x, y, z), while tensors (e.g., the susceptibility tensor) transform as products of coordinates.

The susceptibility tensor has the same symmetry representations as quadratic functions of the Cartesian coordinates, such as x^2, y^2, z^2, xy, yz, and xz. Consequently:

- A vibrational mode is *infrared-active* if its symmetry species transforms like one of the coordinates (x, y, z), since this corresponds to a change in dipole moment P_D.
- A vibrational mode is *Raman-active* if it transforms like one of the quadratic forms, corresponding to a change in the susceptibility tensor χ.

The same results can be obtained using a more qualitative approach [16]. If the geometry of the atomic displacements is known, the nature of the vibrational modes can be identified through purely geometrical considerations. These results are summarized in Figure 1.4, which illustrates the deformations Q that lead to changes in the polarizability α (or in the susceptibility χ for crystals) for symmetric diatomic, asymmetric diatomic, and symmetric triatomic molecules.

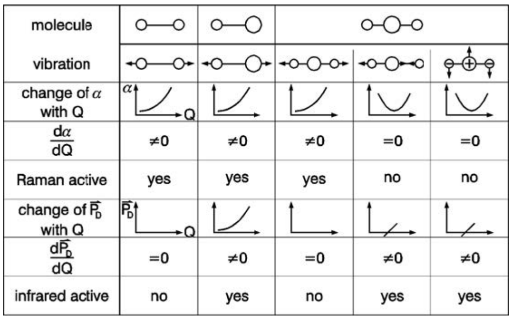

molecule					
vibration					
change of α with Q					
$\frac{d\alpha}{dQ}$	$\neq 0$	$\neq 0$	$\neq 0$	$=0$	$=0$
Raman active	yes	yes	yes	no	no
change of P_D with Q					
$\frac{dP_D}{dQ}$	$=0$	$\neq 0$	$=0$	$\neq 0$	$\neq 0$
infrared active	no	yes	no	yes	yes

Figure 1.4: Selection rules for Raman and infrared activity of vibrations. These considerations are based on geometrical arguments. Equivalent results can also be derived using group theory. Image is taken from [16].

For symmetric vibrations, the displacement of the atoms modifies the polarizability α, making these vibrations Raman-active. This is not the case for asymmetric vibrations of the triatomic molecule: to first order, the changes induced in one part of the molecule are compensated by the other, so that the derivative of the polarizability with respect to the normal coordinate Q vanishes at $Q = 0$. These oscillations are therefore Raman-inactive.

Analogous considerations apply to infrared activity. Only the vibration of the diatomic molecule and the asymmetric vibrations of triatomic molecules produce a dipole moment, and are therefore infrared-active.

1.1.3 *Quantum description*

The classical treatment of Raman scattering, while intuitive, is incomplete because it neglects the quantized nature of light and matter. A more rigorous framework is obtained within quantum mechanics, where the process is described as a two-photon inelastic scattering event mediated by a real eletronic state (resonant Raman scattering) or virtual one (Spontaneous Raman scattering). We are interested in the Spontaneous one.

A schematic view of the Raman scattering is presented in Figure 1.5 . In the Stokes process, an electron is excited by a photon ($\hbar\omega$) and it consequently relaxes into an excited state with the emission of a photon of different energy ($\hbar\omega - \hbar\Omega$). On the other hand, in the Anti-Stokes the effect is the opposite: a photon brings an excited state into an intermediate state, which decays consequently in the ground state with the emission of a photon with higher energy ($\hbar\omega + \hbar\Omega$). In a simply way, in the Stokes process the incident photon "create" an excitation inside the system, while in the Anti-Stokes the incident photon "absorbs" an excitation already present.

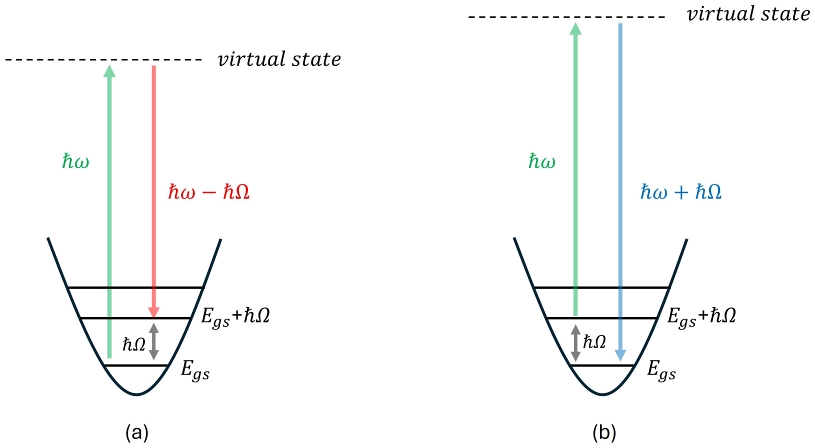

Figure 1.5: Raman scattering mechanism. (a) displays the Stokes process and (b) the Anti-Stokes. The E_{gs} is the ground state energy of the quantized lattice field. In green is shown the incident photon energy, in red and blue respectively the Stokes and Anti-Stokes–photon energy. The "quantum" of vibrational energy is $\hbar\Omega$. The initial and final state are mediated by virtual states (Spontaneous Raman scattering), which its description goes beyond the purpose of this section and it is not mentioned.

In the following, the Raman scattering proceeds by calculating quantum mechanically the dipole moment induced by the incident light; this is done through the second order perturbation theory considering a classical electromagnetic field as a perturbation. We follow the approaches in [16, 17]. In order to discuss the inelastic scattering processes (Figure 1.5) we must evaluate the matrix element for the transition between the initial state ($|i\rangle$) and final state

($\langle f|$). The polarization induced by the light is $\mathbf{P} = \chi\epsilon_0\mathbf{E}$, which drives the transitions of the scattering process. Therefore, the matrix element has the form

$$P_{fi} = \langle f|\mathbf{P}|i\rangle = \langle f|\varepsilon_0\,\chi\,\mathbf{E}|i\rangle. \tag{1.6}$$

Since $\langle f|$ and $|i\rangle$ are generalized wave functions the integration runs over all electronic and nuclear coordinates. If the wavelength of the light is much larger than the interatomic distances the electric field ($\mathbf{E}$) can be considered to be constant in Equation 1.6 so that we can extract from the equation a generalized form of the susceptibility, which is typically called as the *transition susceptibility*:

$$[\chi_{mn}]_{fi} = \langle f\,|\,\chi_{mn}\,|\,i\rangle.$$

This quantity is determined by the electronic orbitals in the crystals and therefore it is material-specific. If both initial and final states are the ground state, it turns into the classical susceptibility used for describing absorption processes. However, in Raman scattering the initial and final state are different, as it is shown previously (Figure 1.5). To calculate this element we follow the adiabatic (or Born-Oppenheimer approximation), where the total wave functions can be factorized in an electronic part $\varphi(x, X)$ and a nuclear part $\rho(X)$. Therefore, we obtain

$$\langle f\,|\,\chi_{mn}\,|\,i\rangle = \int \rho_f^*(X)\,\phi_f^*(x, X)\,\chi_{mn}\,\phi_i(x, X)\,\rho_i(X)\,dx\,dX \tag{1.7}$$

Since only the electronic part of the susceptibility is still dependent on the atomic coordinates (x), we can expand it in term of the normal coordinates (Q_k):

$$\langle f|\chi_{mn}|i\rangle = (\chi_{mn})_0\,\langle ..\,\nu_{fk}..\,|\,..\nu_{ik}..\rangle + \sum_k (\frac{\partial\chi_{mn}}{\partial Q_k})_0\,\langle ..\,\nu_{fk}..|Q_k\,|\,..\nu_{ik}..\rangle \tag{1.8}$$

where *bra* and *ket* corresponds with the total vibrational wave function of Equation 1.7. The total wave function are expressed as the product of harmonic oscillator wave function, in which ν_{ik} and ν_{fk} are their occupation numbers:

$$\langle \nu_{f1}..\nu_{fk}..\nu_{fn}| = \prod_k \langle \nu_{fk}|$$

$$\langle \nu_{i1}..\nu_{ik}..\nu_{in}| = \prod_k \langle \nu_{ik}|$$

where $\langle \nu_{fk}|$ and $\langle \nu_{ik}|$ are harmonic oscillator wave function with occupation number ν_{fk} and ν_{ik}. Since the eingenstates of the harmonic oscillator are orthogonal, the products between two wave function are:

$$\langle \nu_{fk} | \nu_{ik} \rangle = \begin{cases} 0, & \text{for } \nu_{fk} \neq \nu_{ik} \\ 1, & \text{for } \nu_{fk} = \nu_{ik} \end{cases}$$

and the expectation value of the normal coordinate is:

$$\langle \nu_{fk} | Q_k | \nu_{ik} \rangle = \begin{cases} 0, & \text{for } \nu_{fk} = \nu_{ik} \\ (\nu_{ik}+1)^{1/2}\sqrt{\frac{\hbar}{2\Omega_k}} & \text{for } \nu_{fk} = \nu_{ik}+1 \\ \nu_{ik})^{1/2}\sqrt{\frac{\hbar}{2\Omega_k}} & \text{for } \nu_{fk} = \nu_{ik}-1 \end{cases} \tag{1.9}$$

Therefore, by considering Equation 1.8, we obtain that the first term gives:

$$(\chi_{mn})_0 \, \langle .. \nu_{fk} .. | .. \nu_{ik} .. \rangle = \begin{cases} 0, & \text{for } \nu_{fk} \neq \nu_{ik} \\ (\chi_{mn})_0 & \text{for } \nu_{fk} = \nu_{ik} \textit{ (Rayleigh scattering)} \end{cases}$$

where essentially is different from zero only if the final state population is unchanged, giving the so-called *Rayleigh scattering*. On the other hand, the second term describes the Raman scattering, as evidenced by the derived susceptibility. Using Equation 1.9 in the Raman term of Equation 1.8, we have:

$$\sum_k \left(\frac{\partial \chi_{mn}}{\partial Q_k}\right)_0 \langle \nu_{fk} | Q_k \, | \nu_{ik} \rangle = \begin{cases} 0, & \text{for } \nu_{fk} = \nu_{ik} \\ (\nu_{ik}+1)^{1/2}\sqrt{\frac{\hbar}{2\Omega_k}}\left(\frac{\partial \chi_{mn}}{\partial Q_k}\right)_0 & \text{for } \nu_{fk} = \nu_{ik}+1 \\ (\nu_{ik})^{1/2}\sqrt{\frac{\hbar}{2\Omega_k}}\left(\frac{\partial \chi_{mn}}{\partial Q_k}\right)_0 & \text{for } \nu_{fk} = \nu_{ik}-1 \end{cases}$$

Therefore, summarizing these results we finally obtain for Equation 1.8:

$$\begin{aligned} \langle \nu_{ik} | \chi_{mn} | \nu_{ik} \rangle &= (\chi)_0 && \textit{(Rayleigh scattering)} \\ \langle \nu_{ik+1} | \chi_{mn} | \nu_{ik} \rangle &= (\nu_{ik}+1)^{1/2}\sqrt{\frac{\hbar}{2\Omega_k}}\left(\frac{\partial \chi_{mn}}{\partial Q_k}\right)_0 && \textit{(Stokes)} \\ \langle \nu_{ik-1} | \chi_{mn} | \nu_{ik} \rangle &= (\nu_{ik})^{1/2}\sqrt{\frac{\hbar}{2\Omega_k}}\left(\frac{\partial \chi_{mn}}{\partial Q_k}\right)_0 && \textit{(Anti-Stokes)} \end{aligned} \tag{1.10}$$

By comparing with the classical evaluation of the Raman intensity (Equation 1.3), one sees that the transition susceptibility tensor is equivalent to the derivative of the susceptibility multiplied by the amplitude of the normal coordinate (Q_{k0}). In the quantum description, this classical amplitude is replaced by its quantum-mechanical counterpart, $\hbar\nu_k/2\Omega_k$. This analogy between the classical and quantum description can be summarized in Table 1.1.

Aspect	**Classical**	**Quantum**
Normal coordinate	$Q_k(t) = Q_{k0}\cos(\Omega_k t)$	Q_k, with $\langle \nu_k \pm 1 \vert Q_k \vert \nu_k \rangle$
Amplitude	Q_{k0}	$\sqrt{\frac{\hbar}{2\Omega_k}} \times \begin{cases} \sqrt{\nu_k + 1} & \text{Stokes} \\ \sqrt{\nu_k} & \text{Anti-Stokes} \end{cases}$
Intensity	$I \propto \left(\frac{\partial \chi}{\partial Q_k} Q_{k0} \right)^2$	$I \propto \left(\frac{\partial \chi_{mn}}{\partial Q_k} \right)^2 \times \begin{cases} \hbar \frac{\nu_k + 1}{2\Omega_k} & \text{Stokes} \\ \hbar \frac{\nu_k}{2\Omega_k} & \text{Anti-Stokes} \end{cases}$

Table 1.1: Comparison between the classical and quantum descriptions of Raman scattering. In the classical case the scattering strength depends on the vibrational amplitude Q_{k0}, whereas in the quantum case this amplitude is replaced by the harmonic-oscillator matrix elements of Q_k, leading to discrete factors depending on the vibrational occupation ν_k.

1.1.4 *Lattice temperature determination*

When comparing with experimental results, it is important to account for the dependence of the Raman intensities on the vibrational occupation number ν_k, which is crucial for the scattering processes described previously by Equation 1.10. This occupation number follows a Boltzmann distribution,

$$W(\varepsilon_k) = \frac{\exp(-\varepsilon_k/k_B T)}{Z} = \frac{\exp\left[-\hbar\Omega_k\left(\nu_k + \frac{1}{2}\right)/k_B T\right]}{\sum\limits_{\nu_k} \exp\left[-\hbar\Omega_k\left(\nu_k + \frac{1}{2}\right)/k_B T\right]}, \tag{1.11}$$

so a thermal average of the form

$$\sum_{\nu_k} (\nu_k + 1)\, W(\varepsilon_k(\nu_k))$$

is required to obtain the effective square of the Raman tensor for the Stokes and Anti-Stokes processes (Equation 1.10). For Stokes scattering, the average yields $n_k + 1$, where n_k is given by the Bose–Einstein distribution for mode k:

$$n_k = f_E(\Omega_k) = \frac{1}{\exp(\hbar\Omega_k/k_B T) - 1}. \tag{1.12}$$

For Anti-Stokes scattering, the average gives simply n_k.

From [16], we present the scattered intensity per unit solid angle for the Stokes process:

$$\frac{d\Phi_s}{d\Omega} = \Phi_s' = \frac{\hbar(\omega - \Omega_k)^4\, V_u\, \chi^2_{yx,k}\, (n_k + 1)\, I_s\, V}{32\pi^2 c^4\, \Omega_k} \tag{1.13}$$

while for the Anti-Stokes we have

$$\frac{d\Phi_a}{d\Omega} = \Phi'_a = \frac{\hbar(\omega+\Omega_k)^4\, V_u\, \chi^2_{yx,k}\, (n_k)\, I_a\, V}{32\pi^2 c^4\, \Omega_k} \tag{1.14}$$

In both equations, c is the velocity of the light (in vacuum) and V the total scattering volume consisting of $N = V/V_u$. The temperature dependence of the Raman intensity follows directly from Equations 1.13-1.14 through the dependence of n_k on T. A particularly convenient experimental observable is the ratio of the Anti-Stokes (Eq. 1.14) to Stokes (Eq. 1.13) intensities of a given mode:

$$\frac{\Phi'_a}{\Phi'_s} = \left(\frac{\omega+\Omega_k}{\omega-\Omega_k}\right)^4 \exp\left(-\frac{\hbar\Omega_k}{k_B T}\right). \tag{1.15}$$

The intensities of higher-order Raman lines arise from the higher-order expansion of the susceptibility. The statistical factors that govern these processes are summarized in Table 1.2. They are expressed in terms of the phonon mean occupation number,

$$n_k = \frac{1}{\exp\left(\frac{\hbar\omega}{k_B T}\right) - 1}$$

and the scattered light intensities are proportional to the square of these factors.

Process	Stokes	Anti-Stokes
One-Phonon	$1 + n_i$	n_i
Two-Phonon (Overtones)	$2 + 3n_i + n_i^2$	$n_i + n_i^2$
Summation	$1 + n_i + n_j + n_i n_j$	$n_i + n_j + n_i n_j$
Difference	$n_j + n_i n_j$	$1 + n_i + n_j$

Table 1.2: Statistical factors for the intensities of Stokes and Anti-Stokes Raman scattering processes. Results from [17].

These relations highlight the power of Spontaneous Raman spectroscopy in dynamical studies of matter. When the matrix elements for Stokes and Anti-Stokes processes are time-independent, Raman scattering acts as a local thermometer of the excitation. This enables real-time tracking of the evolution of different subsystems—electronic, spin, and lattice—within a single measurement.

1.2 EXCITATIONS REVELEAD BY RAMAN SPECTROSCOPY

Raman spectroscopy is a powerful and versatile probe for studying a broad spectrum of excitations in condensed matter systems. It provides access to bosonic excitations, such as phonons and magnons, as well as fermionic quasiparticles "made" by electrons. Figure 1.6 illustrates typical Raman spectra together with their corresponding excitations. In the following, we will examine these excitations in more detail, with particular emphasis on magnetic excitations (*magnons*) and consequently the description of the Raman scattering from single or multiple magnons.

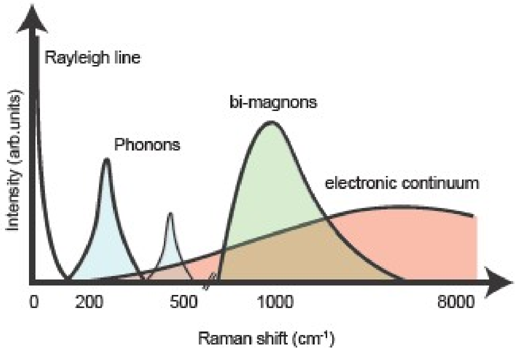

Figure 1.6: Sketch of typical excitations in Raman spectra. Image is taken from [18].

1.2.1 *Phonons*

Phonons represent the quantized vibrational modes of a crystal lattice and thus constitute its fundamental excitations. A full description of phonon excitations goes beyond the purpose of this thesis. However, it is necessary to cite them because both macroscopic and microscopic descriptions of the Raman effect are most frequently developed in terms of the lattice vibrations, as discussed in Sections 1.1.1-1.1.3-1.1.4.

In a typical Raman experiment, phonon parameters such as their energy (or frequency), intensity, and linewidth are measured while systematically varying an external control parameter. These external parameters can include temperature, applied pressure, or magnetic field. Monitoring the evolution of phonon spectra under such conditions allows us to identify signatures of structural instabilities and phase transitions. For example, the softening, quenching or splitting of specific phonon modes can act as a direct fingerprint of symmetry breaking, while changes in linewidth reveal information about phonon lifetimes and interactions with other quasiparticles.

1.2.2 *Electrons*

Electronic Raman scattering is a powerful technique for probing the electronic structure of materials. It provides direct insight into energy levels, band gaps, and electronic transitions, making it widely applied to semiconductors, insulators, metals, and a variety of correlated systems. Beyond these, it is also a valuable tool for studying charge carriers, excitons, and other electronic excitations. A comprehensive discussion of the principles and applications of electronic Raman scattering can be found in [16].

Unlike conventional Raman scattering, where the observed shifts in photon energy arise from vibrational excitations, in electronic Raman scattering the Raman shift reflects electronic transitions [19]. This technique furthermore grants access to the two-particle correlation function, which bears a close connection to the transport properties of the system [20]. An example of electronic Raman scattering can be found in the study of the high-temperature superconductors [21, 22].

1.2.3 *Magnons*

Just as phonons describe quantized excitations of lattice vibrations, magnons represent the quantized excitations of a magnetic system—the classical analogue being spin waves. A simple way to visualize spin waves is through the Heisenberg Hamiltonian,

$$H = -J \sum_{i,j} \mathbf{S}_i \cdot \mathbf{S}_j \,. \tag{1.16}$$

For $J > 0$, the energy is minimized when the spins on neighboring sites are aligned parallel, yielding a magnetic energy gain of $U = NJS^2$. As illustrated in Figure 1.7(a), this corresponds to a ferromagnetic ground state. Conversely, for $J < 0$ the system favors Antiparallel spin alignment, giving rise to Antiferromagnetic order (Figure 1.7b).

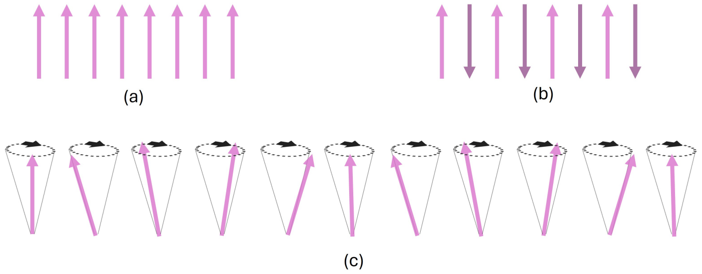

Figure 1.7: Sketch of Magnetic orderings and spin waves. Scheme of a ferromagnetic (a) and Antiferromagnetic order (b), and of a spin wave excitation for a one dimensional ferromagnetic system (c).

In real materials the situation is often more complex: magnetic anisotropies can take different forms, long-range interactions may become relevant, and in compounds with multiple atomic species various competing interactions can occur. In some cases these interactions cannot be simultaneously satisfied, leading to so-called *frustrated* magnetism. As a result, a wide variety of ground states may emerge, including *canted Antiferromagnets*, sinusoidal orders, or spiral spin textures [17].

To introduce the spin-wave formalism, let us first consider the idealized case of a one-dimensional ferromagnet, sketched in Figure 1.7(a). Following the approach in [23, 24], the excitation spectrum and dispersion relations of the Heisenberg model can be derived from the equations of motion for a spin $\mathbf{S}_i$ at site i. Assuming spins are predominantly aligned ($S^z = S$) and that transverse components satisfy $S^x, S^y \ll S^z$, the equation of motion for S^z becomes second order in the small quantities and can thus be neglected. Transforming to momentum space shows that, in the excited states, spins precess around the z-axis with the same frequency but different phases (Figure 1.7c) [25].

For an Antiferromagnet, a similar analysis applies, but both magnetic sublattices must be treated simultaneously. In this case, the linear spin-wave dispersion relation takes the form

$$\omega(k) = 2JS\,\big|\sin(ka)\big|, \tag{1.17}$$

where a is the lattice spacing.

1.2.3.1 *Raman scattering from Magnons*

The presence of magnons in magnetic materials causes a periodic modulation of the material's permittivity and light is scattered by this permittivity fluctuation. To explain the light scattering process in these systems, we follow the approach used in [26].

The polarization can be written as

$$P^j(r,t) = \varepsilon_0 \sum_i \chi^{ji}(r,t)\, E_I^i(r,t), \tag{1.18}$$

where i and j denote the three Cartesian coordinates, ε_0 is the vacuum permittivity, and χ^{ij} is the susceptibility tensor. As discussed in the previous section, this polarization serves as the source of the scattered field. The evaluation of the scattering cross section reduces to computing the correlation function

$$\langle \chi^{\alpha\beta}\, \chi^{\mu\nu} \rangle_\omega \tag{1.19}$$

with α, β, μ, ν labeling Cartesian components.[2] The average $\langle \cdots \rangle_\omega$ is not a time average but a statistical one. It represents the expectation value over the microscopic states of the medium, weighted by their thermal or quantum probabilities. In practice, this means averaging over the microscopic degrees of freedom

---

[2] The correlation function has four indices because each susceptibility tensor $\chi^{\alpha\beta}$ already carries two Cartesian labels: one (α) referring to the component of the induced polarization and the other (β) to the component of the driving field. Since the scattered intensity depends quadratically on the susceptibility, one has to correlate two such tensors, which naturally leads to an object with four indices: $\langle \chi^{\alpha\beta} \chi^{\mu\nu} \rangle_\omega$.

(e.g. vibrational, electronic, or spin states) that modulate the susceptibility. This statistical averaging connects the microscopic fluctuations of the susceptibility to the macroscopic observable scattering cross section.

The effective Hamiltonian describing the interaction of light with a magnetic system can be regarded as the electric dipole interaction between the polarization vector and the scattered field in a given direction E_S^j:

$$H = \sum_r \sum_{i,j} E_S^i \, \chi^{ij}(r) \, E_I^j, \tag{1.20}$$

where the sum over r runs over the distinct magnetic sites. In magnetic materials the susceptibility can depend on spin, and–by analogy with the treatment used for vibrational Raman spectroscopy, where we have expanded the susceptibility in normal coordinate–here we expand the susceptibility at site r in spin operators:

$$\begin{aligned} \chi^{ij}(r) = \chi_0^{ij}(r) + \sum_\mu K_{ij\mu}(r) \, S_r^\mu + \sum_{\mu,\nu} G_{ij\mu\nu}(r) \, S_r^\mu S_r^\nu \\ + \sum_\delta \sum_{\mu,\nu} H_{ij\mu\nu}(r,\delta) \, S_r^\mu S_{r+\delta}^\nu + \text{h.o.} \end{aligned} \tag{1.21}$$

The first term, $\chi_0^{ij}(r)$, represents the susceptibility in the absence of magnetic excitations and yields elastic scattering. *One-magnon processes* are captured primarily by the next two terms (K and G), which involve spin operators on a single site. These terms gives the so called–*Elliott–Loudon* process, where in particular the K term is first-order scattering while G second-order. The linear coefficient K is proportional to the magnetic circular birefringence, while the quadratic coefficient G is proportional to the magnetic linear birefringence. At the macroscopic level, one-magnon scattering proceeds via the electric-dipole coupling of light to the crystal and relies on spin–orbit interaction ($\lambda \vec{L} \cdot \vec{S}$) in the electronically excited state to change the ion's spin. Further discussion of the *Elliott–Loudon* mechanism can be found in [23, 26].

This thesis concerns mainly Antiferromagnets (Ca_2RuO_4), where the dominant scattering channel is the *two-magnon process*, described by the last term in Eq. 1.21 (the H term), which couples spins on different sites. Although this contribution can slightly renormalize one-magnon scattering, its central role is to produce pure two-magnon events in which a pair of magnons is created or annihilated. In the Stokes channel, the frequency shift of the incident light is

$$\Delta\omega = \omega(q) + \omega(q')$$

Since the photon momentum k is negligible on the Brillouin-zone scale, momentum conservation then imposes $q \simeq -q'$ (Figure 1.8a)

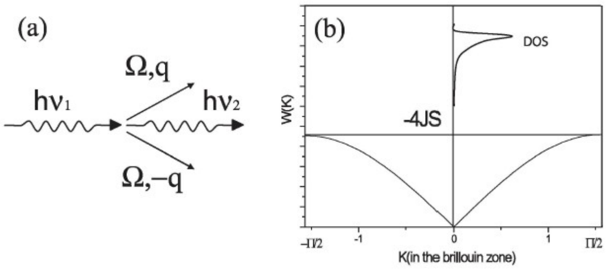

Figure 1.8: Schematic of two-magnon Raman scattering in Antiferromagnets. (a) The scattering event creates two magnons with opposite wave vectors. (b) For illustration, a sinusoidal magnon dispersion for a one-dimensional antiferromagnet is shown (Equation 1.17). The two-magnon intensity is proportional to the density of states of the magnon dispersion. Image taken from [17].

Therefore, unlike one-magnon scattering, which is confined to the zone center, two-magnon scattering spans the entire q values and so all of the Brillouin zone. Thus, the two-magnon appears in Raman spectra as a peak near the frequency range where the magnon density of states is largest, typically close to the zone boundary (Figure 1.8b).

According to the Elliott-Loudon theory, second order scattering processes should have a scattering intensity much weaker than their first-order counterpart. By contrast, experiments on Antiferromagnets, such as metal fluorides like CoF_2 and MnF_2, show that two-magnon scattering is comparable to —or frequently stronger than—the one-magnon signal [27, 28]. This apparent discrepancy was resolved by proposing a more efficient process, the exchange-scattering mechanism [24], even know as the *Fleury-Loudon* effect.

To explain this process, consider the two-magnon excitation spectrum of a simple Antiferromagnet, which comprises two magnon branches corresponding to spins precessing in opposite directions on the two sublattices, $\omega_\pm(k)$. Physically, these branches represent excitations where the total S^z changes by ± 1. In zero magnetic field the two branches are degenerate [26]. We denote their states by $|k,+\rangle$ and $|k,-\rangle$, where $+(-)$ indicates an increase (decrease) in S^z. Linearly independent two-magnon states with momenta k and $-k$ can then be constructed as

$$\begin{aligned} |a\rangle &= |k,+\rangle|-k,+\rangle & \Delta S^z &= +2 \\ |b\rangle &= \frac{1}{\sqrt{2}}(|k,+\rangle|-k,-\rangle + |k,-\rangle|-k,+\rangle) & \Delta S^z &= 0 \\ |c\rangle &= \frac{1}{\sqrt{2}}(|k,+\rangle|-k,-\rangle - |k,-\rangle|-k,+\rangle) & \Delta S^z &= 0 \\ |d\rangle &= |k,-\rangle|-k,-\rangle & \Delta S^z &= -2 \end{aligned} \tag{1.22}$$

The states $|a\rangle$ and $|d\rangle$ correspond to one-magnon processes extended to higher order. In contrast, $|b\rangle$ and $|c\rangle$ ($\Delta S^z = 0$) describe spin deviations on opposite sublattices, mediated by exchange interactions through a virtual electronic transition. The even-parity state $|b\rangle$ underlies two-magnon Raman scattering, whereas the odd-parity state $|c\rangle$ is more relevant for two-magnon absorption. This mechanism provides a far more efficient scattering channel than the higher-order one-magnon route, demonstrating that two-magnon scattering originates from a distinct physical process. Consequently, there is no a priori reason for the two-magnon intensity in Antiferromagnets to be weaker than the one-magnon feature.

2

EXPERIMENTAL APPARATUS

The experiments in this thesis required two complementary Raman platforms: (i) a high–spectral-resolution, polarization-resolved setup for equilibrium measurements over broad spectral windows and (ii) a tunable time-resolved spontaneous Raman (TRSR) setup to measure non-equilibrium dynamics with controlled time–energy resolution. Both platforms share a common set of constraints: efficient Rayleigh rejection close to the laser line, well-defined in/out polarizations to select symmetry channels, and reliable operation from room temperature down to cryogenic conditions.
This chapter is divided in two parts. In the first part we present the Static spontaneous Raman setup and in the second one the Tunable Time-resolved Spontaneous Raman setup that we design and built.

2.1 STATIC SPONTANEOUS RAMAN SETUP

The Raman apparatus is based on a **TriVista CRS**^{3} (*S&I Spectroscopy & Imaging GmbH*) triple spectrometer coupled to a confocal microscope. Excitation is provided by a continuous-wave (CW) laser. Two sources are available, 532 nm and 633 nm, although all the measurements presented here were performed with the 532 nm line. The beam power is 80 mW and can be controlled by using neutral density filters (ND filters). The laser is focused onto the sample by a high-numerical-aperture (NA) confocal microscope objective, with a spot size on the sample of approximately 5 µm. It is crucial to have a high NA to collect the maximum available scattered light, while the confocal microscope is essential to maximize the scattered light at the focal spot, resulting in excellent imaging of the focus that is approximately independent from the position of the laser on the sample. The scattered light is collected in a backscattering configuration.
In the following, we present schematically the main parts and possible configurations of our setup.

- The **polarization control** is achieved with one $\lambda/2$ and one analyzer: one placed in the excitation path, before the beam reaches the sample, and one in the detection path, before the spectrometer. In this way we perform parallel ($E_{in} \| E_{out}$) and crossed ($E_{in} \perp E_{out}$) configurations. In order to minimize the effect on the gratins arising from changes in the polarization, a $\lambda/4$ plate, rotated by 45° with respect to the analyzer, is placed after the analyzer. The polarizations of the incident and scattered light lie in the xy-plane.

- The **acquisition system** consists of a **triple-stage spectrometer** coupled with a charged coupled device (CCD) detector (*PIXIS, Princeton Instruments*), which is cooled down to $-75\,C°$ by using a four-stage Peltier cooler in combination with circulating air or coolant.
  The diffraction grating of the spectrometer disperses the scattered light, and the CCD records the spectra with integration times depending on the measurement. Three diffraction gratings are available with different spectral resolutions. The latter is set by the grooves density designed on the surface of the dispersion grating. The available gratings in the set-up have 300 g/mm, 1200 g/mm and 2400 g/mm with corresponding increasing resolution and decreasing spectral bandwidth.

  The system can be easily switched between **single-stage** and **triple-stage** configurations.
  In single-stage is used only the last stage. The spectral resolution depends on the gratings used. For all of the following measurements (expect when clearly explicited) we use 1200 g/mm and set at minimum the slit entrance (150 μm).
  In triple-stage mode, the spectrometer can be operated in either **additive** or **subtractive** configuration (see Figure 2.1).

  - In **additive mode**, each stage further disperses the incoming light, yielding a resolution equivalent to a single spectrometer with a focal length equal to the sum of the three stages. The highest spectral resolution is $0.1\ \text{cm}^{-1}$ by using inseries the three 2400 g/mm gratings.
  - In **subtractive mode**, the first two stages act as a tunable bandpass filter, transmitting only the desired spectral range and strongly suppressing stray light. Therefore, this configuration allows the fundamental laser line (elastic/Rayleigh scattering) to be partially rejected without notch filters. Additionally, a key advantage of this configuration is the ability to resolve modes close to the laser line, down to $\sim 5\,\text{cm}^{-1}$.

- **Spectral filtering:** Rayleigh scattering is suppressed either by edge or notch filters, depending on the measurement: **edge filters** are used for

Stokes-only analysis, while **notch filters** are required when both Stokes and anti-Stokes signals are recorded.
Additionally, two approaches can be used to suppress the laser line for simultaneous Stokes–anti-Stokes measurements: (i) operating the triple-stage spectrometer in subtractive mode, which further suppresses Rayleigh scattering, and (ii) installing laser masks between the first and second stages. The laser mask is a thin metal bar centered in the slit that mechanically blocks the laser light. It offers four settings—three bar widths (150, 300, 600 µm) and an open position that allows the Raman signal to pass through the intermediate slit unblocked.

The system can be used in two different configurations:

1. **Room-temperature, in-air measurements.** The sample is mounted directly under a confocal microscope (*IXplore Standard, Olympus*) equipped with a translational stage. The available microscope objectives have amplifications of 10 x, 50 x and 100 x, with, respectively, numerical aperture (NA) of 0.30, 0.55, 0.90. A (optional) rotational stage allows the sample to be rotated in the xy-plane, so that the polarization of the light can be aligned relative to the crystallographic axes. The corresponding set-up is presented in Figure 2.2.

2. **Low-temperature and magneto-Raman measurements.** For temperature-dependent experiments, the system is coupled to an **OptiCool cryostat** (*Quantum Design*), operating in the range $1.7 - 350$ (± 0.1) K and equipped with a **superconducting magnet** providing fields up to ±7 T along the z-axis. The laser is focused on the sample using a high-NA microscope objective positioned inside the vacuum chamber but kept at room temperature, which preserves its full optical performance. The NA is 0.7, magnification 50 x and working distance of 7 mm. The spot size of the laser beam is approximately $\sim 5\,\mu\text{m}^{-1}$. The corresponding set-up is presented in Figure 2.3.

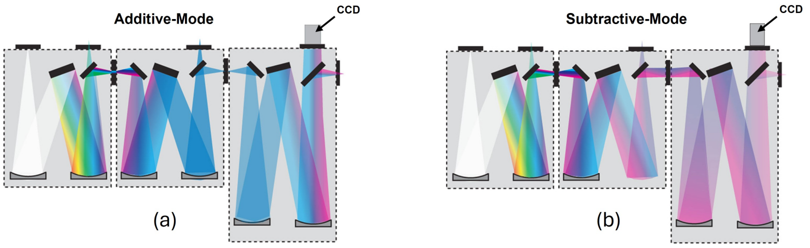

Figure 2.1: Schematic representation of the TriVista CRS^3 spectrometer in additive and subtractive configurations. In additive mode (a), all three stages contribute to spectral dispersion. In subtractive mode (b), the first two stages act as a tunable bandpass filter, transmitting a narrow spectral window to the final dispersive stage. Therefore, this configuration allows the fundamental laser line (elastic/Rayleigh scattering) to be partially rejected without notch filters. In the single-stage configuration, only the last stage is used by a second entrance port. The spectral resolution of this configuration is depending on the selected gratings (approximately 1 cm^{-1}), while is 0.1 cm^{-1} in additive mode [29] (with 2400 g/mm). Images adapted from [29].

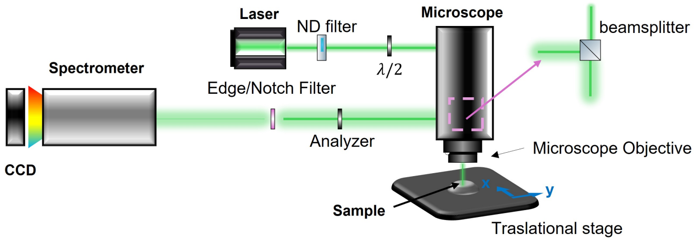

Figure 2.2: Scheme of Room-temperature in-air Raman set-up: TriVista CRS^3 spectrometer coupled to a confocal microscope (*IXplore Standard, Olympus*) with translational and (optional) rotational sample stages. The laser (CW at 532 nm) is focused onto the sample through a high-NA objective with a spot size of $\sim 5\,\mu m^{-1}$, and scattered light is collected in backscattering geometry. The polarization is in plane and is controlled by a $\lambda/2$ and by an analyzer in order to perform parallel and crossed configuration. The Rayleigh scattering is suppressed either by edge or notch filters, depending on the type of measurements.

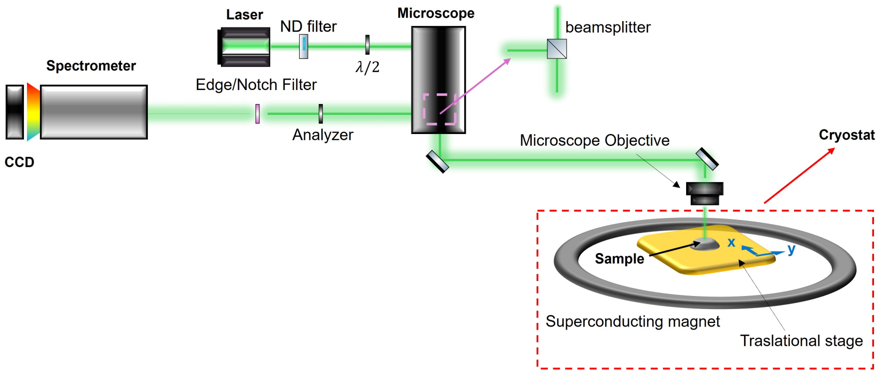

Figure 2.3: Scheme of Cryostat-coupled Raman set-up: the sample is mounted in an OptiCool cryostat (*Quantum design*), allowing measurements in the temperature range $1.7-350$ K and under magnetic fields up to ± 7 T along the z-axis. The acquisition scheme remain identical to the room-temperature configuration (Figure 2.2).

2.1.1 *Static Raman measurement on Silicon*

Silicon was chosen as a reference material to benchmark the performance of the Raman apparatus. Its well-known and sharp first-order Raman mode at $\sim 520\ \mathrm{cm}^{-1}$ provides an ideal test.

First, we perform a Stokes/anti-Stokes measurement using the triple-stage spectrometer in subtractive mode (300 g/mm) to partially suppress the laser line. To further reduce the elastic scattering, it is used a laser mask between the first and second stage. This configuration allows the simultaneous collection of both Stokes and anti-Stokes signals. The excitation wavelength was $\lambda_0 = 532$ nm with a fluence[1] of $3.20\,\mathrm{nJ/cm^{-2}}$. Measurements were carried out in crossed polarization at room temperature inside the OptiCool cryostat (see scheme in Figure 2.3).

The corresponding raw spectrum is shown in Figure 2.4. The y-axis represents the CCD intensity (proportional to the number of scattered photons)[2], while the x-axis corresponds to the Raman shift ($\Delta\tilde{\nu}$), defined as the difference in wavenumber between the incident and scattered photons:

$$\Delta\tilde{\nu} \equiv \tilde{\nu}_0 - \tilde{\nu}_s = \frac{1}{\lambda_0} - \frac{1}{\lambda_s}. \tag{2.1}$$

Although the raw spectrum still exhibits a residual laser line, both the Stokes and anti-Stokes modes are clearly visible with a width of $4-5\ \mathrm{cm}^{-1}$. The data are then pre-processed following the protocol described in [30], consisting of

---

[1] Fluence is measured using a average power of 8 mW and spot size of $\sim 50\mu$m over 1 ps of time-window to make a comparison between these measurements and the ones obtained with ps pulses.

[2] The CCD produces a 2D pixel array. For all measurements we report the average over a selected region of interest.

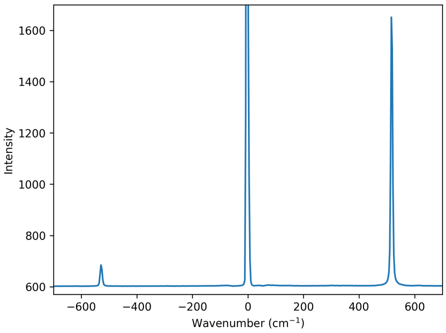

Figure 2.4: Raman spectrum of Si. it is collected in subtractive triple-stage configuration (300 g/mm) inside the Opticool ($E_{in} \perp E_{out}$). Both Stokes and anti-Stokes modes at ~ 520 cm^{-1} are visible, together with a residual contribution from the laser line. The meaurements are performed at room temperature.

cosmic ray removal, Gaussian filtering, baseline correction with Asymmetric Least Squares, and normalization by the area under the curve. The processed spectra are shown in Figure 2.5(a) and (b). A comparison of background regions before and after preprocessing is reported in appendix B (Figure A.1). All Raman spectra presented in the following sections have been preprocessed using this method, unless when is explicitly mentioned.

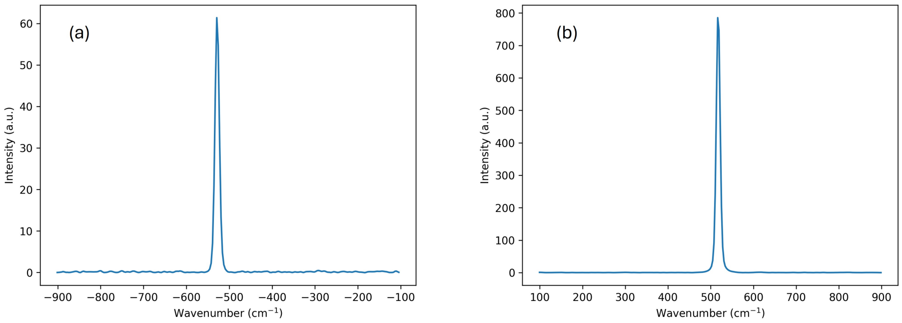

Figure 2.5: Preprocessed Raman spectra of Si: (a) anti-Stokes side and (b) Stokes side, after cosmic ray removal, Gaussian filtering, baseline correction, and area normalization [30] (A detailed zoom-in of the background is displayed in Figure A.1). The phonon modes are clearly resolved and suitable for extracting the Raman temperature.

Finally, to demonstrate the validity of the setup, we extract the signal strengths of the phonon at the Stokes and anti-Stokes positions by fitting the mode with Gaussian function. We determine the temperature based on a Boltzmann distribution. According to [31], the expressions most frequently given to describe this relationship are shown in Equations 2.2-2.3 [32]:

$$\frac{I_{AS}}{I_S} = \left(\frac{\nu_L + \nu_{ph}}{\nu_L - \nu_{ph}}\right)^4 \exp\left(-\frac{h\nu_{ph}}{k_B T}\right) \quad \Longrightarrow \quad T = \frac{h\nu_{ph}}{k_B} \bigg/ \ln\left[\frac{I_S}{I_{AS}}\left(\frac{\nu_L + \nu_{ph}}{\nu_L - \nu_{ph}}\right)^4\right] \tag{2.2}$$

$$\frac{I_{AS}}{I_S} = \left(\frac{\nu_L + \nu_{ph}}{\nu_L - \nu_{ph}}\right)^3 \exp\left(-\frac{h\nu_{ph}}{k_B T}\right) \quad \Longrightarrow \quad T = \frac{h\nu_{ph}}{k_B} \bigg/ \ln\left[\frac{I_S}{I_{AS}}\left(\frac{\nu_L + \nu_{ph}}{\nu_L - \nu_{ph}}\right)^3\right], \tag{2.3}$$

where T is the temperature associated with the phonon mode, k_B is Boltzmann's constant, h is Planck's constant, ν_L is the frequency of the laser, ν_{ph} is the frequency of the vibrational mode (Raman band position), and the Stokes (I_S) and anti-Stokes (I_{AS}) Raman scattering strengths are based on energy detection of the signals. The type of intensity-experimentally measurement is very important. The use of Equation 2.2 is appropriate when spectra are acquired with energy-based detection, whereas Equation 2.3 should be used when photon counting is the basis for detection [33, 34]. The spectra reported here were all acquired using a charge-coupled device (CCD) detector, a photon counting device, so equation 2 is more appropriate for the analysis of our data. We implement both equations and we summarize the results in Table 2.1, where it is compared the obtained lattice temperatures T with the temperature measured at the sample holder by the OptiCool cryostat at room temperature. Since the system is at thermal equilibrium (all of the degree of freedom have the same T), the lattice temperature T coincide with the macroscopic temperature of the sample.

Although the results are not completely equal with the temperature of the sample holder, we can argue that the use of Equation 2.3 is more accurate. The discrepancy of the temperatures might originate from the fact that the Opticool temperature is measured at the sample holder, therefore not directly referred to the sample. Moreover, this analysis might, in principle, exclude a local heating from the laser in Si, since the effective temperature is less than the room temperature expected.

Table 2.1: Temperatures of Si in Opticool. Comparison between the cryostat sample holder temperature (T_{holder}) and the Raman-derived sample temperatures from the Si mode determined using Equation 2.2 (T^4_{Si}) and Equation 2.3 (T^3_{Si}). Moreover, we add the temperature obtained without the prefactor $\left(\frac{\nu_L+\nu_{ph}}{\nu_L-\nu_{ph}}\right)$ (T^0_{Si}).

T_{holder} **(K)**	T^3_{Si} **(K)**	T^4_{Si} **(K)**	T^0_{Si} **(K)**
300 ± 0.1	274.2 ± 0.4	268.7 ± 0.4	291.6 ± 0.4

2.2 TUNABLE TIME-RESOLVED SPONTANEOUS RAMAN SETUP

2.2.1 Ab initio *considerations*

Typical design parameters for a time-resolved spontaneous Raman (TRSR) setup include energy resolution, time-resolution, the laser linewidth, and laser repetition rate [35]. Other design factors include tunability of the pump excitation and Raman probe light. The energy- and time- resolution paramaters are of crucial importance in TRSR experiments. For a trasform-limited Gaussian pulse, the bandwidth-time relation is

$$\Delta\nu\Delta\tau \sim 14.7\text{cm}^{-1}\text{ps},$$

where $\Delta\nu$ is the frequency (energy) bandwidth of a pulse and $\Delta\tau$ is the pulse duration[3]. Therefore, the technique inherently links time and energy resolution, and an ideal setup should provide control over both. The boundary between accessible and forbidden regions is set by the Fourier transform relation as described in Figure 2.6. Since our goal is to investigate the dynamics of collective excitations in quantum materials—such as magnons, phonons, Cooper-pair breaking, and charge-density-wave modes—which are low-energy excitations with $\Delta E < 120\,\text{meV}$, the relevant energy scale corresponds to Raman shifts of $\sim 1000\ \text{cm}^{-1}$ and below, and therefore requires high spectral resolving power.

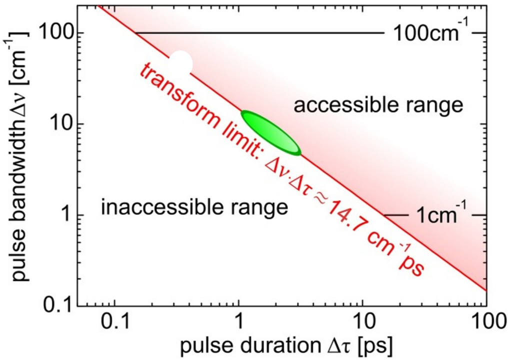

Figure 2.6: Energy and temporal ranges of the TR experiment. For Gaussian pulses, the Fourier-transform relation $\Delta\nu\,\Delta\tau \sim 14.7\ \text{cm}^{-1}\cdot\text{ps}$ links the spectral bandwidth $\Delta\nu$ to the pulse duration $\Delta\tau$, and thus sets the boundary between accessible and forbidden regions. For TRSR studies of quantum materials, the energy-resolution range of interest is $\sim 1\text{–}100\ \text{cm}^{-1}$, which corresponds to temporal resolutions from roughly 15 ps down to 150 fs. The green ellipse indicates the operating regime with a picosecond probe. Image adapted from [36].

In spontaneous Raman spectroscopy, the inelastically scattered light needs to be separated from the Raman excitation light. Tipically, it is used notch fil-

---

[3] Here, $\Delta\nu$ and $\Delta\tau$ refer to the FWHM.

ters. However, when tunability in probe wavelenght is of importance, a triple subtractive Raman spectrometer is still favored (see scheme in Figure 2.1). In TRSR spectroscopy, one more feature appears since the pump-beam and the pump-induced Raman spectrum need to be filtered out. In [35], different filtering schemes have been applied for this:

- Degenerate[4] TRSR experiment: polarization optics are used to reject the pump-induced elastic and inelastic scattered light, but only the parallel geometry can be studied [37];
- Two-color TRSR experiment: the pump-induced effects can be conveniently rejected by spectral filtering [35, 38]. We implement this type of scheme in our setup, as described in what follows.

Amplified laser systems allow for tunable two-color experiments and overcome the average heating problem by using high repetition rate amplifiers, which gives enough average power with lower per-pulse energy, reducing peak-intensity problems and heating [36].

2.2.2 *Setup overview*

We develop a TRSR setup with a ps-probe and two different pump-pulses. The crucial uniqueness of the setup lies in the fact that all of the pulses can be finely tuned in a wide range of wavelenght, allowing us the possibility to finely pump between $650-900\,\text{nm}$ or $1.3-16\,\mu\text{m}$, and simultaneously probing across $315-1010\,\text{nm}$. Moreover, the system can be switched between TRSR and static spontaneous Raman operation (Figure B.1)—or configured for single color pump-probe measurements, where the time-resolved integrated reflectivity is measured (Figure 2.9).

The system consists of three main parts: (A) the amplified laser system and optical parametric amplifiers to generate pulses for selective pumping, and narrow-bandwidth pulses for Raman probing, (B) the table optics for pulse cleaning, polarization control, and the delay line, and (C) the confocal Raman microscopy interface, the high efficiency spectrometer, and the charge-coupled device detector. We present the layout of the setup in Figure 2.7.

---

[4] Degenerate refers to pulses with the same color.

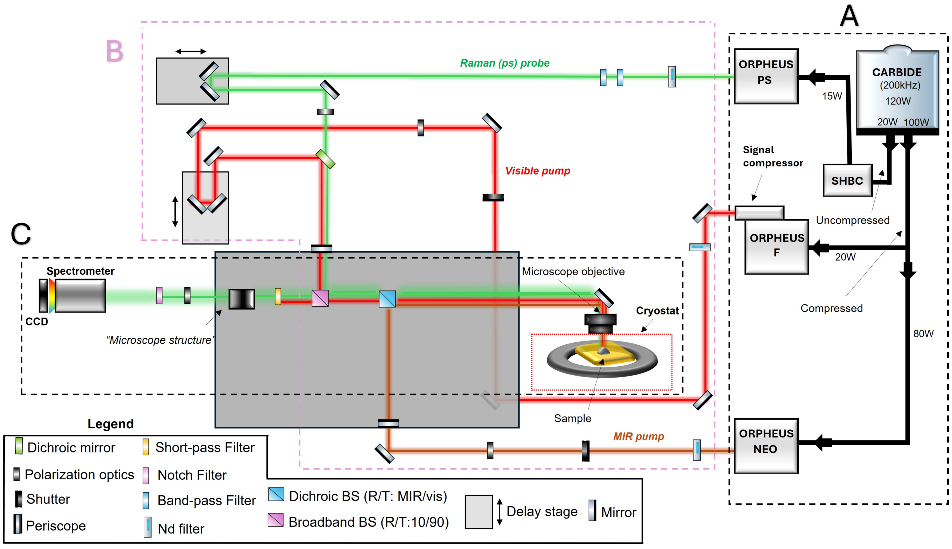

Figure 2.7: Scheme of the TRSR setup. The system consists of three main parts: (A) the amplified laser system and optical parametric amplifiers to generate pulses for selective pumping, and narrow-bandwidth pulses for Raman probing, (B) the table optics for pulse cleaning, polarization control, and the delay line, and (C) the coupling of the three beams, Raman interface, and acquisition scheme. See the main text for details.

2.2.2.1 *A: Amplified Laser System and tunable pump excitations and Raman probe*

A chirped pulse amplification based laser system (*Light Conversion CARBIDE*) is used for the setup. The CARBIDE is a high repetition rate femtosecond laser system based on a chirped pulse amplification technique, which uses directly diode-pumped Yb:KGW (ytterbium-doped potassium gadolinium tungstate) as active medium. The CARBIDE laser head comprises of a Kerr lens mode-locked Oscillator, Regenerative Amplifier and Stretcher-Compressor units. The emitted pulses have $\lambda_c = 1024$ nm central wavelength. The repetition rate can be set up to $f_{max} = 200$ kHz with a power of 120 W. After the regenerative amplification stage, the 1024 nm stretched pulse beam is divided into two beams:

- One beam is compressed with an average power of 100 W. This beam is split and 80 W are routed to a Orpheus-NEO (400 µJ/pulse) and 20 W to a Orpheus-F (100 µJ/pulse):
  - Orpheus-NEO is a three-stage white-light–seeded femtosecond optical parametric amplifier (OPA) to generate tunable pulses of $\sim$ 80 fs (*Light Conversion ORPHEUS-NEO*). The Signal is continuously tunable from 1300–2000 nm, the Idler from 2100–400 nm and optional difference frequency generation (DFG) extends coverage to 4000–16000 nm, therefore the overall tunability is 1.3 µm—16 µm.

  - Orpheus-F is a two-stage white-light–seeded femtosecond OPA (*Light Conversion ORPHEUS-F*). The Signal can be continuously tuned from 650–900 nm and is externally compressed by a two-prism compressor. Idler runs from 1200–2500 nm. The output pulses are 30 fs.

- Other beam is emitted as an 20 W (100 μJ/pulse) output of non-compressed (NCB) —ps long pulses. This beam is routed to a second harmonic bandwidth compressor (*Light Conversion SHBC*):
  - The SHBC converts the 1024 nm pulses of FWHM $\Delta\nu \sim 50\,\mathrm{cm}^{-1}$ into 512 nm trasform limited pulses $\Delta\nu \sim 10\,\mathrm{cm}^{-1}$ with FWHM and $\Delta\tau \sim 1$ ps temporal width. The SHBC output is used to pump a three stage white-light seeded picosecond optical parametric amplifier (*Light Conversion PS-OPA*). The PS-OPA can continuosly tune the Raman probe wavelength from 630 − 950 nm, while signal and idler of the PS-OPA output can be externally coupled to a second and fourth-harmonic generator to tune the probe wavelength between 320 − 600 nm.

The TRSR setup operates in the green oval region in the ($\Delta\nu$,$\Delta\tau$) in Figure 2.6 when the probe used is PS-OPA output. In this thesis, we consistently use a PS-OPA probe centered at 532 nm to enable direct comparison between measurements obtained with the static setup (Chapters 4 and 5) and the time-resolved setup (Chapter 6). Pump pulses are provided by Orpheus-F (630–950 nm) and, for lower-photon-energy excitation, by Orpheus-NEO (1.3–16 μm). Hereafter, we refer to Orpheus-F as the visible pump and Orpheus-NEO as the MIR pump.

Finally, we report in Table 2.2 the standard optical parameters which summarize the performance of the setup.

Table 2.2: Typical performance of the setup. We report the tunability and time-duration of the beams of the setup.

Pulse	**Tunability**	**Time duration**
Visible pump (Orpheus-F)	650 − 900 nm	30 fs
MIR pump (Orpheus-NEO)	1.05 − 16 μm	80 fs
Raman probe (Orpheus-PS)	640 − 1010 nm; 315 − 630 nm	1 ps

2.2.2.2 *B: Table Optics*

A general spectral characteristic of an optical parametric amplifier (OPA) is that, together with the amplified pulses described earlier, a spurious non-amplified background is emitted. In particular, the 513 nm non-filtered output of the SHBC band is always present. The intensity of this non-amplified

background is weak compared to the OPA output and therefore usually negligible for most spectroscopic applications (the background is approximately 10^{-6} weaker than the amplified output). However, this is not negligible in the case of Raman spectroscopy. Considering that the typical cross section of a Raman process is 10^{-8}–10^{-10} relative to the excitation line, the background is expected to be much more intense than the Raman signal, requiring appropriate spectral filtering. To verify the origin of these signals, it is common practice to shift the laser line and check whether the Raman shift remains constant (as expected for a Raman process) or changes.
Since our Raman probe is centered at 532 nm, we employ narrow bandpass filters at this wavelength to suppress spurious signals. In particular, we use filters with bandwidths of 1 nm and 4 nm.

Polarizers are placed to control the polarization of both probe and pump pulses. A second polarizer (analyzer), which is fixed to maximize the efficiency of the spectrometer (Figure 2.2-2.3), allows the use of parallel ($E_{in} \parallel E_{out}$) and crossed ($E_{in} \perp E_{out}$) polarization geometries. As in the static version (Figure 2.1-2.3), the Raman experiments are performed in a back-scattering configuration with the polarizations of the beams in plane (xy).

The setup is equipped with two translation stages to independently control the time delay between the three beams. A first translation stage (TS1) is placed in the probe path, so that TS1 tunes the delay between the probe and the MIR pump[5], while the second translation stage (TS2) modifies the optical path of the visible pump. This approach enables pump–probe experiments with both the visible pump and MIR pump.

The visible pump and probe beams are made collinear before entering the Raman interface (Part C) by means of a dichroic mirror.

2.2.2.3 *C: Coupling of the three beams, Raman Interface, and Acquisition Scheme*

The collinearly propagating visible pump and probe beams enter the Raman microscopy interface via a periscope, while the MIR pump enters the same microscopy setup via a second periscope. The **coupling of the beams** into the microscope and their corresponding filtering are described as follows:

- The collinear visible pump and probe beams are reflected from a broadband beam splitter (R/T: 10/90) (BS1). This type of beam splitter is used for two reasons. Firstly, since the two beams are tunable over a wide

---

[5] In pump–probe experiments, only the relative delay between pump and probe matters, not their absolute timing. The delay can therefore be set by changing the optical path of either beam. In our setup, because the MIR pump operates at 1.05–2.6 µm and 2.5–16 µm, where air absorption is significant, we keep its path as short as possible and adjust the probe path instead.

wavelength range, (i) the broadband nature ensures that the system does not depend significantly on the colors used. Secondly, (ii) the low reflectivity R is chosen because in a Raman experiment it is important to collect as much scattered light as possible, which in our system is acquired via the transmission of BS1.
To filter the residual visible pump beam, a shortpass filter at 650 nm is used.

- The MIR pump enters via a second periscope and is made collinear to the other beams by a dichroic beam splitter (BS2), which reflects the mid-IR and transmits the visible. In this way, the scattered MIR pump is removed by BS2 when the beam travels backwards after the interaction with the sample.

We defocus the microscope objective to achieve higher incident probe power without damaging the samples, as in [36]. This further increases the Raman scattering, since it scales with incident laser intensity. The spot sizes of the ps probe and pump pulses are ~ 50 μm, measured with a camera.
When using the MIR pump, we employ a reflective microscope objective ($NA = 0.5$), since the previous objective (see Sect. 2.1) absorbs strongly in the MIR range.

The **acquisition scheme** is as follows. For each fixed time delay (t_i), two Raman spectra are acquired: one with the pump on and one with the pump off. During the pump-off acquisition, a mechanical shutter blocks the pump beam for the entire integration time, while the CCD camera records the Raman spectrum. The CCD operates in read-out trigger mode, waiting for the shutter trigger.[6] In order to avoid experimental artifacts due to the time opening of the pump shutter and of the CCD shutter, we use a CCD integrations time (t_{int}) which is 500 ms shorter than the actual opening/closing period of the pump shutter ($t_{shutter}$). At each delay position (t_i), we perform n scans (one scan $\equiv$ one pump-on + one pump-off spectrum). After n scans, acquisition is paused and the time delay is changed. At the new delay, the same procedure is repeated until the final delay (t_f) is reached. The entire measurement sequence can then be repeated m times. A schematic is shown in Figure 2.8.

---

[6] A function delay generator (FDG) shifts the shutter trigger so that the CCD camera always receives a positive sharp signal. Since the CCD in trigger mode can read only positive (or only negative) signals, and the shutter provides either negative or positive outputs depending on its transition (on→off or off→on), we manually adjust the shutter output to always provide a positive signal to the CCD. To do this, the temporal delay of the FDG must be fitted to the desired CCD integration time.

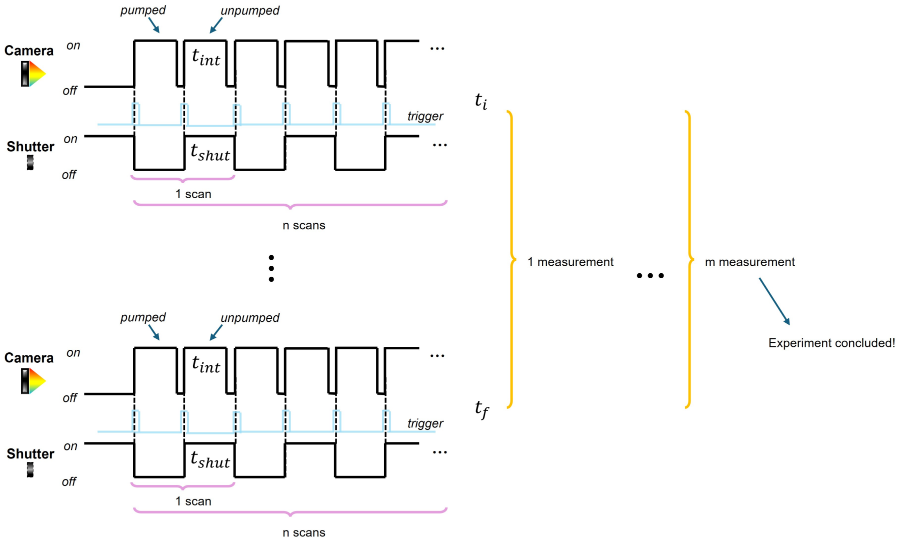

Figure 2.8: Differential acquisition scheme of the TRSR setup: t_{int} is the CCD integration time for the Raman spectrum, t_{shut} is the time during which the shutter mechanically blocks (or not) the pump pulse, and t_i and t_f are the initial and final time delays of the time-resolved measurements.

2.2.2.4 *Integrated single color pump-probe set-up*

The TRSR setup (Figure 2.7) can be easily switched to a standard pump–probe (PP) configuration in which the differential reflectivity of the Raman probe is collected by photodetectors and amplified by a lock-in amplifier (Figure 2.9). Although this configuration can be used to perform a wide variety of PP experiments thanks to the large tunability of the beams, the temporal duration of the probe used (1 ps) affects significantly the temporal resolution of the PP measurements. Therefore, here we mainly use it just to (i) preliminarily find and optimize spatial and temporal overlap before TRSR experiments and (ii) study the integrated intensity of the Raman probe. The measured signal is the differential reflectivity $\Delta R/R$, where ΔR is the difference of reflectivity when the system is pumped (R_{on}) and unpumped (R_{off}).

The main difference relative to the TRSR setup is the acquisition system, which consists of two photodetectors coupled to a lock-in amplifier. One photodetector is used as a reference (to monitor the incident probe for normalization), while the other collects the probe reflected from the sample. A mechanical chopper modulates the pump beam, and the lock-in amplifier is referenced to the chopper frequency, improving the signal-to-noise ratio by rejecting out-of-band noise.

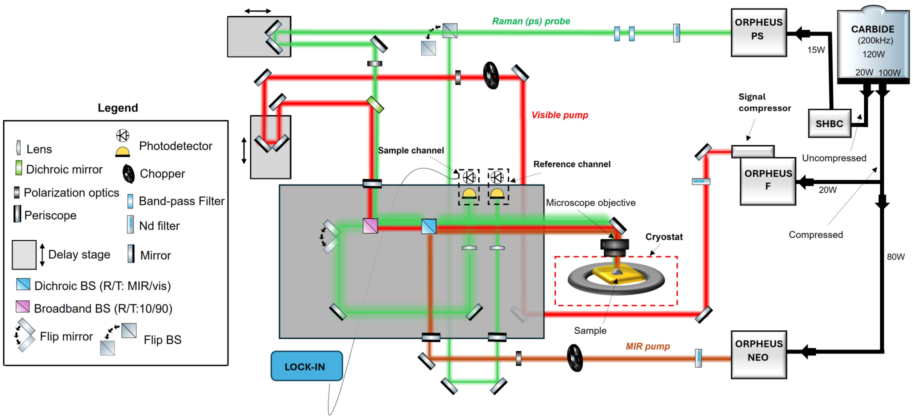

Figure 2.9: Scheme of the integrated single-color PP setup. The setup differs from the TRSR configuration (Figure 2.7) mainly in the acquisition system: two photodetectors (reference and signal) and a lock-in amplifier measure the differential reflectivity ΔR, with the pump beam modulated by a mechanical chopper. Integration with the TRSR beam path is achieved using a flip mirror and a flip beam splitter.

2.2.3 *Test-of the time-resolved Raman set-up: phonon dynamics in silicon*

In order to test the validity of the setup discussed previously, we perform TRSR measurements on Si. We excite the Si sigle crystal (100) oriented at room temperature above the indirect band-gap with 700 nm pulses. The Raman probe excitation is centered at 532 nm with 1 ps temporal duration. The repetition rate (f) of the laser is set at 200 kHz, the average power (P) measured before the optical window of the cryostat are $P_{\text{probe}} = 11\,\mu\text{W}$ and $P_{\text{pump}} = 35\,\mu\text{W}$. The spot sizes (d) of the beams at the sample are ~50 µm. Therefore, the pump and probe fluences[7] are $F_{\text{pump}} = 17.8\,\mu\text{J}/\text{cm}^2$ and $F_{\text{probe}} = 5.6\,\mu\text{J}/\text{cm}^2$. The sample is mounted inside the Opticool cryostat. The backscattering light is collected with the single-stage spectrometer, where a notch-filter centered at 532 nm is employed to block the elastically scattered light. We perform the measurements in the crossed polarization geometry. Additionally, we maximize the signal at overlap by preliminary pump-probe measurements inside the microscope (setup in Figure 2.9).

Firstly, we present the anti-Stokes and Stokes spectra at negative times of the average unpumped spectra. These results are shown in Figure 2.11(a-b). We point that the phonon mode has FWHM of $\sim 23.5\,\text{cm}^{-1}$, which is larger than $4-5\,\text{cm}^{-1}$ obtained with the CW laser (Figure 2.5). This is reasonable because ps-pulses are used to collect the Raman spectrum and therefore they have an intrinsic bandwith of $10-20\,\text{cm}^{-1}$.[8] A direct comparison between the

---

[7] Fluence F is measured as: $F = P/(f \cdot d^2)$.

[8] For a transform-limited pulse, the time–bandwidth product is approximately $\Delta\nu\Delta t = 0.44$ (for a Gaussian beam), giving for 1 ps time duration $\Delta\nu \sim \frac{0.44}{1\text{ ps}} = 0.44 \times \text{THz} \sim 15\,\text{cm}^{-1}$.

Stokes spectrum obtained with the CW and ps pulses is shown in Figure 2.10.

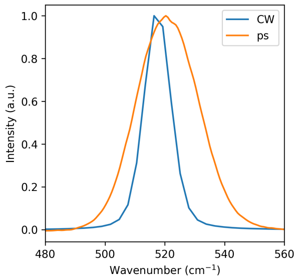

Figure 2.10: Comparison between CW and ps pulses on Si. The phonon mode of ps has FWHM of ~ $23.5\,\mathrm{cm}^{-1}$, which is larger than $4-5\,\mathrm{cm}^{-1}$ obtained with the CW laser. This is reasonable because ps-pulses are used to collect the Raman spectrum and therefore they have an intrinsic bandwith of $10-20\,\mathrm{cm}^{-1}$.

We present the TRSR measurements as a time-resolved (TR) Raman map, which is constructed as follows: the horizontal axis corresponds to Raman shift (wavenumber), the vertical axis to the pump–probe delay, and the color scale to the normalized differential signal

$$\frac{\langle R_{\mathrm{on}}\rangle - \langle R_{\mathrm{off}}\rangle}{\langle R_{\mathrm{off}}\rangle} = \frac{\Delta R}{\langle R_{\mathrm{off}}\rangle}, \tag{2.4}$$

where $\langle R_{\mathrm{off(on)}}\rangle$ denotes the average over the number of scans (and measurements) of the unpumped (pumped) spectrum. Before computing the difference, both pumped and unpumped average spectra were normalized consistently with the static Raman measurements (see Sect.2.1 and Figure A.1). The results are shown in Figure 2.11(c-d).

It is possible to see that an increase in scattering is observed on the anti-Stokes side, consistent with the creation of a transient optical-phonon population. However, in the Stokes map the negative differential signal cannot originate from a transient phonon population. Moreover, a positive shoulder is observed in the Stokes map. The integrated intensities are displayed in Figures 2.12(a–b). The integral is performed over the spectral region $\pm(510\text{–}540)\,\mathrm{cm}^{-1}$, and the value at negative delay times is subtracted from all data points. These results are in good agreement with those previously reported in [36], as shown in Figure 2.12(c).

The phonon temperature is extracted from the anti-Stokes to Stokes intensities for each delay time using the same approach that was used for the CW laser (Equation 2.3). Moreover, we exctract both temperatures from the pumped and unpumped spectra, which therefore permits us to present the differential temperature ΔT, measured as

$$\Delta T = T_{\mathrm{pump}} - T_{\mathrm{unpump}}$$

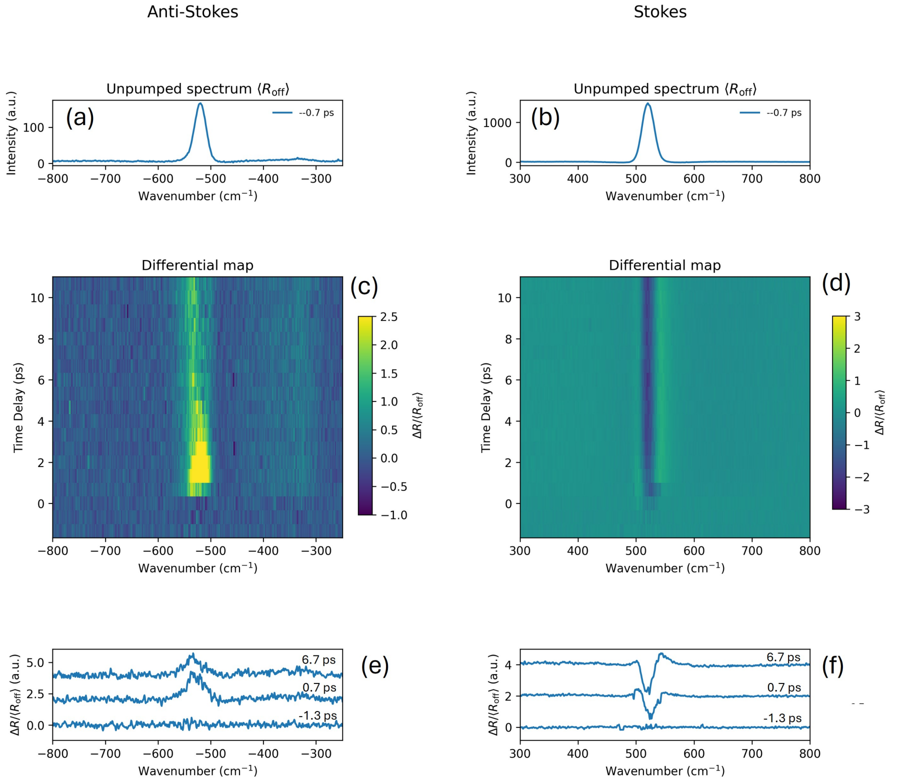

Figure 2.11: TRSR on Si at room temperature. (a) Anti-Stokes and (b) Stokes averaged spectra at -0.7 ps. The FWHM is $\sim 23.5\,\mathrm{cm}^{-1}$, which is larger than $4-5\,\mathrm{cm}^{-1}$ obtained with the CW laser (Figure 2.5). (c–d) Time-resolved Raman maps showing the normalized differential signal $\Delta R/\langle R_{\mathrm{off}}\rangle$ versus Raman shift and pump–probe delay. The anti-Stokes side exhibits a positive differential response, consistent with a transient phonon population, while the Stokes side displays a negative feature with a small positive shoulder. (e-f) displays three representative orizontal cuts of (a-b), respectively. Pump is at 700 nm and Raman probe at 523 nm. Fluences are $F_{\mathrm{pump}} = 17.8\,\mu\mathrm{J/cm}^2$ and $F_{\mathrm{probe}} = 5.6\,\mu\mathrm{J/cm}^2$, respectively.

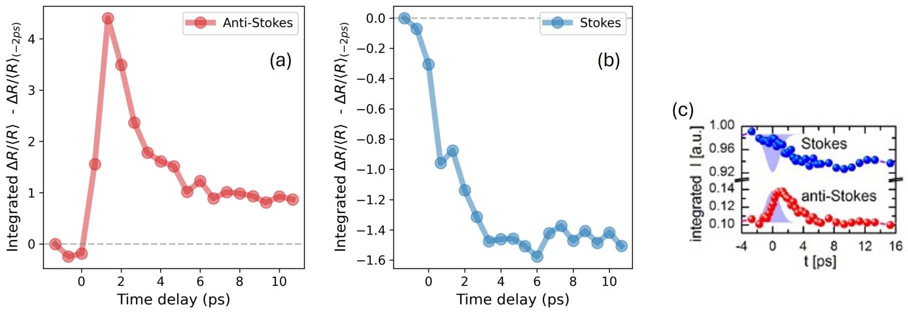

Figure 2.12: Transient Stokes and anti-Stokes phonon intensities in Si. (a) and (b) show the signals integrated over the spectral regions $-(510\text{–}540)\,\mathrm{cm}^{-1}$ (anti-Stokes) and $+(510\text{–}540)\,\mathrm{cm}^{-1}$ (Stokes), respectively. In (a), a positive signal is observed, consistent with a transient optical-phonon population, whereas the negative signal in (b) is not attributable to an increased population. These results are in good agreement with (c), reproduced from [36].

where T_{pump} and T_{unpumped} are the extracted temperatures from the pumped and unpumped spectra. The results are shown in Figure 2.13(a).

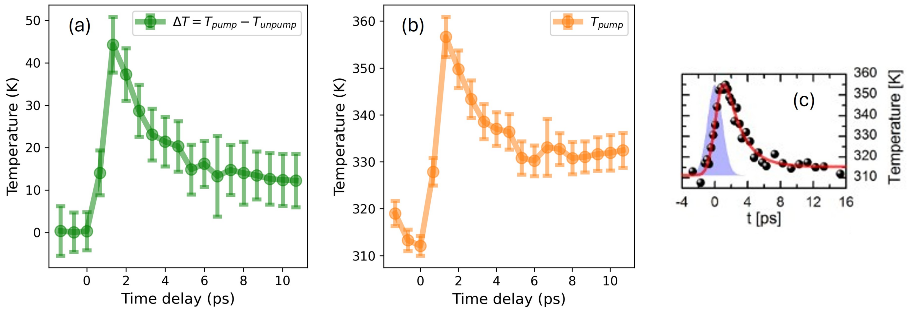

Figure 2.13: Transient Raman phonon temperature in Si. For each delay stage, we extract the temperatures from the averaged pumped (T_{pump}) and unpumped (T_{unpump}) spectra (estimated using Equation 2.3). (a) shows the differential temperature, $\Delta T = T_{\mathrm{pump}} - T_{\mathrm{unpump}}$. Immediately after photoexcitation, the temperature rises by $\sim 45\,\mathrm{K}$. (b) shows T_{pump} alone, which is in good agreement with the results reported in [36], reproduced in (c). After $\sim 10\,\mathrm{ps}$, the system reaches quasi-equilibrium at an elevated temperature of $\Delta T \sim 10\,\mathrm{K}$, about $5\,\mathrm{K}$ higher than in [36]. Error bars are obtained by standard propagation of the uncertainties in the intensities extracted from Gaussian fits to the phonon mode.

It displays a zero average temperature for negative times, while after photoexcitation ΔT rises by $45\,\mathrm{K}$ and rapidly decays. After $10\,\mathrm{ps}$, the temperature reaches quasi-equilibrium at an increased temperature of $\sim 10\,\mathrm{K}$ consistent with a long-lived thermal state of the lattice.

We display the results obtained only for T_{pump} in order to compare it with the similar measurements in [36]. We present these in Figures 2.13(b-c), respectively. Our results are in good agreement, expect for an observed increase of the quasi-equilibrium temperature, which is of ~ 5K in [36].

3

THE PHYSICS OF RUTHENATES: A BRIEF OVERVIEW

Ruthenium oxides offer a clear example of how small changes in crystal structure can steer a material between very different electronic behaviors. In this family, Sr_2RuO_4 and Ca_2RuO_4 provide two closely related yet contrasting end members, making them a natural starting point for discussing structure–property relationships in ruthenates.

In what follows, we use these parents to frame the broader $Ca_{2-x}Sr_xRuO_4$ series in which the Sr concentration is tuned. By comparing their crystal structures and overall electronic character, and then tracking how composition tunes the balance between them, we outline the main regimes that emerge across their phase diagram. The aim is to provide a guide to setting the stage for the Raman results presented in the next Chapters.

3.1 STRUCTURAL AND ELECTRONIC PROPERTIES

3.1.1 *Sr_2RuO_4*

Sr_2RuO_4 crystallizes in the tetragonal K_2NiF_4 structure with space group $I4/mmm$ (D_{4h}) and lattice parameters $a = b = 3.8603$ Å, $c = 12.729$ Å [39]. The structure is formed by layers of RuO_6 octahedra separated by Sr ions (Figure 3.1). The RuO_6 octahedra are slightly elongated along the c axis, so that the local coordination of Ru ions has tetragonal symmetry. For the tetragonal structure D_{4h}, four phonons are Raman-active [40]:

$$\Gamma_{\text{Raman}}^{(D_{4h})} = 2A_{1g} + 2E_g.$$

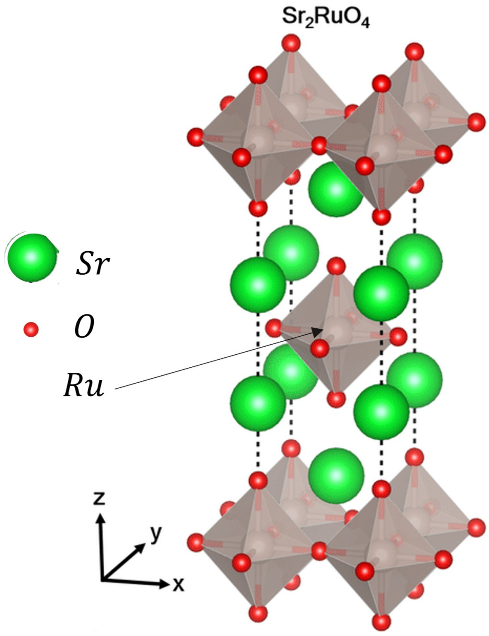

Figure 3.1: Crystal structure of Sr_2RuO_4. Green spheres indicate the Sr atoms, red the oxygens, and blue the Ru atoms. Image is taken from [41].

From a structural point of view, Sr_2RuO_4 resembles the layered cuprates, but its electronic behavior differs dramatically: instead of a Mott insulating ground state, it remains metallic down to low temperatures and exhibits unconventional superconductivity below 1 K [42], which is described as *Still a mystery after all of these years* [43] and as *Thirty years of puzzling superconductivity* [44].
In addition, its metallic behavior is described as a Fermi liquid below ~ 25 K [45], while above this temperature it is classified as a Hund metal. Although the purpose of this section is not to describe these phases in detail, we can easily argue that both regimes point to strong electronic interaction and correlations: the carriers are less free to move, and the system therefore behaves as a "bad" metal.

It is well known that the low-energy properties of Sr_2RuO_4 are determined by the 4d electrons of the Ru ions. In particular, the static electric field produced by the surrounding charge distribution of the oxygen (O) orbitals—more generally referred to as the crystal field—induces a splitting (Δ) of the five Ru 4d levels into three degenerate t_{2g} and two e_g orbitals (Figure 3.2a). Because of the stronger hybridization of the two e_g orbitals with the O 2p orbitals, the higher Coulomb repulsion makes them energetically unfavorable compared with the three t_{2g} orbitals. Therefore, in Sr_2RuO_4 the four Ru 4d electrons occupy the t_{2g} manifold, as shown by the partial density of states modeled in [46] (Figures 3.2b–c).

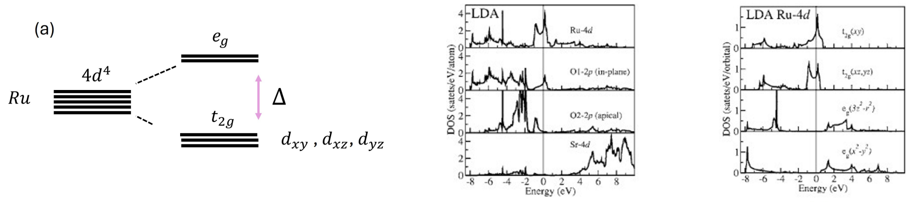

(b) (c)

Figure 3.2: Orbital levels and density of states of Sr_2RuO_4. (a) Schematic orbital configuration of the Ru 4d states. The tetragonal crystal field (Δ) splits the five degenerate 4d levels into three t_{2g} and two e_g orbitals. (b) Partial density of states Sr_2RuO_4 modeled in [46], with the Fermi level at zero. (c) Orbitally projected density of states of the Ru 4d levels. The low-energy properties of Sr_2RuO_4 are determined by the four Ru 4d electrons, which occupy the t_{2g} orbitals. (b–c) are taken from [46].

3.1.2 *Ca_2RuO_4*

Ca_2RuO_4 crystallizes in an orthorhombic structure with space group Pbca (D_{2h}), as shown in Figure 3.3. The pronounced difference with respect to the higher-symmetry tetragonal structure of Sr_2RuO_4 (Figure 3.1) lies in the smaller ionic radius of Ca ($r_{Ca} = 1.18$ Å) compared to Sr ($r_{Sr} = 1.31$ Å), which produces strong tilts and rotations of the RuO_6 octahedra (Figure 3.3). These structural distortions substantially reduce the Ru–O–Ru bond angles, leading to alternating rotations of the octahedra along the z direction, together with tilts of z relative to the ab (xy) plane, and distortions that make a and b slightly different. For the orthorhombic structure D_{2h}, 36 phonons are Raman-active [47]:

$$\Gamma^{(D_{2h})}_{\text{Raman}} = 9A_g + 9B_{1g} + 9B_{2g} + 9B_{3g}.$$

In this configuration, Ca_2RuO_4 is a Mott insulator with a metal–insulator transition (MIT) at $T_{MI} \sim 360\,K$ [49] and an antiferromagnetic ordering at $T_N \sim 110\,K$ [50, 51], where the magnetic moment of Ru are alligned along the b-axis with a small canting along c [48] (Figure 3.3).

The MIT is accompanied by a structural transition between an orthorhombic insulating phase with a short c-axis of the RuO_6 octahedra (S-Pbca), and a quasi-tetragonal metallic one with a long c-axis length (L-Pbca) [52].

Clear evidence of this transition is given by the temperature dependence of the resistivity and by the temperature dependence of the lattice constants, displayed in Figure 3.4(a) [52]. It is notable that, by lowering the temperature from 400 K to 70 K, the system exhibits an increasingly strong orthorhombic distortion that continuously reduces the volume, leading to negative thermal expansion (NTE), whose origin in transition-metal oxides such as Ca_2RuO_4 is currently under study [53].

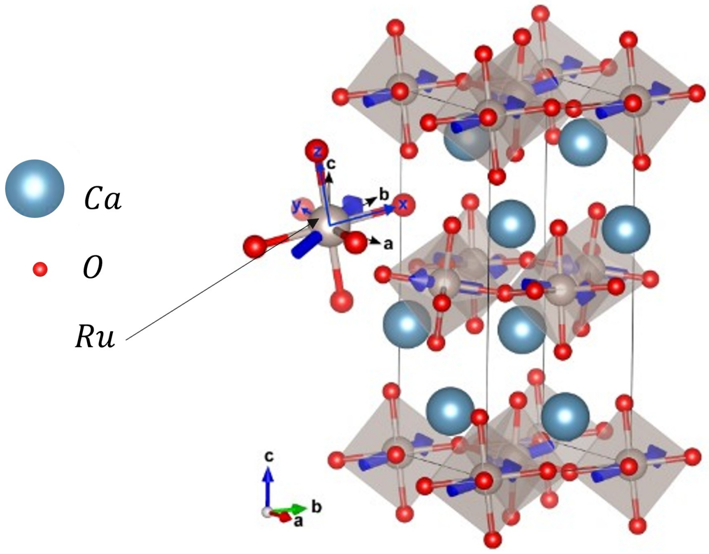

Figure 3.3: Crystal structure of Ca_2RuO_4. Gray spheres indicate the canted octahedral Ru sites, light blue spheres are calcium, and red are oxygen atoms. Blue arrows indicate the magnetic moment on each Ru site. The local xyz frame around Ru is highlighted in the inset. The smaller ionic radius of Ca ($r_{Ca} = 1.18$ Å) compared to Sr ($r_{Sr} = 1.31$ Å) produces strong tilts and rotations of the RuO_6 octahedra. See Figure 3.1 for comparison with the Sr_2RuO_4 crystal structure. Image is taken from [48].

Additionally, the system undergoes a second structural transition above 650 K, where only rotations are present and the tilt vanishes [54].

Similarly to Sr_2RuO_4, the low-energy properties of Ca_2RuO_4 are determined by the four $4d$ electrons of the Ru ions. A perfect octahedron ($c = a = b$) leads to exact degeneracy; denoting by r the average of a and b, the smaller the ratio r/c—i.e., the more elongated in the z direction the RuO_6 octahedron is—the higher in energy the d_{xy} orbital is relative to the d_{yz}–d_{xz} doublet [55].
Importantly, the transport properties are determined by the ordering of the t_{2g} levels: in the insulating short-c-axis state ($r/c > 1$), the d_{xy} orbital lies below the d_{yz}–d_{xz} doublet, with a crystal-field gap large enough that electrons tend to form pairs in the d_{xy} orbital, despite the fact that local Coulomb repulsion disfavors such an arrangement (Figure 3.4b). Following Hund's rule, the remaining two electrons occupy the d_{yz}–d_{xz} doublet with parallel spins. This configuration gives rise to an antiferromagnetic insulating order below T_N.
With further increase of temperature, the ratio r/c becomes $r/c < 1$, which pushes the d_{xz}–d_{yz} doublet below the d_{xy} level. As a result, the system becomes metallic: three electrons occupy the lowest orbitals in accordance with Hund's rule, while the fourth electron is free to move through the lattice [53]

(Figure 3.4b).

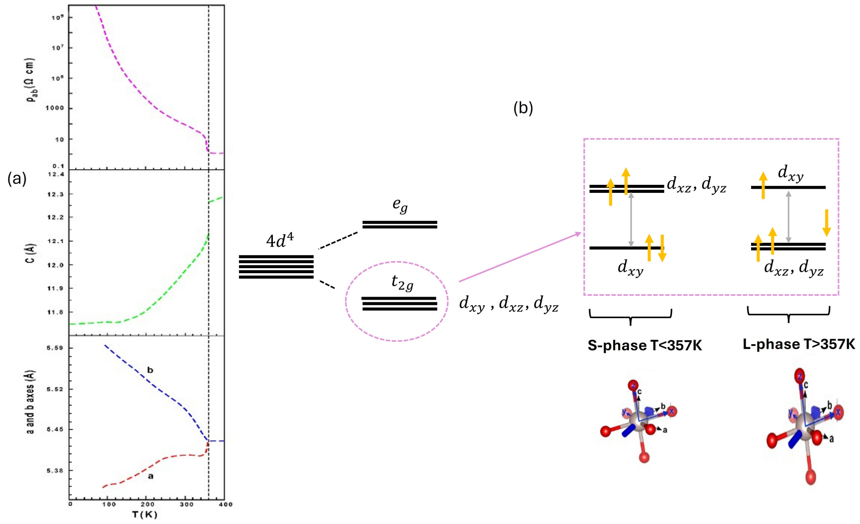

Figure 3.4: Temperature dependence of the lattice parameters of Ca_2RuO_4 and scheme of its orbital levels. (a) Temperature dependence of the resistivity (top), c lattice parameter (center), and b and a parameters (bottom). These results display the metal–insulator transition at $T_{MI} \sim 360\,K$ [49] (black dotted line), accompanied by the structural transition between an orthorhombic insulating phase with a short c-axis of the RuO_6 octahedra (S-phase), and a quasi-tetragonal metallic one with a long c-axis (L-phase) [52]. (b) Orbital-level scheme in the insulating phase (S-phase) and the metallic one (L-phase). The elongation of the octahedra along c from $T_N \to T_{MI}$ plays a crucial role for the MIT by lifting up the d_{xy} orbital until the system is in a metallic state. Orange arrows indicate the Ru spin configuration. Panel (a) is taken from [49].

Another key factor influencing the electronic properties of Ca_2RuO_4 is spin–orbit coupling. While negligible in 3d systems, dominant in 5d, and comparable to Coulomb repulsion and crystal-field splitting in 4d compounds, a recent work [56] indicates that Ca_2RuO_4 lies in the crystal-field–dominated regime, with spin–orbit coupling still playing a significant role [53].

In this context, it is worth mentioning the proposal of *excitonic magnetism* in d^4 Mott insulators such as Ca_2RuO_4 [57]. This theory is also referred to as "singlet–triplet" magnetism, which more directly reflects its nature. For Ru^{4+} ions with a t_{2g}^4 configuration, strong spin–orbit coupling stabilizes a nonmagnetic $J = 0$ singlet ground state, which would normally suppress magnetic order. The first excited states are $J = 1$ triplets lying at relatively low energies ($\sim$ 50–200 meV [57]). When the superexchange interaction[1] is of compara-

---

[1] Superexchange is an indirect exchange interaction mediated by nonmagnetic atoms (such as oxygen), allowing neighboring atoms (such as Ruthenium) to couple magnetically through virtual electron hopping.

ble strength (50–100 meV [57]), virtual excitations into these triplet states can mix with the singlet background. Once such triplet excitations ("excitons") are sufficiently populated, they "condense" and generate effective magnetic moments, which then order antiferromagnetically. In this picture, magnetism in Ca_2RuO_4 does not arise from pre-existing local moments of Ru^{4+} ions but from the collective condensation of excited states, a phenomenon described as excitonic magnetism. A schematic representation is shown in Figure 3.5. For further details, a microscopic description of this mechanism in Ca_2RuO_4 is presented in [57].

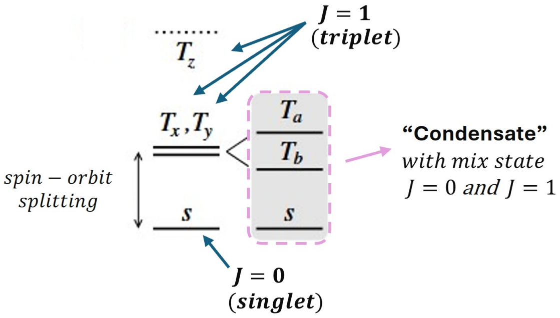

Figure 3.5: Excitonic or "singlet–triplet" magnetism. Spin–orbit coupling (SOC) splits the $J = 0$ (singlet) and $J = 1$ (triplet) levels. When the superexchange interaction is comparable to SOC, triplet excitations can form and, under suitable conditions, condense (pink region), giving rise to effective magnetic moments that order antiferromagnetically. This explains the presence of antiferromagnetism in Ca_2RuO_4 despite its nominal $J = 0$ ground state. Image adapted from [58]. The detailed splitting of the triplet (T) levels is beyond the scope of this section and will be discussed later in Chapter 5.

3.2 PHASE DIAGRAM OF CA$_{2-x}$SR$_x$RUO$_4$

The dramatic difference between Sr_2RuO_4 and Ca_2RuO_4 highlights the central role of lattice distortions in ruthenates. Sr_2RuO_4 with undistorted octahedra is metallic and superconducting, while Ca_2RuO_4 with tilted octahedra is a correlated insulator with antiferromagnetic (AF) order. Therefore, by changing the Sr-concentration (x) in $Ca_{2-x}Sr_xRuO_4$, it is expected that it reduces the octahedral tilts, increases the Ru–O–Ru bond angles, and enhances the electronic bandwidth. This results in a rich (x, T) phase diagram [59], as shown in Figure 3.6, where c is the concentration of Sr atoms. In the following, we highlight three regions:

- **Region I ($x < 0.2$):** the distortions (rotations+tilting) are maximal and lead to a canted AF insulating ground state (CAF–I) and a metal–insulator transition ($T_{M/NM}$). For $x = 0$, the system remains insulating up to 360 K and exhibits antiferromagnetic order below 110 K.

- **Region II** ($0.2 < x < 0.5$)**:** "Magnetic metallic (M–M) region". $x \sim 0.5$ corresponds to a novel crossover between the nonmagnetic (region III) and magnetic (region I-II) phases, which is evidenced by a critical enhancement of the low-temperature susceptibility [59].
- **Region III** ($x > 0.5$)**:** the system is nonmagnetic and behaves as a good Fermi liquid (FL) and Hund metal (H–M), becoming an unconventional superconductor (SC) at $T_c \sim 1.5$ K only for $x = 2$. In this region, the rotations are estinguished at $x = 0.5$ and only the tilting along c axis is present until $x = 2$.

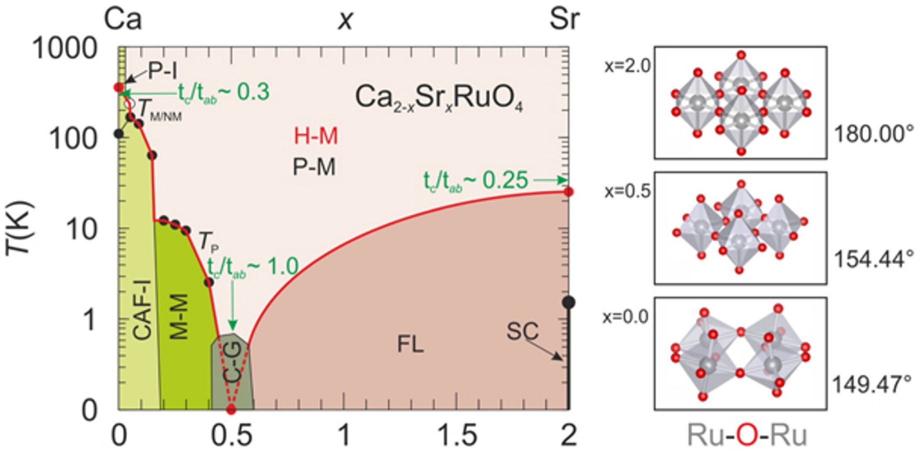

Figure 3.6: Phase diagram of Ruthenates. The x-axis shows the Sr content, while the y-axis shows the temperature on a logarithmic scale. Light green corresponds to the canted antiferromagnetic transition in the insulating state (CAF–I); green to the metallic–magnetic state (M–M); red to the Fermi-liquid state (FL); and black to the superconducting state (SC). The red line marks the transition to a Hund metal (H–M), while the black line marks the paramagnetic state (P–M). The diagram shows that increasing Sr concentration reduces the octahedral tilts and increases the Ru–O–Ru bond angles, which leads to a plethora of phase transitions. Image is from [60]

.

3.2.1 *Magnetic Phase Diagram and Lattice Distortions*

We report the theoretical predictions [61] of first-principles calculations that explicitly vary the three octahedral distortions—rotation (ϕ) about c, tilting (θ)

about an in-plane edge, and flattening $\lambda = c/r$—and compare the magnetic ground states (NM, FM, AF) at each fixed structure (Figure 3.7a).[2]
Mapping these structural parameters to composition using neutron data [50, 52] shows that Sr_2RuO_4 sits at $\phi = \theta = 0°$, $Ca_{1.5}Sr_{0.5}RuO_4$ has strong rotation but vanishing tilt ($\phi \sim 12.8°$, $\theta = 0°$), and Ca_2RuO_4 combines comparable rotation with sizable tilt ($\phi \sim 11.9°$, $\theta \sim 12°$). From $x = 2 \to 0.5$ the flattening remains nearly constant ($\lambda \sim 1.07$), whereas from $x = 0.5 \to 0$ the rotation is essentially fixed while the tilt grows. These trends alone reproduce the sequence of magnetic tendencies across the series: rotations drive a NM→FM instability, while the subsequent addition of tilt (together with flattening) stabilizes staggered AF order (Figure 3.7b).

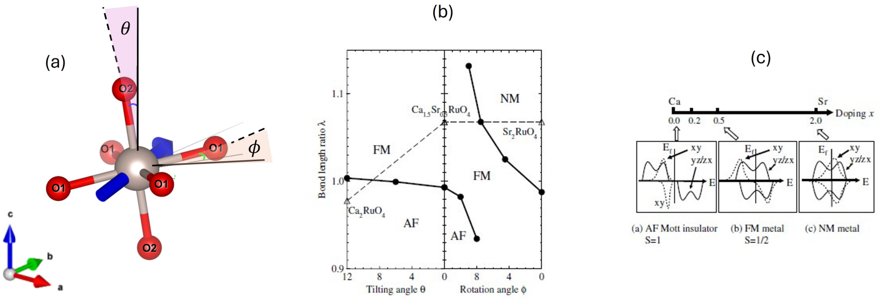

Figure 3.7: Magnetic phase diagram of ruthenates. (a) Sketch of the octahedral rotation (ϕ) and tilting (θ). (b) Magnetic phase diagram as a function of θ, ϕ, λ, where $\lambda = c/r$ with r the average of a and b lattice parameters. Triangles are experimental data; black lines are theoretical predictions from [61]. (c) Schematic projected density of states (PDOS) for the three representative cases: Ca_2RuO_4, $Ca_{0.5}Sr_{1.5}RuO_4$, and Sr_2RuO_4. (a) adapted by [48], (b)-(c) from [61].

Microscopically, the magnetic properties are attributed to the cooperative occupation of the t_{2g} orbitals at all Ru sites. In particular, the projected density of states (Figure 3.7c) shows that in the case of $x = 0$, the d_{xy} orbitals are fully occupied while the d_{xz} and d_{yz} are half-filled [61]. This configuration suggests a localized spin picture of $S \sim 1$ (although inter-site hybridization modifies the picture quantitatively and gives rise to a more exotic form of magnetism known as excitonic magnetism [57]). The stabilization of the AF state is mainly due to the strong super-exchange interaction between the occupied majority-spin and unoccupied minority-spin $d_{yz/zx}$ orbitals [61]. The d_{xy} orbital does not contribute to exchange interactions due to its nearly full occupation.

By going from $x = 0 \to 0.2$, the splitting between d_{xz} and $d_{yz/zx}$ is reduced due to the decrease of flattening, moving away from the orthorhombic struc-

---

[2] r stands for the average between the a and b lattice parameters.

ture and toward the tetragonal one. This splitting is consistent with what was previously observed when explaining the metal–insulator states of Ca_2RuO_4 (Figure 3.4), where elongation of the octahedra lifts up the d_{xy} orbital. Therefore, the AF state becomes less stable because the occupation of the d_{xy} orbital is partially suppressed by elongation of the Ru–O bond along the c-axis. This is consistent with the reduced Néel temperature T_N observed in the phase diagram (Figure 3.6).

For $x = 0.5$, the absence of tilting θ results in a broadening of the d bands, with the $d_{yz/zx}$ most affected since decreasing θ primarily reduces the overlap between them and the apical O-2p orbitals (Figure 3.7c). The persistence of rotation ϕ keeps the d_{xy} states narrow. Overall, the $x = 0.5$ case may correspond to an $S \sim 1/2$ picture, where the d_{xy} orbital contributes to the magnetic moment [61]. This picture agrees with Curie–Weiss susceptibility fits showing $S = 1/2$ [59].

Moving from $x = 0.5 \rightarrow 2$, the decrease of ϕ leads to a broadening and upward shift of the d_{xy} band, bringing the system into a non-magnetic state (Figure 3.7c).

4

RAMAN SCATTERING FROM RUTHENATES

In this chapter, we exploit static Raman scattering to gain insigth into the symmetry of the vibrational modes in ruthenate samples, to track their phase transitions as a function of temperature, and to assess how temperature influences the Raman response of these compounds. The ruthenates studied in the present thesis are the parent compounds Ca_2RuO_4, Sr_2RuO_4 and three different Sr-doped Ca-based $Ca_xSr_{2-x}RuO_4$ compounds (x=0.1,0.2,0.3 Sr doping). Therefore, various regions of the temperature-doping phase diagram can be explored (Figure 3.6).
Raman spectroscopy allows us to investigate the vibrational and magnetic excitations of the samples, exploring the symmetry of these excitations and its temperature dependence.

The aim of this chapter is twofold.
Firstly, the symmetry of the phonons is investigated at room temperature. We used this information to identify the symmetry of the Raman modes. This part is presented starting from Sr_2RuO_4 and Ca_2RuO_4 to the Sr-doped Ca-based compounds.
Secondly, we exploit Raman scattering to explore the effect of the thermal phase transitions in ruthenates on the lattice and magnetic dynamics.
In Ca_2RuO_4, we investigate the antiferromagnetic transition, the temperature dependence of the electron-phonon interaction and a possible evidence of the orbital-ordering transition occuring in the insulating paramagnetic phase.
In Sr_2RuO_4 we exploit Raman scattering to unveil signatures of a possible transition to a Fermi liquid state at low temperatures (Figure 3.6).
In the doped samples $Ca_{2-x}Sr_xRuO_4$ with $x = 0.2$ and $x = 0.3$ a structural phase transition occuring in the metallic phase is reported, and it is discussed its behaviour as a function of the Sr-doping of the ruthenate compounds. Lastly, we report a comparison between the insulating state of Ca_2RuO_4 and the metallic one of the Sr-doped compounds.

4.1 POLARIZATION DEPENDENCE OF THE RAMAN MODES

A crucial step in Raman experiments is the choice of polarization geometry, since the Raman tensor components transform according to the symmetries of the crystal (see Chapter 1). In our measurements we use a back-scattering geometry, with the polarizations of the incident and scattered light lying in the xy-plane. In Porto notation this corresponds to configurations $z(xx)\bar{z}$ or $z(xy)\bar{z}$. [1] All the polarization-dependent measurements were performed at room temperature and using the *Room-temperature in-air Raman set-up* (Figure 2.2).

All of the samples studied have a tetragonal structure at room temperature, except for Ca_2RuO_4, which is orthorhombic (Chapter 3). Both structures exhibit the same in-plane symmetry; the only difference is that in the orthorhombic case $a \neq b$. This small anisotropy does not qualitatively affect the irreducible symmetries allowed for the polarization of light in the RuO_2 octahedral plane (ab), which are A_g and B_{1g}. In particular, these two symmetries are maximized in parallel and crossed polarization configurations, respectively.

To isolate the contributions of the A_g and B_{1g} Raman modes, following the approach of [58], we aligned the incident and scattered polarization vectors at 45° with respect to the Ru–Ru bonds. In this way, the parallel configuration selectively probes the A_g modes, while the crossed configuration enhances the B_{1g} modes. In Porto notation, these correspond to $z(x'x')\bar{z}$ and $z(x'y')\bar{z}$, where x' and y' are obtained by rotating x and y by 45°, respectively. The scheme of these configurations is shown in Figure 4.1.

Since the polarization of the outgoing light is fixed in order to maximize the efficiency of the spectrometer gratings, and because the two configurations of interest are parallel and crossed, we cannot rotate both polarizations simultaneously. For this reason, we fixed the polarizations of both the incident and scattered light, and instead rotated the sample under the microscope. To switch between parallel and crossed geometries, we simply rotated the incident polarization by 90°.

If a Raman mode has A_g symmetry, its intensity is not expected to vary with the orientation of the sample, since this mode is total symmetric and does not alter the polarization of the outgoing beam. By contrast, the intensity of a B_{1g} mode depends strongly on the orientation. In particular, the signal is maximized when the sample is aligned as shown in Figure 4.1(b) and extinguished

---

[1] In a Raman spectroscopy experiment, a laser beam is fired at a sample and the spectrum of the beam scattered in a given direction is analyzed. Using Porto notation, the geometry of a Raman experiment will be denoted as $a(bc)d$, with $a(d)$ direction of the propagation of the incident (analyzed) beam and $b(c)$ polarization direction of the incident (analyzed) beam [62].

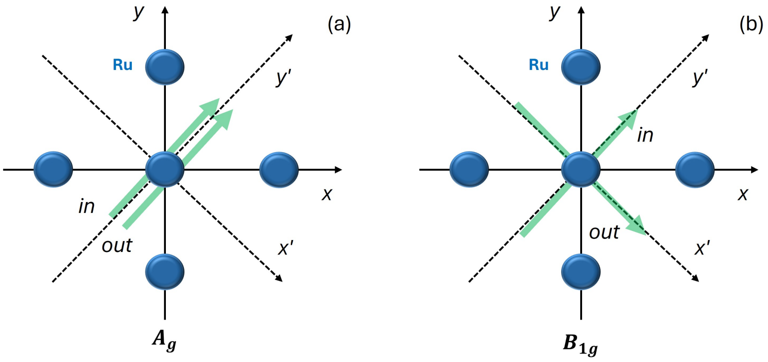

Figure 4.1: Polarization scheme: Polarization vectors of the incoming and outgoing photons (green arrows) with respect to the Ru lattice for A_g (a) and B_{1g} (b) symmetries. The polarizations are oriented at 45° relative to the Ru–Ru bonds. Scheme adapted from [58]. The A_g and B_{1g} geometries correspond in Porto notation to $z(x'x')\bar{z}$ and $z(x'y')\bar{z}$, respectively.

when it is aligned as shown in Figure 4.1(a). In the following, when we refer to A_g and B_{1g} geometries, we specifically mean the configurations shown in Figures 4.1(a) and 4.1(b), respectively. Once the sample orientation is determined, we can switch between A_g and B_{1g} geometries simply by rotating the polarization of the incident light by 90°.

4.1.1 Sr_2RuO_4

Figure 4.2 shows the Raman measurements at room temperature for the following orientations of the sample in the xy (ab) plane by maintening fixed the relative polarization between the incoming and the scattered light: 5°, 25°, 45°, 65°, 85°, 95°. In particular, Figure 4.2(a) shows the Raman spectra collected in the parallel configuration, while in Figure 4.2(b) the Raman spectra collected in the crossed configuration.

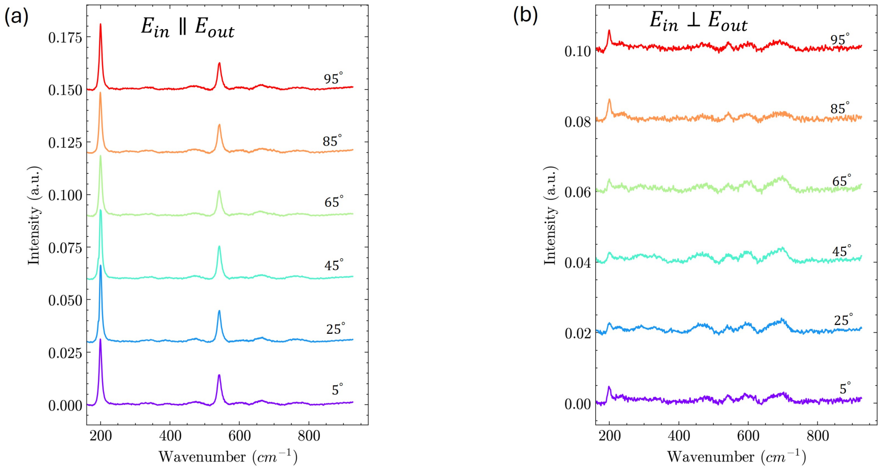

Figure 4.2: Polarization study in the ab plane for Sr_2RuO_4 at 300K: Raman spectra collected with different orientations of the sample in the ab plane (xy). In (a-b) is shown, respectively, the parallel and crossed configurations. Two phonon modes are present in the parallel configuration. There is no preferential orientation of the sample.

In Figure 4.4(a) are present two peaks, one at 200 cm^{-1} and one at 542 cm^{-1}. The phonon energy of them agrees well with the literature [40]. The mode at 200 cm^{-1} corresponds to the in-phase motion between Sr and apical oxygen, while the one at 542 cm^{-1} to the vibration of the apical oxygen along the c axis [63]. In Figure 4.4(b) pronounced peaks are not present. There is a residual of the peak at 200 cm^{-1}, which is close to the background intensity. The absence of B_{1g} modes is reasonable. Indeed, this reflects the high symmetry of the octahedra, which leads to a degeneracy and more symmetric (as A_g symmetry) of the phonon modes.

For a more quantitative analysis, we did the polar plot of these modes. The results are reported in Figure 4.3, where is shown the area under the peaks with respect to the angle of orientation. The window of integration is ± 7 cm^{-1} with respect to the central phonon frequencies.
It is clear that these two phonon modes are total-symmetric. In fact, they do not depend on the orientation of the sample with respect to the incident light. This analysis confirms the A_g symmetry of these modes [40]. Since there are no preferential axes of orientation, the sample is mounted in an arbitrary direction. We use this "configuration" for all of the following measurements of Sr_2RuO_4 presented in this thesis.

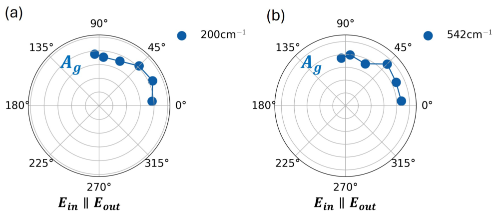

Figure 4.3: Polar plots of the A_g modes in Sr_2RuO_4 at 300K: integrated intensity of the modes for different orientations of the sample in the ab plane (xy). In (a-b) is shown the A_g symmetry for the peaks at $200, 542\ cm^{-1}$, respectively.

4.1.2 *Ca_2RuO_4*

In this section, we present the polarization-dependent Raman scattering on the Ca_2RuO_4 compound.
Figure 4.4(a)-(b) show the room temperature Raman spectra obtained with different orientation of the sample by maintening fixed the relative polarization between the incoming and the scattered light. Since the in-plane symmetry of the octahedra is invariant under 90° rotations, we report two measurements at equivalent angles[2], indicating in parentheses the corresponding difference from 45°. In particular, Figure 4.4(a) corresponds to the parallel configuration and Figure 4.4(b) to the crossed.

In Figure4.4(a)-(b) we note the emergence of new Raman modes with respect to the one observed in Sr_2RuO_4 (Figure 4.2). The presence of a richer phonons structure in both the parallel and cross configuration highlights a lower simmetry structure, hence compatible with a distortion of the RuO_6 octahedra with respect to the undistorted case ($SrRuO_4$) (Figure 4.2). The nature of these modes will be discussed in more details in the next section (4.2.1.1) where their temperature-dependent behavior will be discussed, together with DFT simulations of the lattice dynamics. We label the phonons used for the next analysis. In particular, for the A_g phonons we use the same labels as reported in the next section 4.2.1.1 (Figure 4.17-4.18).

In Figures 4.5(a-d) are presented the polar plots of the parallel configuration for the A1, A6, A8, A11 Raman modes (see Figure 4.4a). The A11 mode might correspond to the highest energy mode reported previously for Sr_2RuO_4 (Fig-

---

[2] In order to know these angles, we follow this procedure. We mount the sample on a rotational stage with respect of an arbitrary configuration. Then, we collect the Raman spectra at different angles. Once obtained the spectra, we identify the angle at which the B_{1g} phonons are maximed and set this angle as 45°. After that, we re-scale all of the remaining angles with respect of this. We follow this procedure for the similar analysis of the doped compounds in Sections 4.1.3-4.1.4-4.1.5.

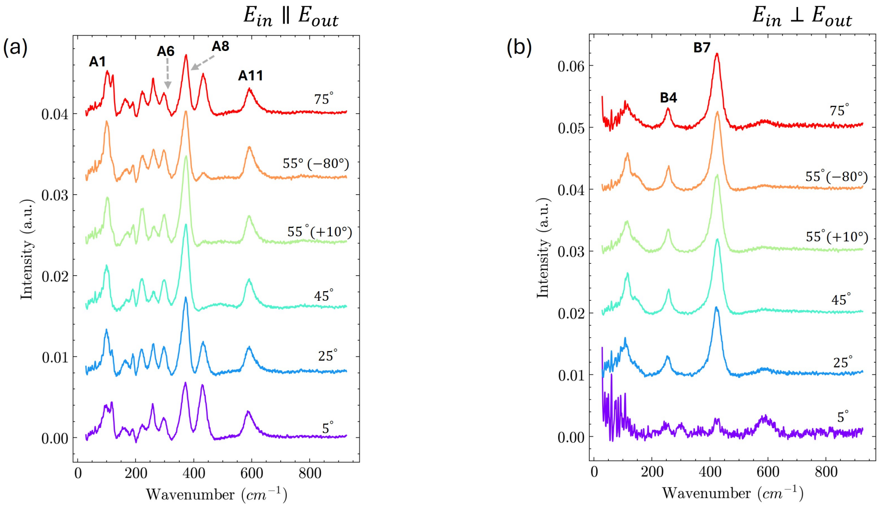

Figure 4.4: Polarization study in the ab plane of Ca_2RuO_4 at 300K: Raman spectra collected with different orientations of the sample in the ab plane (xy). In (a)-(b) is shown, respectively, the parallel and crossed configurations. Parentheses indicate the difference of the starting angles from 45°. In both cases the resulting value is 55°, obtained once as $45° - 80°$ and once as $45° + 10°$, consistent with the 90° rotational symmetry of the system. The B_{1g} configuration corresponds to 45° when B7 is minimum in the parallel configuration and maximum in the crossed. The phonons used for the next analysis are labeled and indicated by arrows.

ure 4.2a). It preserves the same symmetry with removing Sr content. These polar plots clearly show the A_g symmetry of these modes.

Figure 4.6(a)-(b) and Figure 4.6(c)-(d) show B_{1g} symmetry for B4 and B7 modes (see Figure 4.4b). In particular, Figure 4.6(a)-(c) correspond to the crossed configuration, while Figure 4.6(b)-(d) to the parallel configuration. The B_{1g} channel is mainly caracterized by B7 mode.

We orient the sample at 45°, which corresponds to the B_{1g} symmetry, at which the B7 phonon is maximized in crossed and minimized in parallel configuration. This matches with the polarization scheme shown previously in Figure 4.1, which allows us to switch between A_g and B_{1g} geometries by changing from parallel to crossed polarization.

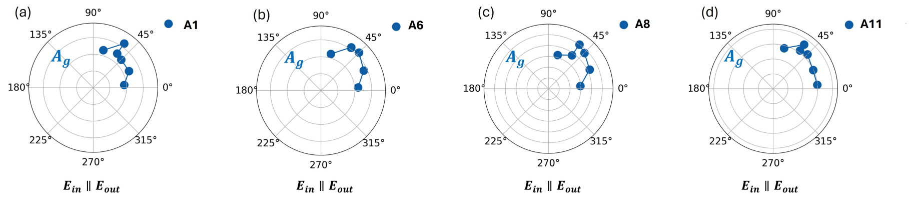

Figure 4.5: Polar plots of the Ca_2RuO_4 A_g modes at 300K: integrated intensity of the modes for different orientations of the sample in the ab plane (xy). In (a)-(b)-(c)-(d) is shown the A_g symmetry of A1, A6, A8, A11 modes, respectively.

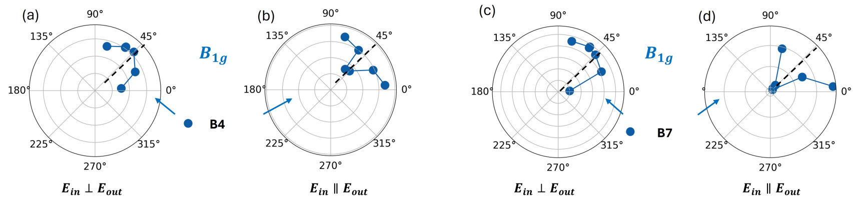

Figure 4.6: Polar plots of the Ca_2RuO_4 B_{1g} modes at 300K: integrated intensity of the modes for different orientations of the sample in the ab plane (xy). In (a)-(b) is shown the B_{1g} symmetry for B4 mode, while (c)-(d) for B7. The B_{1g} symmetry is underlined from the evidence that a maximum in the crossed configuration (a)-(c) at 45° corresponds to a minimum in the parallel configuration (b)-(d).

4.1.3 $Ca_{1.7}Sr_{0.3}RuO_4$

In this section, we present the polarization-dependent Raman scattering of the x = 0.3 Sr-doped compound $Ca_{2-x}Sr_xRuO_4$. Figure 4.7(a)-(b) show the room temperature Raman spectra obtained with different orientation of the sample. In particular, Figure 4.7(a) corresponds to the parallel configuration and Figure 4.7(b) the crossed.

In Figure 4.7(a) three peaks are present at all of the angles, which we label as C1, C2, C3; while one at 427cm^{-1} (D2) is maximum at 85° and minimum at around 45°.
The first three peaks correspond with the following energies: 249, 323, 572cm^{-1}. Regarding the nature of these Raman modes, one possible suggestion is given later in this thesis looking at the spectrum at low temperature and compared it with the phonon modes of Ca_2RuO_4 (Section 4.2.3.1). C3 might be related to the one observed in Sr_2RuO_4, which corresponds to the vibration of the apical oxygen along the c axis [63].
In Figure 4.7(b) one peak (D2) at around 427cm^{-1} is the only visible mode, which disappears at 65°. In [64], they try to attribute this mode to the apical oxygen vibration.

In order to show clearly the symmetry of these phonon modes, we integrate

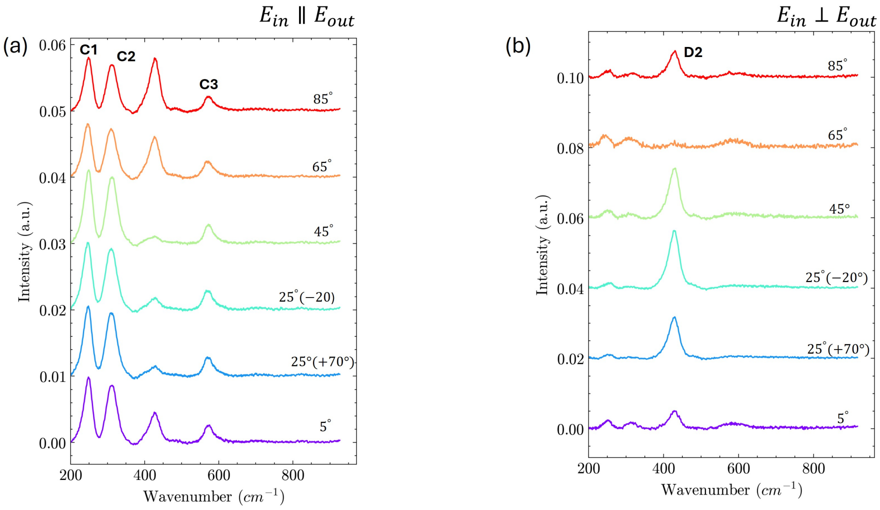

Figure 4.7: Polarization study in the ab plane for $Ca_{1.7}Sr_{0.3}RuO_4$ at 300K: Raman spectra collected with different orientations of the sample in the ab plane (xy). In (a)-(b) is shown, respectively, the parallel and crossed configurations. Parentheses indicate the difference of the starting angles from 45°. In both cases the resulting value is 25°, obtained once as $45° - 20°$ and once as $45° + 70°$, consistent with the 90° rotational symmetry of the system. The B_{1g} configuration corresponds to 45° when D2 is minimum in the parallel configuration and maximum in the crossed.

the spectral weigth below the observed phonon modes and plot them in the polar plot presented in Figures 4.8-4.9.
Figure 4.8(a-c) confirm the A_g symmetry of C1, C2, C3, respectively. Indeed, the intensity of them does not depend on the orientation of the incoming light in the xy (ab) plane.
Figure 4.9 displays the B_{1g} symmetry of D2. In particular, Figure 4.9(a)-(b) display the crossed and parallel configuration, respectively. It appears clearly that the minimum of the integrated intensity at 45° calculated in the parallel configuration corresponds to a maximum in the crossed configuration.

The richer phonon structure observed in both parallel and crossed configurations indicates a lower-symmetry state compared to the tetragonal phase of Sr_2RuO_4, consistent with distortions of the RuO_6 octahedra. Conversely, the reduced number of phonon modes compared to orthorhombic Ca_2RuO_4 shows that the system retains a higher symmetry than the most distorted crystalline phase of Ca_2RuO_4.
Similarly with Ca_2RuO_4, we orient the sample at 45°, which corresponds to the angle at which the B_{1g} phonon (D2) [64] is minimized in the parallel configuration and maximized in the crossed configuration.

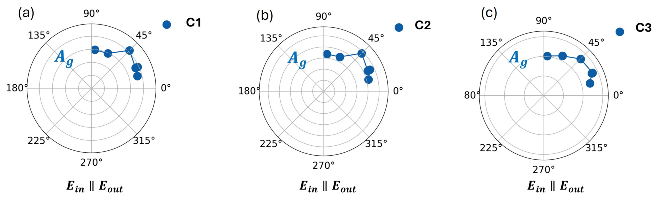

Figure 4.8: Polar plots of the $Ca_{1.7}Sr_{0.3}RuO_4$ A_g modes at 300K: integrated intensity of the modes for different orientations of the sample in the ab plane (xy). In (a)-(b)-(c) is shown the A_g symmetry for C1, C2, C3.

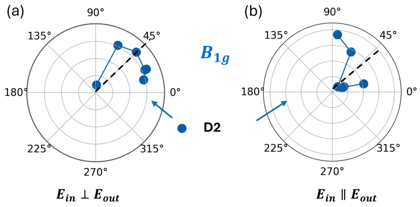

Figure 4.9: Polar plots of the $Ca_{1.7}Sr_{0.3}RuO_4$ B_{1g} modes at 300K: integrated intensity of the modes for different orientations of the sample in the ab plane (xy). In (a)-(b) is shown the B_{1g} symmetry of D2. The B_{1g} symmetry is underlined from the evidence that the minimum in the parallel configuration (b) corresponds to a maximum in the crossed configuration (a).

4.1.4 $Ca_{1.8}Sr_{0.2}RuO_4$

In this section, we present the polarization-dependent Raman scattering on the x = 0.2 Sr-doped compound $Ca_{2-x}Sr_xRuO_4$. Figures 4.10(a)-(b) show the room temperature Raman spectra obtained with different orientation of the sample. In particular, Figure 4.10(a) corresponds to the parallel configuration and Figure 4.10(b) the crossed. There are no significant differences in both parallel and cross polarizations with respect of what was previously observed in the higher doped-compound (x=0.3) in Figure 4.7.

In Figures 4.11(a-c) we present the polar plot of the parallel configuration for C1, C2, C3. These modes have the same A_g symmetry previously reported for the doped sample with x=0.3 (Figure 4.8).
Figure 4.12 shows the polar plot of D2 in the crossed configuration (a) and in the parallel configuration (b). The minimum in the parallel configuration at 45° corresponds with a maximum in the crossed configuration.

The similarity in the Raman spectra between the $x = 0.2$ and $x = 0.3$-Sr doped compounds can be justified by looking at their phase diagram (Figure 3.6). The absence of a metal-to-insulator transition as well as the absence of an anti-ferromagnetic order at low temperatures suggest indeed a similar distorsion of the ochaedra cells in the two doped compounds.

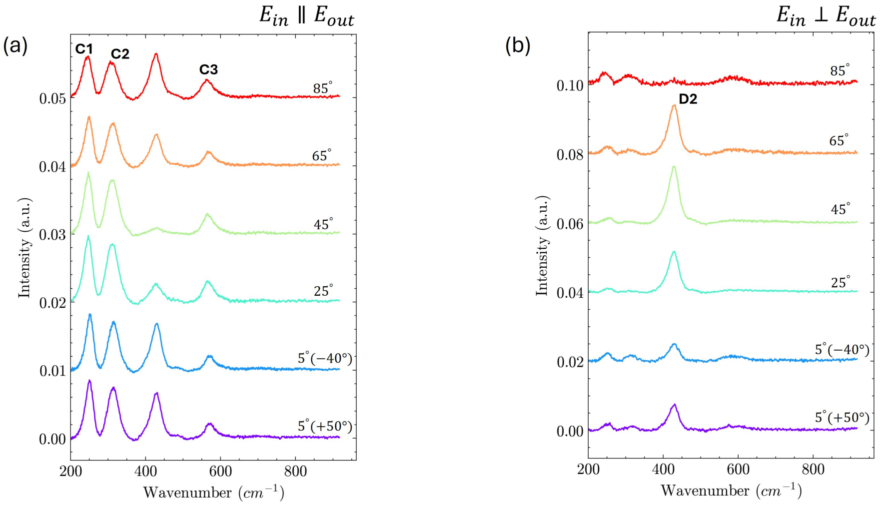

Figure 4.10: Polarization study in the ab plane for Ca$_{1.8}$Sr$_{0.2}$RuO$_4$ at 300K: Raman spectra collected with different orientations of the sample in the ab plane (xy). In (a)-(b) is shown, respectively, the parallel and crossed configurations. Parentheses indicate the difference of the starting angles from 45°. In both cases the resulting value is 5°, obtained once as $45° - 40°$ and once as $45° + 50°$, consistent with the 90° rotational symmetry of the system. The B$_{1g}$ configuration corresponds to 45° when the peak at 436 cm^{-1} (D2) is minimum in the parallel configuration and maximum in the crossed. There are no substantial deviations in both polarizations with respect of what was previously observed in the higher doped-compound (x=0.3) in Figure 4.7.

We orient the sample at 45° for the same reasons discussed for the previous compounds.

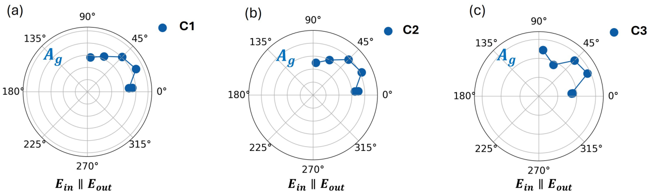

Figure 4.11: Polar plots of the $Ca_{1.8}Sr_{0.2}RuO_4$ A_g modes at 300K: integrated intensity of the modes for different orientations of the sample in the ab plane (xy). In (a)-(b)-(c) is shown the A_g symmetry for C1, C2, C3, respectively.

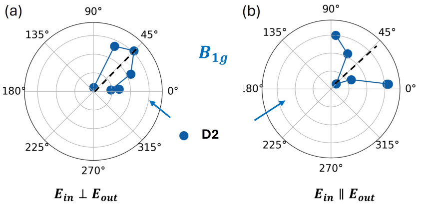

Figure 4.12: Polar plots of the $Ca_{1.8}Sr_{0.2}RuO_4$ B_{1g} modes at 300K: integrated intensity of the modes for different orientations of the sample in the ab plane (xy). In (a)-(b) is shown the B_{1g} symmetry of D2. The B_{1g} symmetry is underlined from the evidence that the minimum in the parallel configuration (b) corresponds to a maximum in the crossed configuration (a).

4.1.5 *$Ca_{1.9}Sr_{0.1}RuO_4$*

In this section, we present the polarization-dependent Raman scattering on the x = 0.1 Sr-doped compound $Ca_{2-x}Sr_xRuO_4$. Figure 4.13(a)-(b) show the room temperature Raman spectra obtained with different orientation of the sample. In particular, Figure 4.13(a) corresponds to the parallel configuration and Figure 4.13(b) the crossed.

The corresponding three Ag peaks C1, C2, C3 observed in the previous doped samples are still present. D2 presents a similar behavior to what reported previously for the higher doped compounds (Figures 4.7-4.10).
However, there is one feature which is absent for the other dopings: one more Raman phonon (D1) around $364\,\mathrm{cm}^{-1}$ in the parallel configuration. This mode depends on the orientation of the sample and is not clearly visible in the crossed configuration. The nature of this mode can be associated to the presence of a second-order structural phase transition above room temperature, similarly to what reported in [65] and in the samples at low temperature with a higher Sr doping (see Sect. 4.2.3.2).

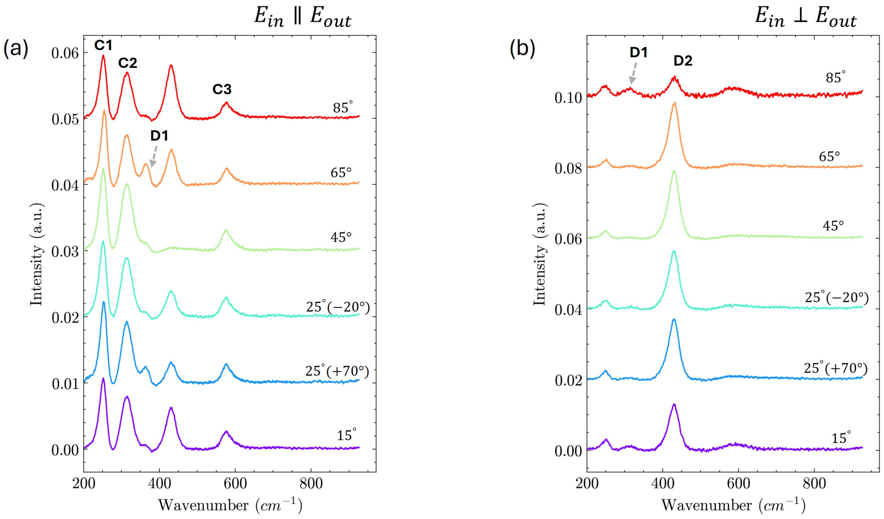

Figure 4.13: Polarization study in the ab plane for $Ca_{1.9}Sr_{0.2}RuO_4$ at 300K: Raman spectra collected with different orientations of the sample in the ab plane (xy). In (a)-(b) is shown, respectively, the parallel and crossed configurations. Parentheses indicate the difference of the starting angles from 45°. In both cases the resulting value is 25°, obtained once as $45° - 20°$ and once as $45° + 70°$, consistent with the 90° rotational symmetry of the system. The B_{1g} configuration corresponds to 45° when D2 is minimum in the parallel configuration and maximum in the crossed. It is noticeable one more Raman phonon (D1) around $364\,cm^{-1}$ in the parallel configuration.

In Figure 4.14(a-c) are presented the polar plot of the parallel configuration for the three modes C1, C2, and C3. These modes have the same A_g symmetry previously reported for the doped sample with x=0.2,0.3 (Figures 4.8-4.10).
Figure 4.15(a)–(b) and Figure 4.15(c)–(d) show the possible B_{1g} symmetry of D1 and D2. In particular, Figure 4.15(a) and (c) correspond to the crossed configuration, while Figure 4.15(b) and (d) correspond to the parallel configuration. Whereas D2 clearly exhibits B_{1g} symmetry, this is not the case for D1. In fact, in the parallel configuration D1 does not reach a minimum only at 45°, and in the crossed configuration it shows two maxima. Moreover, examining the spectra in Figure 4.13(b), the intensity of this peak in the crossed configuration is comparable to the background, which affects the reliability of this analysis. We report these considerations because we expect A_g symmetry for this mode by comparison with samples at lower Sr doping (see Sect. 4.2.3.2) and with [65] for x=0.3.
We orient the sample at 45° for the same reasons discussed for the previous compounds.

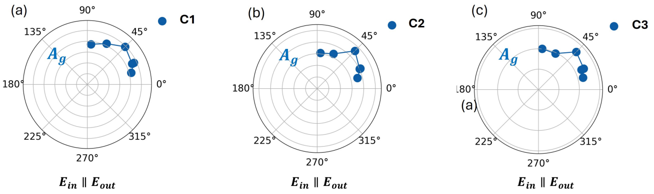

Figure 4.14: Polar plots of the Ca$_{1.9}$Sr$_{0.1}$RuO$_4$ A$_g$ modes at 300K: integrated intensity of the modes for different orientations of the sample in the ab plane (xy) with respect to an arbitrary initial configuration. In (a)-(b)-(c) is shown the A_g symmetry for C1, C2, and C3, respectively.

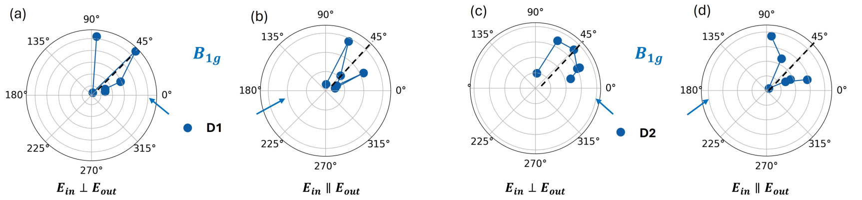

Figure 4.15: Polar plots of the Ca$_{1.9}$Sr$_{0.1}$RuO$_4$ B$_{1g}$ modes at 300K: integrated intensity of the modes for different orientations of the sample in the ab plane (xy) with respect to an arbitrary initial configuration. In (a)-(b) is shown the B_{1g} symmetry for the peak D1, while (c)-(d) for D2. The B_{1g} symmetry of D2 is underlined from the evidence that the minimum in the crossed configuration (a) corresponds to a maximum in the parallel configuration (b), whereas for D1 the behavior is not unambiguously consistent with B_{1g} symmetry.

4.2 TEMPERATURE-DEPENDENT RAMAN SCATTERING FROM RUTHENATES

In the second part of this chapter, we investigate the temperature dependence of the Raman scattering in Ca_2RuO_4, Sr_2RuO_4, and $Ca_{2-x}Sr_xRuO_4$ with $x = 0.2, 0.3$. Specifically, this section is divided into three parts: Ca_2RuO_4, Sr_2RuO_4, and $Ca_{2-x}Sr_xRuO_4$.

In the first part, we analyse the phonon modes observed in the low-temperature spectra of Ca_2RuO_4. Our measurements are compared with results from the literature and DFT simulations to better understand the nature of these modes. We will study the antiferromagnetic transition and identiy the Raman active excitations characteristic of the anti-ferromagnetic ordered state.
We study the lattice dynamics and electron-phonon interactions in Ca_2RuO_4, focusing on the broadening and energy shifts of selected phonon modes. These changes are linked to the structural transformation associated with the metal–insulator transition (MIT) at $T_{MI} = 357$ K [52, 66, 67]. Indeed, the MIT is determined by the elongation of the octahedra along the c-axis, but it does not occur abruptly; instead, it develops over a broad temperature range before reaching T_{MI}. Additionally, we analyze the intensity behavior of two phonon modes, which we tentativly attribute to the orbital ordering transition at approximately 260 K [68].

In the second part, we present the low-temperature spectrum of Sr_2RuO_4 and report possible evidence of a Fermi-liquid transition [45] at low temperatures.

In the third part, we discuss the low-temperature spectra of $Ca_{2-x}Sr_xRuO_4$ compounds. We attempt to identify the nature of the phonon modes by comparing them with the corresponding modes in Ca_2RuO_4 and Sr_2RuO_4.
We detect a structural phase transition in the $x = 0.2$ and $x = 0.3$ compounds. Finally, we present evidence of metallic behavior in the $x = 0.2$ sample, based on a comparison with Ca_2RuO_4.

Before discussing this section in detail, we first summarize the main phase transitions observed in our sample within the phase diagram (Figure 4.16). All subsequent measurements in this chapter were performed using the *cryostat-coupled Raman setup* (Figure 2.3) operated in single-stage mode with a 1200 grooves/mm grating. The average laser power was maintained at ~ 8 mW.

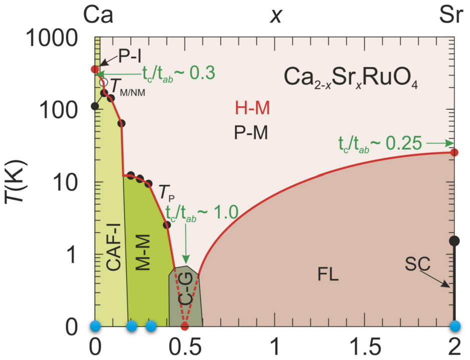

Figure 4.16: Phase diagram of Ruthenates. The x-axis is the Sr contens, while the y-axis the temperature in a logarithmic scale. Light green corresponds to the counted antiferromagnetic transition in the insulating state (CAF-I); green for the metallic-magnetic state (M-M); red for the Fermi-liquid state (FL); black for the superconducting state (SC). The red line marks the transition to an Hund-metal (H-M), while the black line the paramagnetic state (P-M). Light-blue circles indicate the samples studied in the following section. Image adapted from [60].

4.2.1 *Ca$_2$RuO$_4$*

4.2.1.1 *Anti-ferromagnetic phase*

We perform a characterization of the phonon modes of Ca$_2$RuO$_4$ in the Anti-ferromagnetic phase down to 1.8 K. The measurements are performed in both geometries A_g and B_{1g}. The results are shown in Figure 4.17, where (a) and (b) displays the B_{1g} and A_g channels, respectively.

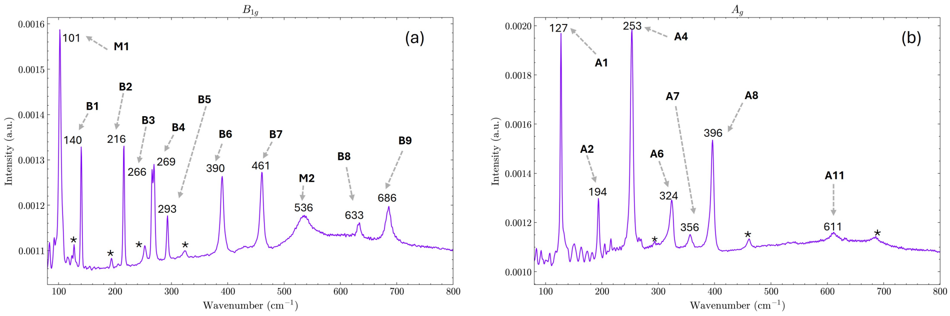

Figure 4.17: Raman Spectra of Ca$_2$RuO$_4$ at 1.8K: in (a)-(b) the B_{1g} and A_g geometry, respectively. The peaks M1 and M2 are magnetic excitations, where M1 is might attributed to a single-magnon [58] and M2 to a two-magnon scattering [58]. The 9 expected phonons are visible in the B_{1g} channel while in the A_g channel two are missing, probably at 204 cm^{-1} and 304 cm^{-1} [47]. A residual of the other polarization might be present and it is represented by the peaks marked with an asterisk.

The B_{1g} channel shows two magnetic modes: one at low energy around $\sim 100\,\mathrm{cm}^{-1}$ (M1), one at higher energy around $532\,\mathrm{cm}^{-1}$ (M2). We discuss in detail the nature of these modes in the next section (Sect. 4.2.1.2).
As reported previously in Chapter 3, nine phonon modes might be present in both configurations [47].
Relatively for the B_{1g} configuration, nine B_{1g} phonons expected are present. As found in the room temperature measurements (Figure 4.4), the mode at $461\,\mathrm{cm}^{-1}$ (B2) is might attributed to the apical oxygen vibration [64]. Since there is a lack in the literature for the B_{1g} phonons, we are unable to attribute the remaining phonons to vibrations of specific atoms. One suggestion is to perform a DFT simulation and sketch the ion displacements for the calculated phonon modes.
On the other hand, in the A_g geometry we identify seven A_g phonons (Figure 4.17b). Two A_g modes are missing; by comparison with the literature [47, 69], these modes might be at $204\,\mathrm{cm}^{-1}$ and $304\,\mathrm{cm}^{-1}$. The two missing peaks were hard to identify even in [69]. This is due probably to the presence of a broad continuum above $200\mathrm{cm}^{-1}$ and 600^{-1} that was already reported in [58] and that evolves upon entering the magnetically ordered state.
A residual of the other polarization might be present and it is represented by the peaks marked with an asterisk. This might be caused for a small misallingment of the crystals inside the cryostat, which makes the incoming light not precisely oriented at 45° with respect to the Ru-Ru bond, as shown in the ideal polarization scheme (Figure 4.1).

We summarized these results in table 4.1, in which we compare the relative peak position with the ones obtained in [47] and with the phonon energies calculated with density functional theory (DFT) in [69]. The results are in good agreement with both the DFT simulations and the reference data. The peak at $356\ \mathrm{cm}^{-1}$ (A7) is expected from the DFT calculations, but is not reported here since it was also absent in the reference study [69]. In addition, we observe a phonon mode at $633\ \mathrm{cm}^{-1}$ (B) in the B_{1g} channel, whose energy is comparable to the A_g mode A12 predicted by DFT, although we do not detect this mode in the A_g geometry. We also report a lack of evidence for A3, consistent with the findings in [69]. Finally, the predicted B mode is not observed, likely because it lies beneath the shoulder of M2.

Finally, we report the DFT simulation results [69] for the nine A_g phonons, which allow us to determine the specific atomic contributions to the corresponding vibrational modes. In particular, Figure 4.18 sketches the crystal structure and shows the corresponding A_g displacement patterns. O1 stands for the in-plane oxygen position while O2 for out-of-plane. The parameters in the polarization vectors of the A_g modes correspond to the free structural parameters of Ca, O1, and O2 positions in the orthorhombic ($Pbca$) structure.

In the modes A1, A2, A3 is possible to find the parameters describing the tilting of the octahedron [69], which are sensitive to a the second structural phase transition occuring at 650K [54]. This transition brings the system to a higher symmetry phase characterized by the suppression of the octahedra's tilt θ (Figure 3.7a).
Concerning the two highest A_g modes (A11-A12), the interpretation is that both are Ru-O bond-stretching modes: A11 corresponds to the vibration of the apical O2 in c direction and A12 is the in-plane stretching mode. These two modes can be taken as a probe of the flattening or elongation of the RuO_6 octahedra [69], therefore of the structural transition between S–phase to L–phase (Figure 3.4b).

Table 4.1: Comparison of Ca_2RuO_4 Raman peak positions at 1.8K. B_{1g} and A_g modes are related to the reference values in [47] and DFT predictions performed in [69]. S indicate short c-axis phase, characterized by more compressed octahedra (shorter Ru–O bond length along the c-axis). By contrast, L stands for long c-axis phase, where octahedra are elongated (stable at higher temperature, above ~ 360–380K) [52].[3]

Thesis 1.8K	**Maeno** [47] 10K	**DFT** [69] 10K **(S)**	**DFT** [69] 300K **(S)**	**DFT** [69] 400K **(L)**	**Label**	**Mode Nature**
B_{1g} **modes [cm^{-1}]**						
101	–	–	–	–	M1	Magnetic mode (single-magnon) [58]
140	140	133.7	131.0	119.4	B1	Not assigned
216	215	225.9	221.7	218.4	B2	Not assigned
266	265	255.8	242.7	233.4	B3	Not assigned
269	269	263.6	264.2	267.6	B4	Not assigned
293	292	287.3	281.3	286.1	B5	Not assigned
390	388	381.0	352.5	345.9	B6	Not assigned
461	459	461.5	397.5	419.2	B7	Apical oxygen vibration (O2) [64]
–	–	514.3	482.4	481.0	–	Not assigned
536	534	–	–	–	M2	Magnetic mode (two-magnon) [58]
633	–	–	–	–	B8	Not assigned
686	683	662.5	659.1	655.0	B9	Not assigned
A_g **modes [cm^{-1}]**						
127	126	124.2	118.0	95.2	A1	Octahedral tilting
194	192	185.2	174.5	176.1	A2	Octahedral tilting
–	204	206.0	198.2	204.7	A3	Octahedral tilting
253	251	256.5	250.8	227.9	A4	Not assigned
–	304	302.9	276.6	271.5	A5	Not assigned
324	322	329.3	311.9	320.5	A6	Not assigned
356	356	–	–	–	A7	Not observed in [69])
396	395	404.5	407.6	391.9	A8	Not assigned
611	607	600.3	569.7	552.8	A11	Apical oxygen (O2) stretching along c
–	–	627.9	640.7	666.6	A12	In-plane Ru–O1 stretching

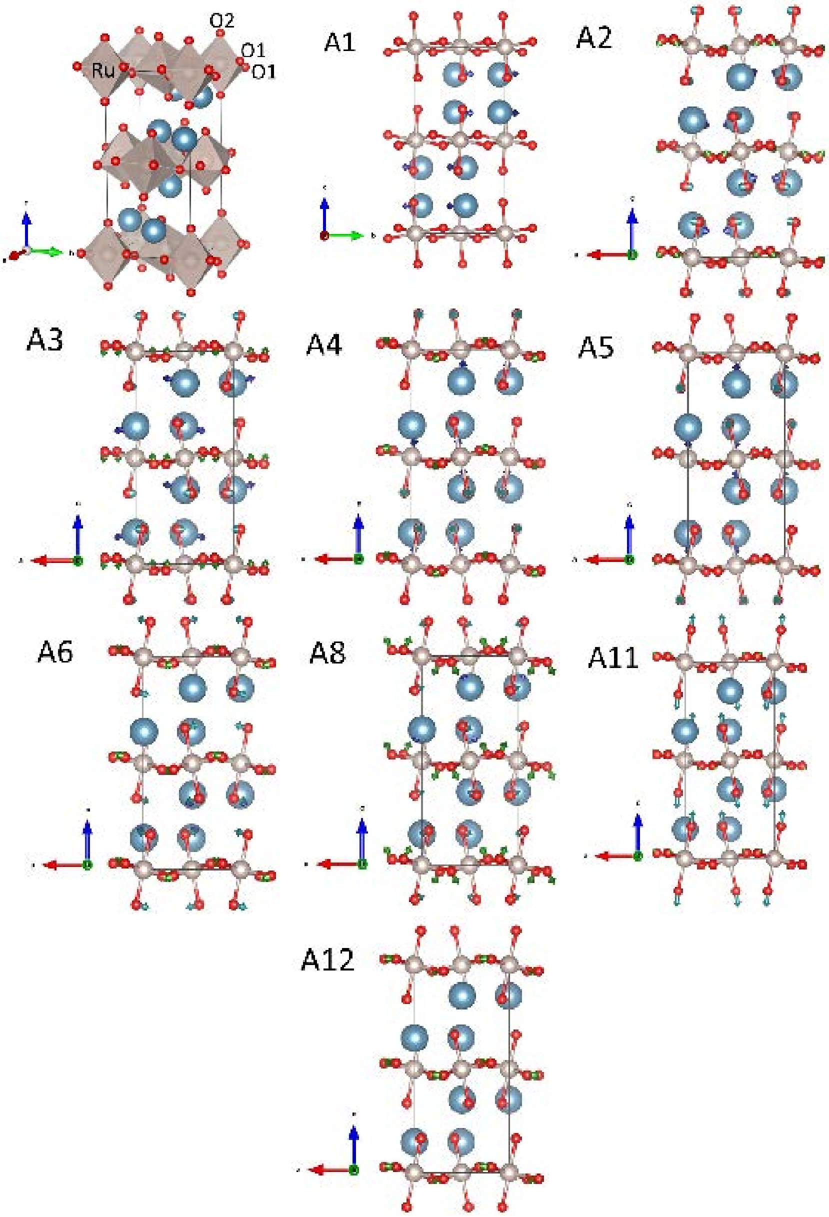

Figure 4.18: Sketch of the Ca_2RuO_4 crystal structure and the ion displacements for the 9 calculated Ag phonon modes A1-A6, A8, A11, A12 [69]. The parameters in the polarization vectors of the A_g modes correspond to the free structural parameters of Ca, O1, and O2 positions in the orthorhombic ($Pbca$) structure. Temperature is not mentioned in [69].

4.2.1.2 *Raman scattering across the antiferromagnetic transition*

In order to understand and characterize how these vibrational and magnetic excitations evolve across the antiferromagnetic transition, we performed a temperature scan from 1.8 K to 290 K. The results are summarized in Figure 4.19, where panels (a) and (b) show all the Raman spectra collected in the B_{1g} and A_g geometries, respectively. Both channels exhibit common features with increasing temperature, such as (i) mode broadening, (ii) quenching of specific modes, and (iii) significant modifications of the background in proximity to the antiferromagnetic transition.[4]

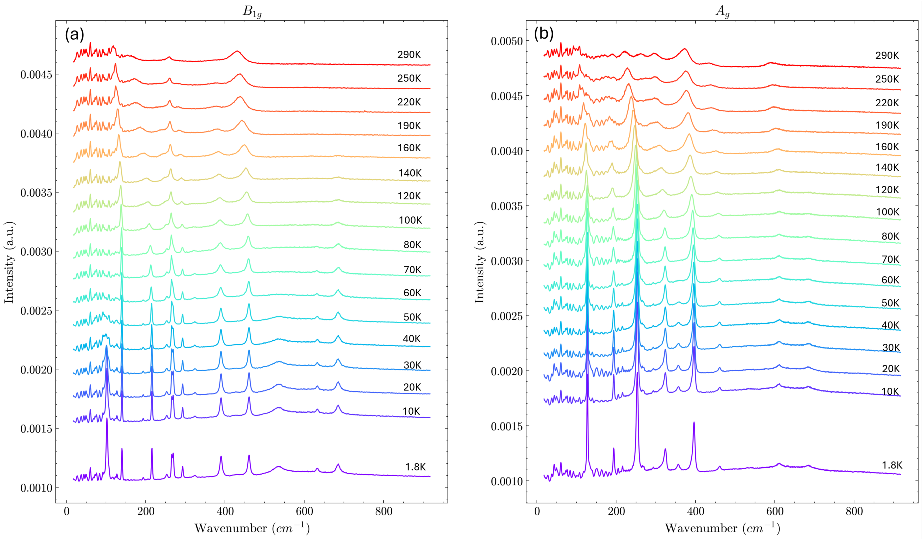

Figure 4.19: Temperature dependent Raman scattering of Ca_2RuO_4 across the AF transition: Raman spectra collected from 1.8 K to 290 K in B_{1g} (a) and A_g (b) geometry. The spectrum are shifted for clarity. The power used for these measurements is ~ 1 mW.

Regarding (iii), we decide to perform the next analysis, following the similar approach in [58].
Concerning the B_{1g} channel, in Figure 4.20 we present two zooms over the regions 90–180 cm^{-1} (B) and 480–800 cm^{-1} (B′), where in particular panel (a) shows the temperature scan reported in Figure 4.19 with the two regions of interest highlighted in shaded gray, while panels (b-c) represent the Raman spectra over the B and B′ regions for some selected temperatures.

The feature B appears around 102 cm^{-1} and gradually sharpens.[5] Its nature, however, remains under debate. Previous studies have attributed M1 either to two-magnon scattering [64, 70], to a zone-boundary folded phonon[6] in the

---

[4] To disentangle background changes from preprocessing artifacts (Figure A.1), the Raman spectra presented here are normalized without applying the asymmetric least squares method (see appendix B).

[5] The labels are consistent with [58], although this feature was previously attributed to M1 (see Figure 4.17).

[6] A zone-boundary folded phonon is a vibrational mode that originally exists at the edge of the Brillouin zone but becomes observable at the center due to a change in the crystal's periodicity—often caused by magnetic or structural ordering that doubles the unit cell [71].

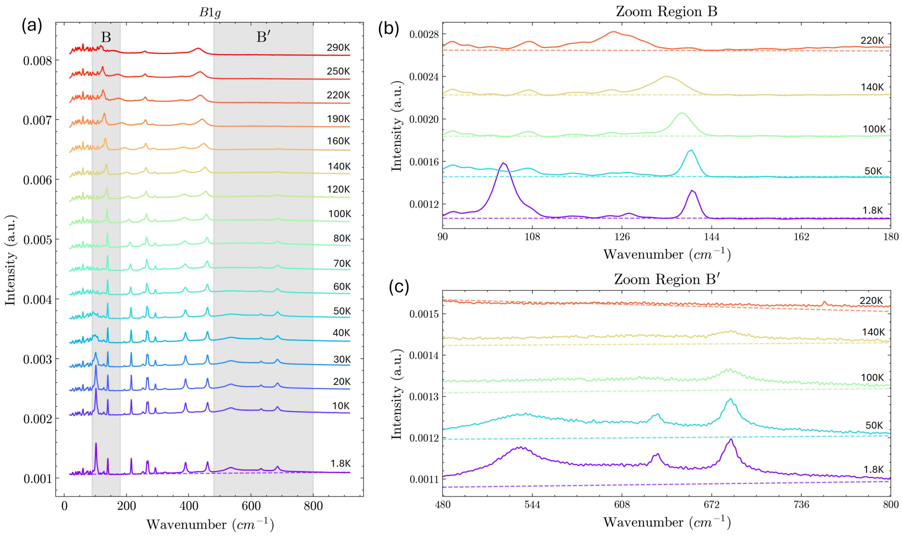

Figure 4.20: Raman spectra of Ca_2RuO_4 in B_{1g} scattering geometry with two magnetic features B, B′ appearing below T_N. In (a) is shown the temperature scan with the two regions highlighted in grey. In (b)-(c) are reported the Raman spectra over B, B′ for some selected temperatures. The background (dashed line) is subtracted in further analysis. The B region is related to a single-magnon excitation, while the B′ region to a two-magnon feature [58], as evidenced by the broad continuum present only in the latter.

magnetically ordered state [47], or to a single-magnon excitation [58]. Our measurements under an external magnetic field might point to its two-magnon nature (see Chapter 5).
The B′ region shows a strong decrease with temperature of the peak at 536 cm^{-1}. This peak is associated with a two-magnon feature [58]. The two-magnon feature is also verified looking how the continuum background[7] in the B′ region changes increasing the temperature. Indeed, a two-magnon scattering involves creating two magnons simultaneously with opposite momenta. Each individual magnon can occupy a wide range of the Brillouin zone and therefore many different k-values contribute (see Figure 1.8), which gives as a result a broad continuum of possible energies rather than a sharp line as for single magnon excitation [72].

Regarding the A_g channel, we present in Figure 4.21 two zooms over the regions 150–430 cm^{-1} (A) and 550–850 cm^{-1} (A′) of the A_g spectra. As previously for the B_{1g} channel, panel (a) shows the temperature scan reported in Figure 4.19 with the two regions of interest highlighted, while panels (b-c) represent the Raman spectra over the A and A′ regions.

---

[7] The background is fitted considering it linear.

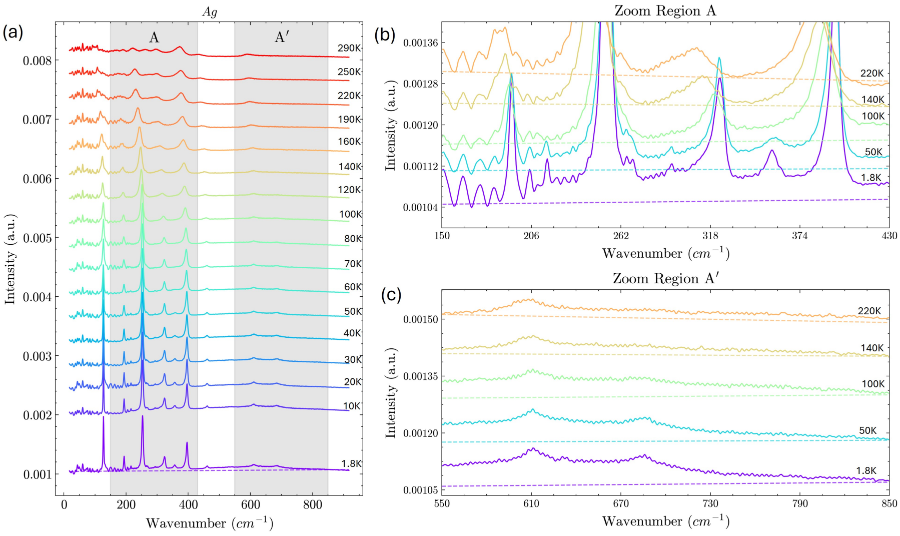

Figure 4.21: Raman spectra of Ca_2RuO_4 in A_g scattering geometry with two magnetic features A, A′ appearing below T_N. In (a) is shown the temperature scan with the two regions highlighted in grey. In (b)-(c) are reported the Raman spectra over A, A′ for some selected temperatures. The A region might be related with the presence of a Higgs-mode peaked at $322\,\text{cm}^{-1}$. A continuum of excitations caused by a two-magnon scattering is visible from the Fano-type of the peak at $322\,\text{cm}^{-1}$ and from the broad continuum that extends in the A′ region, as evidenced by the change of the background.

It is notably the decrease of the background raising the temperature in both regions. Again, this continuum is experimentally and theoretically associated with a two-magnon scattering [58]. The presence of a continuum of excitation can be seen looking at the shape of the peak at 324 cm^{-1} (A6). It has a simmetric shape at higher temperature, while at low temperature it exhibits pronounced Fano-type asymmetric line shapes. The presence of an asymmetric line-shape is a clear signature of the presence of a continuum of excitations coupled to the phonons [73]. Moreover, in [58] they extract the magnetic response of the coupled system of phonons and a continuum and they found that the magnetic feauture in A is peaked at about 322 cm^{-1} (further details will be given in Chapter 5) and has a long tail that merges with the high-energy continuum (A′), much flatter than the B_{1g} one (B′).
Still considering the region A and A′, there are two peaks emerging at low temperature: 356 cm^{-1} and 686 cm^{-1}. The first is a phonon mode in the A_g channel (A7), the second a residual of the polarization of the B_{1g} mode (B9).

In order to show clearly the temperature dependence of these magnetic features, for each temperature we calculate the integrated intensity[8] of the regions B-B′, which corresponds with M1 and M2 (Figure 4.17), and A-A′. Respectively, these results are shown in Figure 4.22(a)-(b) and in Figure 4.22(c)-(d).

The intensity of the regions M2-A-A′ starts to increase close to the antiferromagnetic transition at 110 K [49]. This behavior is not found for the M1 region, where the intensity changes abruptly close to ~ 60 K. A reasonable explanation why this temperature appears lower than 110 K could be a local heating coming from the laser beam, although the absence of the broad magnetic continuum might contribute.

To further investigate this point, we compare the integrated intensities of the M1 and M2 regions with and without background subtraction. In the former case ("with background") we use the same approach as before, i.e., we subtract only a linear baseline. In the latter case ("without background") we apply the full background-removal procedure described in appendix B (Figure A.1). The results are shown in Figure 4.23.

The M2 region exhibits the same trend as M1 when the background is removed. This points to the crucial role of the underlying magnetic continuum and indicates that it persists to temperatures above the measured antiferromagnetic transition (60 K).

---

[8] The area is determined by subtracting the background, which is obtained with a linear fitting. After that, the area is normalized by its value at 1.8 K.

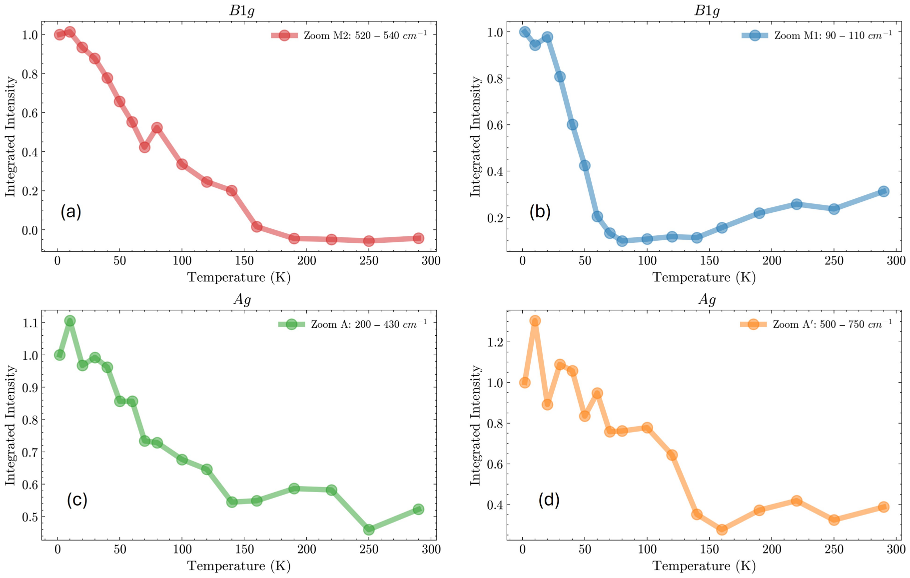

Figure 4.22: Integrated intensity temperature-dependence of magnetic regions in Ca_2RuO_4: in (a)-(b) are shown the two magnons M1 and M2 for B_{1g} geometry (Figure 4.17a), which corresponds with B and B′ regions in Figure 4.20, while in (c)-(d) the regions A and A′ in Figure 4.21 for A_g geometry. The area values are normalized with the value at 1.8 K for each region. All of the areas share a significant increase of its intensity for $T < T_N = 110\,K$. In particular, the feature in (b) has a lower temperature, which might be attributed either to the absence of the broad continuum either to a local heating from the laser.

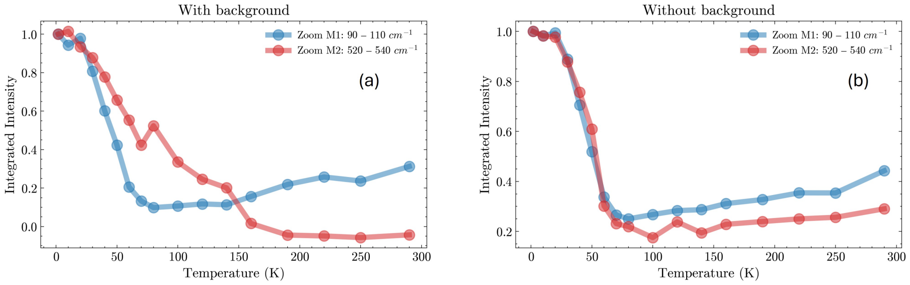

Figure 4.23: Effect of magnetic background on the B_{1g} magnon regions in Ca_2RuO_4. Integrated areas of M1 (blue) and M2 (red) obtained (a) with a linear baseline (“with background”) and (b) after full background removal (described in appendix B). The similar trend of M2 when the background is removed indicates that the underlying magnetic continuum persists at higher temperature than the measured antiferromagnetic transition (60 K).

4.2.1.3 *Lattice Dynamics and Electron-Phonon Interaction*

The second aspect we want to explore in the temperature scan presented previously (Figure 4.19) is the lattice dynamics and the electron-phonon interaction as a function of temperature below the metal-insulator transition temperature $T_{MI} = 357\,K$ [52]-[66]-[67].

We start from Figure 4.24(a), which displays the phonon energy changes with increasing temperature for some representative B_{1g} (140, 220, 380, 460 cm^{-1}) and A_g (125 and 605 cm^{-1}) optical phonon modes[9]. The results agree well with the literature [47] (Fig. 4.24b). The phonon-energy shifts are significantly higher for $T_N < T < T_{MI}$, while there is a little change for $T < T_N$. These systematic shifts of the phonon peak to lower energies when temperature increases through T_N is mainly due to the elongation of the RuO_6 along the c axis [47], as confirmed by considering the temperature-dependence of the c lattice parameter (Figure 3.4).

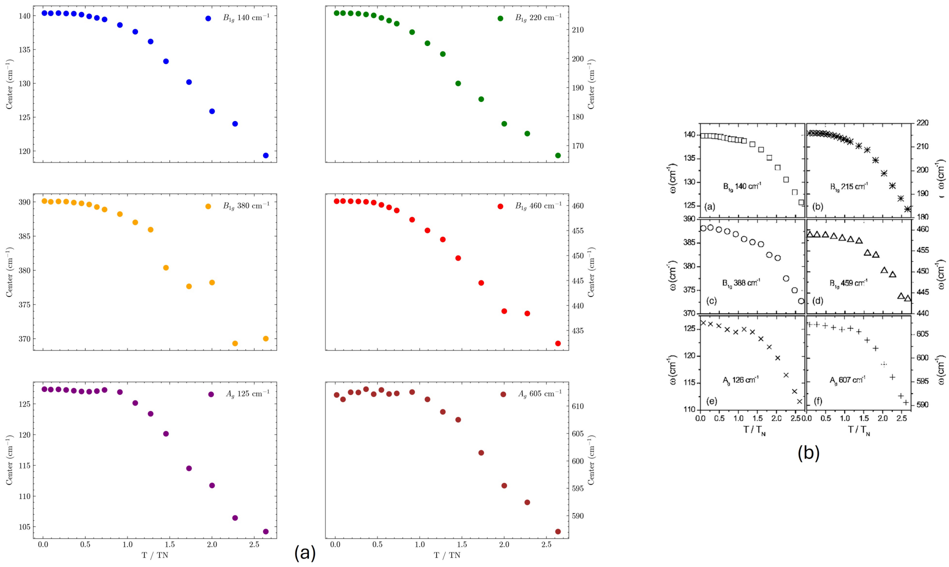

Figure 4.24: Temperature-dependent frequency shifts of Ca_2RuO_4 phonons: (a) shows the B_{1g} modes at 140, 220, 380, 460 cm^{-1}, and of A_g modes at 125 and 605 cm^{-1}. The temperature T is normalized with $T_N = 110\,K$. (b) displays a similar result reported in [47]. It is noticeable that the phonon energy decreases as the temperature increases above T_N. The systematic shifts of the phonon peak to lower energies when temperature increases through T_N is mainly due to the elongation of the RuO_6 along the c axis [47].

---

[9] We do not use the labels in order to make the same comparison with the literature. In particular, B_{1g} phonons (140, 220, 380, 460 cm^{-1}) correspond with B1, B2, B6, B7; while A_g phonons (125 and 605 cm^{-1}) are A1, A11.

Most of the modes exhibit a shift of $\sim 20\,\mathrm{cm}^{-1}$ to lower energies as the temperature increases from 1.8 K to 290 K. The energy of the A_g modes decreases closer to T_N than that of the B_{1g} modes. The fact that the shift starts at higher temperature in the A_g channel for 125–605 cm^{-1} is likely related to the nature of these modes. Specifically, they correspond to the vibration of Ca in the plane and the apical oxygen along the c axis, as shown in the displacement patterns from the DFT simulation (A1 and A11 in Figure 4.18). Consequently, they are more strongly affected by the elongation of the RuO_6 octahedra along the c axis, which occurs with increasing temperature during the transition from the S-phase to the L-phase at $\sim$ 360,K [52] (Chapter 3).

Another feature is that the B_{1g} phonon at $220\,\mathrm{cm}^{-1}$ shows a dramatic energy shift of $\sim 50\,\mathrm{cm}^{-1}$. This anomalous behavior was already reported in [47], although our result is even higher of $\sim 20\,\mathrm{cm}^{-1}$ from what they found (Figure 4.24b). Unfortunately, we have no indications related to the nature of this mode, therefore it is difficult to comprehend better this result.

Increasing the temperature, the phonon linewidths broaden significantly (Figure 4.19). This could be affected by (i) the interaction between the discrete phonon state and a broad electronic continuum of states and by (ii) the phonon-phonon interaction. In [47], they suggest that the dramatic linewidth changes in Ca_2RuO_4 with increasing temperature primarily reflect changes in the electron-phonon interaction, rather than the phonon-phonon interaction.
To study the electron-phonon interaction in detail, the temperature dependence of the phonon linewidths of the B_{1g} and A_g phonon modes were extracted by fitting these modes to a Fano line shape,

$$I(\omega) = I_0 \cdot \frac{(q+\epsilon)^2}{1+\epsilon^2} \tag{4.1}$$

where $\epsilon = (\omega - \omega_0)/\Gamma$, ω_0 is the photon energy, Γ is the effective phonon linewidth, and q is the asymmetry parameter. From the fractional change in the phonon damping rate below T_{MI}, calculated as $\Delta\Gamma/\omega_0 = [\Gamma(T) - \Gamma(290\,K)]/\omega_0$, it is possible to estimate the electron-phonon coupling.[10]

In Figure 4.25(a) is plotted the $\Delta\Gamma/\omega_0$ as a function of temperature. It shares common features with the previous results for the shifts of the phonon energies in Figure 4.24: the phonon linewidth has a significant change only above T_N and the B_{1g} phonon at $220\,\mathrm{cm}^{-1}$ has an anomalous behavior. In fact, it has $\Delta\Gamma/\omega_0 \sim 6.6\%$, while the other modes have $\Delta\Gamma/\omega_0 \sim 1.2-3.8\%$. These results agree well with the literature results presented in Figure 4.25(b) [47].

---

[10] $\Delta\Gamma/\omega_0$ is proportional to the dimensionless electron-phonon coupling parameter λ [74]-[75], which is related to the BCS parameter $N(0)V_{ph}$, where V_{ph} is the pairing potential arising from the electron-phonon interaction and N_0 the electronic density of states at the Fermi surface [76]-[77].

The observed increase of $\Delta\Gamma/\omega_0$ above T_N, which is related to the electron-phonon interaction and number of carriers, strongly suggests that enhanced orbital fluctuations, which are associated with the increased electron transfer between d_{xy} and $d_{yz/zx}$ orbitals, are responsible for the behavior observed in this temperature regime [47]. A detailed analysis of this feature is presented in the following (Section 4.2.1.4).

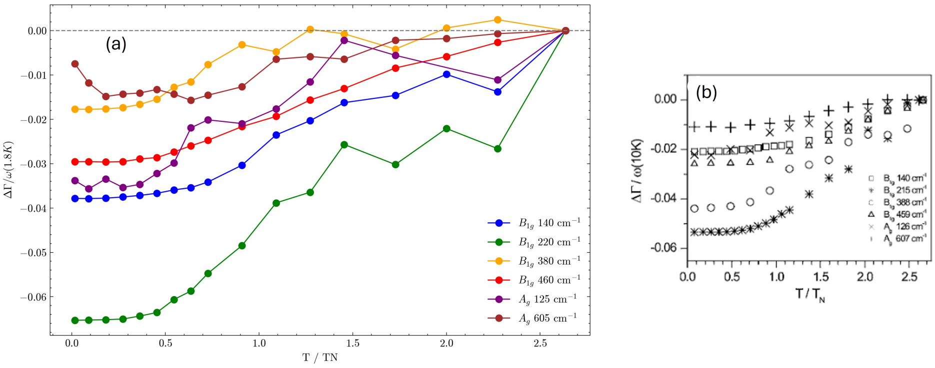

Figure 4.25: Phonon linewidth changes in Ca_2RuO_4 as a function of temperature normalized to T_N. The phonon linewidth changes ($\Delta\Gamma = \Gamma(T) - \Gamma(290\,K)$) are divided by the corresponding phonon energy at T=1.8 K. The plot (a) shows the results obtained after fitting with a Fano profile the spectra in Figure 4.19. The results are in good agreement with the literature in (b) [47]. It can be observed that the linewidth increases significantly above T_N and the B_{1g} peak at 220 cm^{-1} exhibits an anomalous behavior compared with the others modes.

4.2.1.4 *Possible Evidence for an Orbital-Ordering Transition*

A further notable feature in the temperature-dependent Raman spectra (Figure 4.19a) regards the intensity ratio between the two B_{1g} peaks, B6 (390 cm^{-1}) and B7 (461 cm^{-1}) (Figure 4.26).

Figure 4.26(a) zooms into the 350–500 cm^{-1} window of the temperature scan. At low temperature the two peaks have comparable intensities. Upon heating, however, B6 progressively weakens and eventually vanishes, while B7 remains visible.

Figure 4.26(b) plots the B6/B7 intensity ratio as a function of temperature; the inset shows the individual peak intensities. Notably, B6 disappears around $T \sim 260$ K. This behavior is consistent with the onset of an orbital-ordering transition. Indeed, O 1s x-ray absorption on $Ca_{2-x}Sr_xRuO_4$ ($x = 0, 0.09$) indicates that orbital fluctuations increase with temperature well within the insulating phase (i.e., at $T \ll T_{MI}$) and culminate in an orbital-ordering transition near $T_{OO} \sim 260$ K [68, 78].

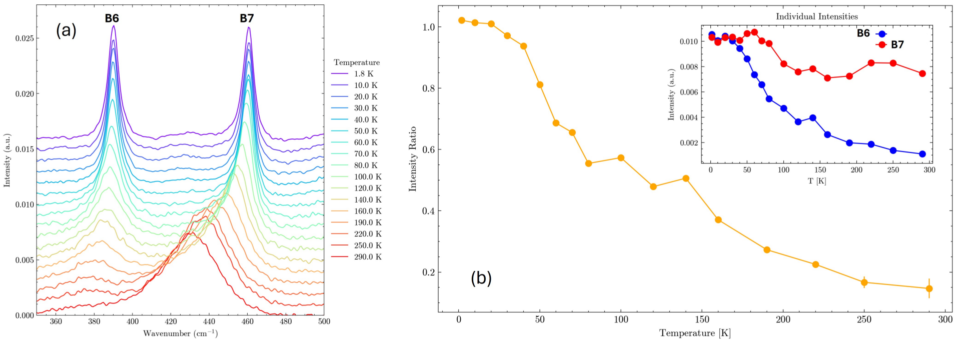

Figure 4.26: Intensity comparison for the B_{1g} phonons at 390 and 461 cm^{-1} in Ca_2RuO_4. (a) Temperature dependence of the B_{1g} spectra in the 350–500 cm^{-1} window, extracted from Figure 4.19. (b) B6/B7 integrated-intensity ratio versus temperature; the inset shows the individual peak intensities. The 390 cm^{-1} mode (B6) vanishes near $T \sim 260$ K, close to the proposed orbital-ordering transition [68].

The orbital-ordering transition is sketched in Figure 4.27. The $4d^4$ electrons of Ru occupy the t_{2g} manifold (see Chapter 3 for details). Crystal-field effects and octahedral distortions polarize the t_{2g} levels. In particular, elongation of the RuO_6 octahedron along the c axis raises the energy of d_{xy} relative to the nearly degenerate $d_{xz/yz}$ doublet [55]. Consequently, in the S phase with a short c axis ($T < T_{MI} = 357$ K) d_{xy} is energetically favored, whereas in the L phase ($T > T_{MI}$) the order is reversed [53].

We tentatively consider the orbital-ordering transition as follows. Since the strong structural changes between the low-temperature S and high-temperature L phases are not restricted to the metal–insulator transition but occur over a wide temperature range between T_{MI} and the antiferromagnetic ordering temperature $T_N = 110, K$ [50]-[51]-[52], the elongation of the octahedra upon warming from low temperatures to T_{OO} decreases the splitting between d_{xy} and the d_{xz}/d_{yz} doublet [55], and therefore interorbital fluctuations are enhanced because electrons require less energy to *hop* between d_{xy} and d_{xz}/d_{yz}. We present these considerations schematically in Figure 4.27. However, we point that the proposed picture fails whenever the fluctuations are involing the d_{xz}/d_{yz} doublet, as the relative orbital energy between them might not be affected significantly during this process.

Such changes in orbital occupation and fluctuations might modify the electron–phonon coupling, broadening linewidth and potentially suppressing specific phonon intensities. It is therefore plausible that B6 is more strongly affected by orbital fluctuations than B7, accounting for its rapid loss of intensity on approaching T_{OO} (see also the linewidth analysis in Figure 4.25).

Finally, the B6/B7 intensity ratio can serve as an internal thermometer to estimate local laser heating during Raman acquisition, enabling *in situ* correction of power-induced temperature offsets.

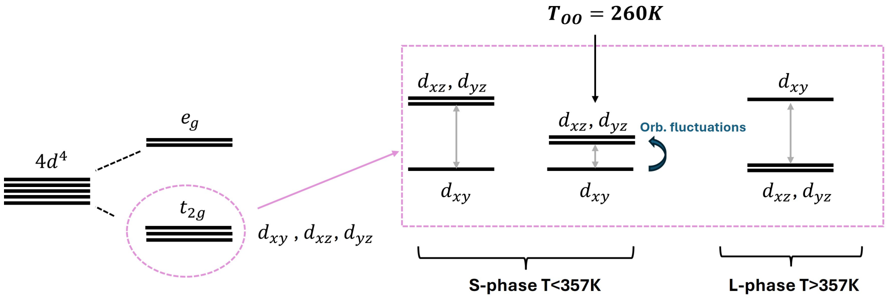

Figure 4.27: Proposed orbital-ordering scenario in Ca_2RuO_4. Schematic t_{2g}-level polarization of Ru^{4+} ($4d^4$) as a function of octahedral distortion along the c axis. In the S phase ($T < T_{MI} = 357$ K; short c axis), d_{xy} lies lowest and is preferentially occupied; in the L phase ($T > T_{MI}$), elongation along c raises d_{xy} relative to the nearly degenerate $d_{xz/yz}$ doublet [55]. Approaching $T_{OO} \sim 260$ K from below, the d_{xz}–d_{yz} splitting diminishes. Therefore, orbital fluctuations might grow since the electrons require less energy to *hop* into d_{xz} and d_{yz}. This feature might modify the electron–phonon coupling and suppress the B_{1g} phonon intensity of B6 relative to B7 (see Figure 4.26).

4.2.2 *Sr_2RuO_4*

4.2.2.1 *Low Temperature*

We report a characterization of the phonon modes of Sr_2RuO_4 down to 1.8 K in the A_g channel (Figure 4.28). The power used is $\sim$ 1 mW.

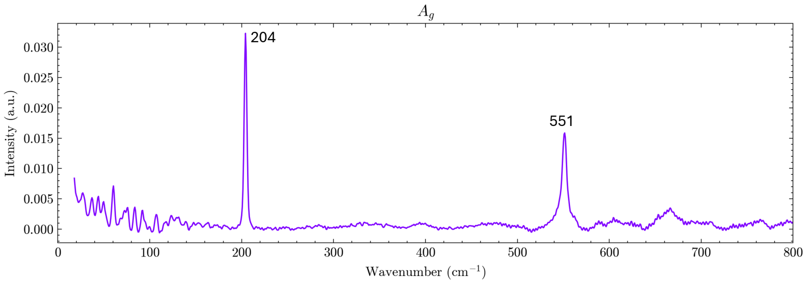

Figure 4.28: Raman spectrum of Sr_2RuO_4 at 1.8 K in A_g geometry. Two A_g phonon modes are visible. The one at 204 cm^{-1} corresponds with the in-phase motion between Sr and apical oxygen (O2), and the other at 551 cm^{-1} with the vibration of apical oxygen (O2) along the c axis [63]. The small intense peaks at low energy in the range 0–100 cm^{-1} are associated with the vibrational modes of air.

We clearly observed two A_g modes, which are expected by the tetragonal structure (Chapter 3). In particular, the two modes are centered at 204 and 551 cm^{-1}. Their phonon energies agree well with the literature [63] and with the room-temperature spectra reported previously when we studied their polarization dependence (Figure 4.2a).

The mode at 204 cm^{-1} corresponds to the in-phase motion between Sr and apical oxygen (O2), and the one at 551 cm^{-1} to the vibration of apical oxygen (O2) along the c axis [63].
No phonons were visible in the B_{1g} configuration, and the results are similar to those already reported at room temperature (Figure 4.2b). Therefore, we have not reported in the following.

4.2.2.2 *Possible Evidence of Fermi liquid properties*

We perform a temperature scan from 1.8 K to 300 K. Regarding the temperature-dependence of the two A_g modes, there is a blue shift of the phonon energies and a broadening with increasing temperature for the two observed phonons. This feature is likely due to an increase in lattice temperature and is not particularly related to any structural transition, as we observe in Ca_2RuO_4.
However, we observe a notable behavior in the energy range 15–150 cm^{-1} for the selected temperatures (Figure 4.29a). In this Raman spectra, the background decreases monotonically until 150 cm^{-1} for $T < 50$ K, while it presents

a different shape above 100 K: after a small increase up to 50 cm^{-1}, it decreases monotonically over the entire spectral region. A broader peak may be present around 40–60 cm^{-1}.

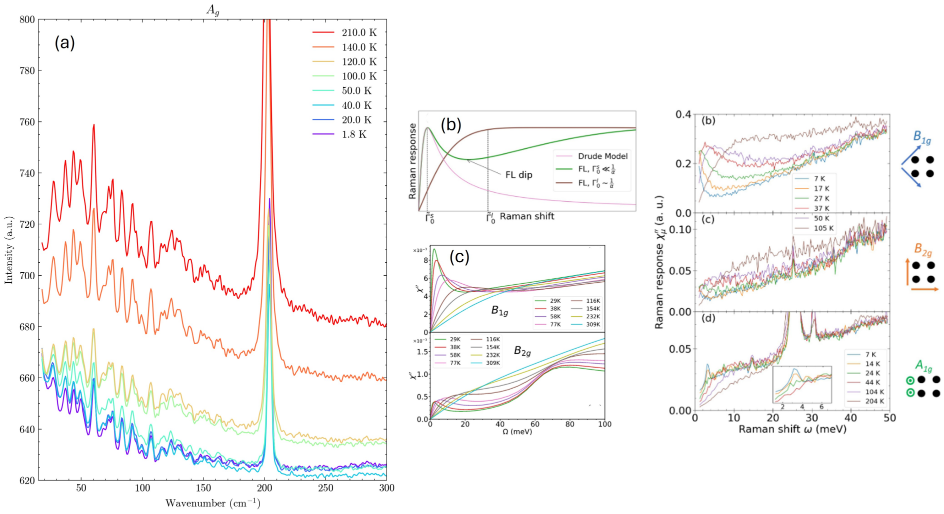

Figure 4.29: Focus on the Fermi-liquid transition in Sr_2RuO_4. (a) Raman spectra obtained for selected temperatures over the spectral region 10–300 cm^{-1}. A change in the low-energy region is observed, which might be related to the theoretical models of the Raman response of a Fermi liquid in (b) [79] and of Sr_2RuO_4 in the B_{1g} and B_{2g} channels in (c) [80]. (d)–(e)–(f) show the Raman measurements reported in [79], which demonstrate the dependence of Fermi-liquid properties on the polarization geometry.

Figure 4.29(b) shows the Raman response for the Drude model and Fermi-liquid model [79], and Figure 4.29(c) shows the Raman response of Sr_2RuO_4 for the B_{1g} and B_{2g} channels with the model discussed in [80]. The main difference in the Raman response between the Drude model and the Fermi-liquid model[11] is the nonmonotonic line shape of the response beyond the Drude peak, leading to a characteristic FL "dip" in the Raman spectra that separates the Drude regime at lower energy from the thermal regime at higher energy [79]. This might explain the different behavior in our measurements above and below 100 K.

Moreover, we compare our measurements with those in the literature in Figure 4.29(d–f). The B_{1g} channel shows a similar behavior in the low-energy region (Figure 4.29d), but in our measurements the electronic background always decreases with increasing energy.

It is important to note that our measurements are in A_g geometry and not in B_{1g}. However, although the polarization of the incident light is not oriented at

---

[11] For a Fermi liquid with an energy-dependent quasi-particle scattering rate $\Gamma(\omega)$, the electronic Raman response is modeled by the extended Drude model [79].

45° along the Ru–Ru bonds as we mounted the sample with a random orientation, our measurements still probe the in-plane polarization. For instance, it is not along the c axis as depicted in the A_{1g} in Figure 4.29(f).
It is therefore reasonable that our results resemble the B_{1g} channel more closely than the A_{1g}. We are in a configuration similar to that in Figure 4.1, without a clear orientation along the Ru atoms.
Since our Raman spectra are performed in the parallel configuration, we collect more scattered light. This might explain why the background looks quite different from what theory [80] and previous experiments found [79].

A more detailed analysis is shown in Figure 4.30, where we normalized the background at low energy with the peak at ~55 cm^{-1} and plotted the difference between the Raman spectra at each temperature and the one at 1.8 K. This result confirms and clearly shows the temperature dependence of the low-energy landscape.

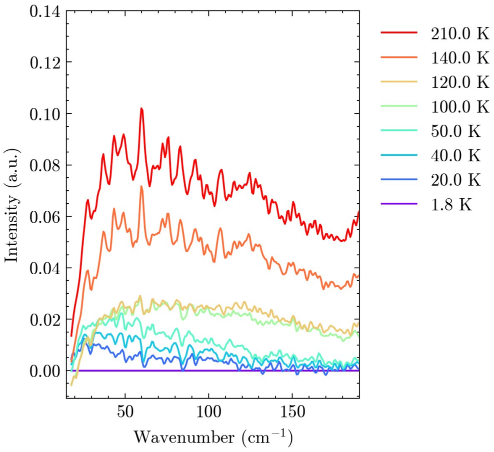

Figure 4.30: Temperature dependence of the low-energy background of Sr_2RuO_4. It displays the difference between the background of the Raman spectra in Figure 4.29(a) and the one at 1.8 K. The spectra are normalized by the peak intensity at ~55 cm^{-1}.

4.2.3 $Ca_{2-x}Sr_xRuO_4$

4.2.3.1 *Low Temperature*

We perform Raman measurements of $Ca_{2-x}Sr_xRuO_4$ samples with $x = 0.3$, 0.2 at 1.8 K. In this part we try to attribute the nature of the phonons present at low temperature by comparing the Raman spectra with the ones of Ca_2RuO_4 and Sr_2RuO_4. The results are summarized in Figure 4.31(a), which it displays from top to bottom the A_g channel for Ca_2RuO_4 ($x = 0$), doped samples with $x = 0.2$, 0.3 and Sr_2RuO_4 ($x = 2$), respectively.

Both doped samples present four distinctive peaks, which we summarize and label in table 4.2.

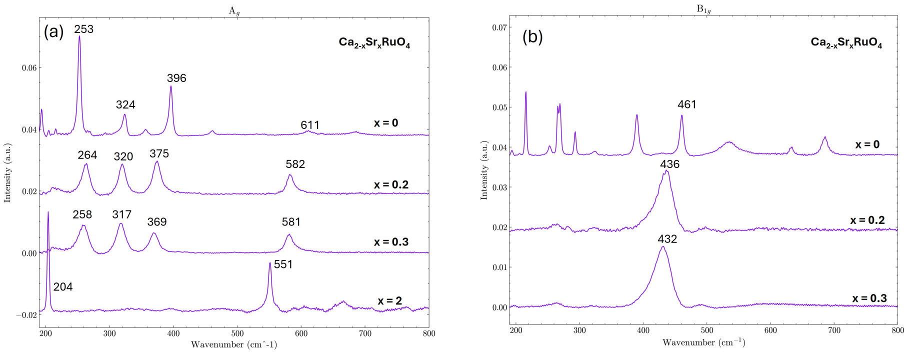

Figure 4.31: Raman spectra of $Ca_{2-x}Sr_xRuO_4$ with $x = 0, 0.2, 0.3, 2$ at 1.8 K: in (a) and (b) are shown the A_g and B_{1g} channels, respectively. For the doped sample with $x = 0.2$ and $x = 0.3$ four A_g phonons are present, which we tentatively attributed their nature to the A4, A6, A8, A11 phonons of Ca_2RuO_4 discussed previously (Figure 4.18). It is interesting how the energy of the two symmetric modes in $x = 2$ change with the doping. In the B_{1g} channel, only one phonon is present for the doped samples, which might be related with the vibration of the apical oxygen [64] or compared to the peak at 461 cm^{-1} of Ca_2RuO_4. It is not shown the B_{1g} channel of $x = 2$ because there was no excitation and differences from the room temperature spectrum already reported in Figure 4.2.

Table 4.2: Phonon modes of $Ca_{2-x}Sr_xRuO_4$ at low temperature for $x = 0.3$, $x = 0.2$, and $x = 0$. Each set of peaks is labeled according to the notation introduced in the text. The nature of these modes is discussed by comparing it with A4, A6, A8, and A11 in the DFT simulation of Ca_2RuO_4 ($x = 0$) (Figure 4.18).

Mode label	$x = 0.3$ (T)	$x = 0.2$ (S)	$x = 0$ (A)
T1 / S1 / A4	258 cm^{-1}	264 cm^{-1}	253 cm^{-1}
T2 / S2 / A6	317 cm^{-1}	320 cm^{-1}	324 cm^{-1}
T3 / S3 / A8	369 cm^{-1}	375 cm^{-1}	396 cm^{-1}
T4 / S4 / A11	581 cm^{-1}	582 cm^{-1}	611 cm^{-1}

In order to identify the nature of these modes, we decide to compare them to the low temperature spectrum of Ca_2RuO_4 ($x = 0$). In particular, it seems reasonable to associate these modes respectively with the ones at 253, 324, 396 and 611 cm^{-1} of $x = 0$ (Ca_2RuO_4), previously identified in the DFT simulation as A4, A6, A8, A11 modes (Figure 4.18). For instance, T1 (S1) is related with the vibration of the Ca atoms along the c-axis, T2 (S2) with the vibrations of the apical oxygen (O2) and the in-plane oxygen (O1) in plane, T3 (S3) with the vibration of O1 out of plane and O2 in plane, T4 (S4) with the vibration of O2 along the c-axis.

The peak at higher energy T4 (S4) looks more asymmetric in the doped samples compared to the one in Ca_2RuO_4 (A11), while is the opposite scenario for the second peaks at ~$320\,cm^{-1}$ (T2 and S2), which is asymmetric only in Ca_2RuO_4 (A6). The asymmetry is related to the Fano effect, but with two different source of couplings. Indeed, while the origin of the asymmetry in Ca_2RuO_4 (A6) is associated to the coupling between the phonon and the continuum of magnetic excitations, here in the doped samples there is no magnetic order (see phase diagram in Figure 4.16) and the system is metallic. Therefore, the asymmetry in T4 (S4) might be explained by the coupling between the phonon and the electronic continuum. Moreover, the coupling with the electronic continuum can explain why the phonon peaks are broader in the $x = 0.2, 0.3$ samples, since the electrons scattered more with the lattice giving to a less sharp phonon mode.

It is notably how the energy of the two modes in $x = 2$ changes with the increase of the doping. As discussed in the previous section of Sr_2RuO_4 at low temperature, these modes are associated to the apical oxygen vibrations [63]. For instance, it is reasonable that these are the most affected by the distortion and tilting of the octahedra (see the structural diagram with doping in Figure 3.7), which shift the energy of these modes from Sr_2RuO_4 to Ca_2RuO_4 ($204 \rightarrow 253\,cm^{-1}$ and $551 \rightarrow 611\,cm^{-1}$). Until now, it is not clear how this feature is consistent with a blue-shift (shift to higher energy) respect with a red-shift.

Finally, we present the B_{1g} channel. Figure 4.31(b) shows the B_{1g} phonons. In this geometry, the samples with $x = 0.2$ (0.3) exhibit only one peak at 432 (436) cm^{-1}. This mode is consistent with the literature [64]. By comparison with similar modes in ruthenates and cuprates, it has been suggested [47] that this mode corresponds to vibrations of the apical oxygen. Alternatively, it may be related to the B_{1g} peak at $461\,cm^{-1}$ observed in Ca_2RuO_4.

The striking difference in the number of B_{1g} modes between the doped samples ($x = 0.2$, 0.3) and the parent compound ($x = 0$) clearly indicates that octahedral distortions lift the degeneracy of the phonon modes. In particular, considering the structural–magnetic phase diagram (Figure 3.7), this difference is mainly attributed to the octahedral tilting angle θ, rather than to the in-plane rotation ϕ.

The B_{1g} channel of $x = 2$ is not shown because no phonon excitations were observed, consistent with the room-temperature spectrum already reported (Figure 4.2).

4.2.3.2 *Structural Phase Transition*

We perform a temperature-scan for the doped samples from 1.8 K to 300 K. The A_g channel results are displayed in Figure 4.32, together with the previous Raman spectra of Ca_2RuO_4.

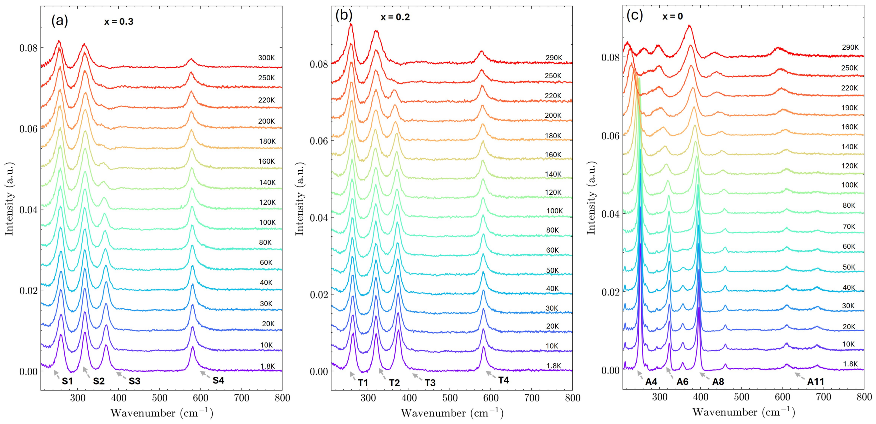

Figure 4.32: Temperature-scan of $Ca_{2x}Sr_xRuO_4$ with $x = 0.3, 0.2, 0$ in A_g channel. The doped sample are presented in (a)-(b), while Ca_2RuO_4 in (c). The Raman measurements are plotted over the spectral region 210–800 cm^{-1}. It can be observed the broadening and quenching of the mode S3 and T3 at 369 and 375 cm^{-1}. The corresponding mode A8 in $x = 0$ shares similar behavior but does not disappear.

All the phonons tend to be broader with increasing temperature. This effect is attributed to the increase of electron-phonon interaction rather than phonon-phonon interaction, as discussed previously in Figure 4.24. It is even more evident that the Ca_2RuO_4 exhibits different changes in the peak-shift and broadening compare with the doped samples, which are metals and not insulators as Ca_2RuO_4 (Figure 4.16).

Despite this, the most interesting feature in the temperature scan (Figure 4.32) is that the S3 (T3) peak at ~370 cm^{-1} of the $x = 0.3$ (0.2) doped sample disappears with increasing temperature around $T_0 \sim 180$ (250) K.
This temperature can be associated with the transition between the orthorhombic and tetragonal phase with increasing T [65]. For the sample $x = 0.3$, our temperature is different from the $T_0 \sim 220$ found in [65]. The discrepancy might lie from a local heating of the laser beam.[12] For the $x = 0.2$ sample, in the literature there are no results about the temperature of this transition.

---

[12] This feature is consistent with the lower transition temperature T_N detected in Ca_2RuO_4 from the temperature dependence of M1 (Figure 4.22). In that case, we found $T_N \sim 60$ K instead of $T_N \sim 110$ K, with a difference comparable to what we observe here for T_0. This interpretation is further supported by the fact that all measurements were performed with the same laser power (~ 8 mW).

Although in Ca_2RuO_4 the corresponding peak A8 still be present at 290 K, it shares a similar decrease of intensity, broadening and redshift with increasing temperature. As a consequece of the metal to insulator transition occuring at about 165 K, the doped sample with $x = 0.1$ broke when we tried to perform these measurements and therefore no results are reported. However, from the room temperature spectra (Figure 4.13) we clearly can argue that T_0 is above 300 K.

A more quantitative analysis is shown in Figure 4.33, where (a-c) display the temperature dependence of the phonon energy shift (with respect to the energy at 1.8 K) for the doped sample with $x = 0.3$, $x = 0.2$, and $x = 0$, respectively. The peak positions are calculated by fitting the modes with Lorentzian and Voigt functions. The inset displays the integrated intensity (normalized by the value at 1.8 K) over a window of $\pm 6\,\mathrm{cm}^{-1}$ with respect to the peak position in function of the temperature.

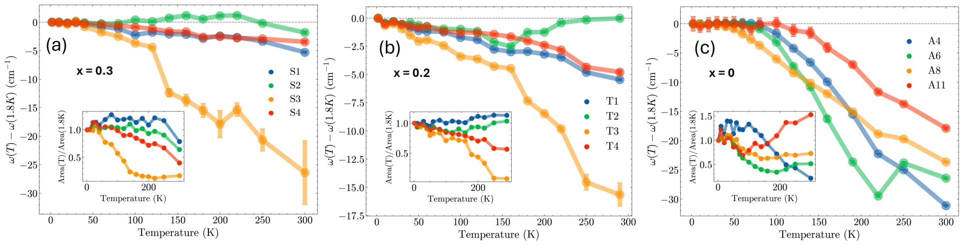

Figure 4.33: Temperature dependence of the A_g phonons of the doped samples. In (a)-(b)-(c) is plotted the energy-shift compared to the energy at 1.8 K for $x = 0.3$, $x = 0.2$, and $x = 0$, respectively. The position is obtained by fitting with Lorentzian or Voigt functions. The inset displays the integrated intensity over a spectral window of $\pm 6\,\mathrm{cm}^{-1}$ with respect to the peak position. In Figure (a) it is noticeable that at $T \sim 120$ K there is a dramatic decrease of energy for S3 and an increase of energy for S2. Similar behavior at $T \sim 180$ K is registered in (b) for T3 and T2.

It can be observed that the peaks S1 and S4 (and the corresponding phonons T1 and T4 in the $x = 0.2$ compound) exhibit a similar redshift of about $\sim 5\,\mathrm{cm}^{-1}$ with increasing temperature. Such a shift is expected, since heating generally enhances anharmonicity and thermal expansion, which reduce the phonon frequencies. By contrast, the corresponding phonons in $x = 0$ (A4 and A11) show a larger redshift of ~ 15–$30\,\mathrm{cm}^{-1}$, likely related to its insulating character or to the elongation of the octahedra along the c axis (see Section 4.2.3.3 for details).

This conventional behavior is not shared by S2 and S3, which display unusual trends. For $T > 120$ K, S2 shifts to higher frequency with temperature, while S3 shifts dramatically to lower frequency by $\sim 27\,\mathrm{cm}^{-1}$. A similar pattern is observed for T2 and T3 in the $x = 0.2$ sample, although the anomalies ap-

pear only above $T > 160\,K$, with T3 decreasing by $\sim 15\,cm^{-1}$. These anomalies are also reflected in the temperature dependence of the integrated intensities (see inset).
No such anomalous behavior is observed in the $x = 0$ compound: A6 and A8 follow frequency-shift trends comparable to A4 and A11. However, A6 exhibits an additional feature for $T > 250\,K$, where it splits into two peaks.[13]

The anomalous behavior of S2 and S3 (and T2 and T3) indicates structural instabilities near the characteristic temperature T_0 and suggests that these phonons are the most strongly involved in the structural transition. This transition is marked by the suppression and pronounced frequency decrease of the S3 (T3) mode, accompanied by a shift of S2 (T2) to higher frequency. The absence of such behavior in Ca_2RuO_4 suggests two possibilities: (i) the parent compound does not undergo an orthorhombic–tetragonal transition in the studied temperature range, and/or (ii) the phonons driving the transition are not the same as those in the doped compounds.

To study the structural transition in more detail, we analyze the integrated area of the characteristic phonons (S2, T2, and A8) and compare their temperature dependence (Figure 4.34). The results show clearly that Sr doping lowers the critical temperature T_0. This is consistent with the interpretation of this transition as an orthorhombic-to-tetragonal distortion [65]. Indeed, increasing Sr concentration drives the system closer to Sr_2RuO_4, which is tetragonal at all temperatures, and therefore requires less energy to move to a higher symmetric structure.

---

[13] For $T > 250\,K$, we report the area and peak position of the higher-frequency component (see Figure 4.32c).

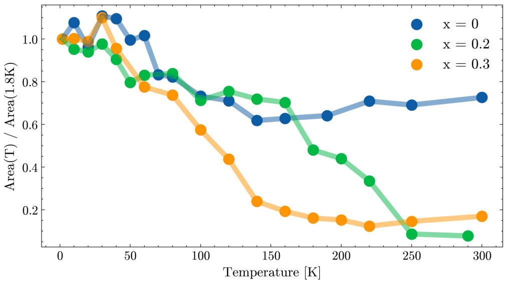

Figure 4.34: Structural-transition comparison between $x = 0$, $x = 0.2$, $x = 0.3$. It displays the integrated intensity of the phonon associated with the structural transition. In particular, S3, T3, and A8 for the $x = 0.3$, $x = 0.2$, $x = 0$ samples (see Figure 4.32). The intensity is normalized at 1.8 K. It can be observed that both doped samples undergoes to a structural transition, while Ca_2RuO_4 might not exhibit this transition or it might be at higher temperature. Moreover, it is noticeable that the increase of Sr reduces the temperature T_0 related to the second-order structural transition. This feature is consistent with the suggestion of this transition as a structural transition between orthorhombic to tetragonal [65]. In fact, the increase of Sr atoms brings the system to be closer to Sr_2RuO_4, which has a tetragonal structure at all temperatures. Therefore, the sample needs less energy to move to a more simmetric structure.

4.2.3.3 *Evidence of Metallic State*

In order to understand better the insulating behavior observed in the I-V measurements (Figure C.1b in appendix C), we decide to do a comparison between the peak-shift with temperature of the corresponding mode at around 426 cm^{-1} in the Raman spectra of the doped sample with $x = 0.2$ and Ca_2RuO_4, as shown in Figure 4.35. We choose this phonon mode because in [64] they use it in temperature-dependent Raman experiments to show the metal-insulator transition.
In particular, Figure 4.35(a)-(c) show the Raman spectra of $x = 0.2$ and Ca_2RuO_4, while Figure 4.35(b)-(d) the energy of the mode at each temperature. The energies are calculated by fitting the mode with a Fano profile.

From the Raman spectra it can be seen that the overall energy-shift is one order of magnitude less between $Ca_{1.8}Sr_{0.2}RuO_4$ ($x = 0.2$) and Ca_2RuO_4. Since there are no significant reasons why the phonon-phonon interactions might be different in these samples, the discrepancy might come from the insulating behavior of Ca_2RuO_4. Indeed, the electrons are less free to move and might interact more with the phonons.
Moreover, in [64] is used the energy and bandwidth changes of this mode to show the metal-insulator transition in $x = 0.06$ and $x = 0.09$ samples. In particular, in the metallic state there are no significant changes in energy.
This might confirm that the insulating behavior observed in Figure C.1(b) for the $x = 0.2$ sample is not related to the metal-insulator transition and that our

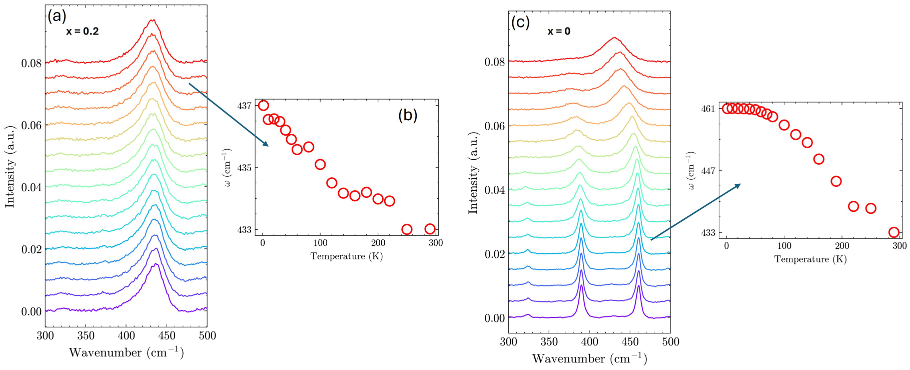

Figure 4.35: Comparison of the B_{1g} mode-shift with temperature with doped $x = 0.2$ and Ca_2RuO_4. In (a)-(c) are shown the Raman spectra in the B_{1g} configuration at different temperatures for $x = 0.2$ and $x = 0$ samples, which corresponds to Ca_2RuO_4. In (b)-(d) are plotted the energy shift of the corresponding phonon mode indicated by the blue arrows. The overall energy-shift of $x = 0.2$ from 1.8 K to 300 K is one order of magnitude less compared with the corresponding one in $x = 0$. Assuming that the phonon-phonon interaction is similar in both samples, the reason behind this might be found in the electron-phonon interaction. This analysis, similar to the one in [64] for the $x = 0.06$ and $x = 0.09$ compounds, might confirm that the insulating behavior observed in the I-V measurements in Figure C.1(b) is not related to a metal-insulator transition.

sample might still exhibit metallic behavior.
Since the $x = 0.3$ sample exhibits metallic behavior in the I-V measurements (Figure C.1a) and the overall energy-shift was comparable to what we already observed in $x = 0.2$, we have not reported here this result.

5

RAMAN SCATTERING OF RUTHENATES IN MAGNETIC FIELD

In this chapter, we investigate the effects of an external static magnetic field on the Raman response of ruthenate compounds, with a particular focus on Ca_2RuO_4 and Sr_2RuO_4. Ca_2RuO_4 displays an antiferromagnetic ground state originating from the interplay between spin, lattice, and orbital degrees of freedom.

Raman spectroscopy, owing to its sensitivity to both vibrational and magnetic excitations, serves indeed as a powerful probe for exploring field-induced phase transitions, symmetry breaking, and coupling mechanisms in these systems.

For performing magnetic-field dependent Raman measurements in a fixed polarization configuration, correcting for the Faraday rotation effect of the set-up would be crucial. We will show this correction in the first part of the chapter, togheter with some test measurements on the non-magnetic compound Sr_2RuO_4, which prove the accurance of the correction protocol.

In the second part of the chapter, we study the effect of a magnetic field on the magnetic and vibrational excitations observed in the antiferromagnetic ground state of Ca_2RuO_4. Particular attention is given to the magnetic features of the AF ground state previously identified in zero-field measurements—such as two-magnon scattering and the Higgs mode in Ca_2RuO_4.

All subsequent measurements in this chapter were performed using the *cryostat-coupled Raman setup* (Figure 2.3) operated in single-stage mode with a 1200 grooves/mm grating. The average laser power was maintained at ~ 8 mW.

5.1 CORRECTION OF THE FARADAY ROTATION EFFECT

Under the influence of magnetic fields, in most optically transparent dielectric materials the Faraday effect takes place. This effect is a physical magneto-optical phenomenon, which causes a polarization rotation which is proportional to the projection of the magnetic field along the direction of the light propagation. The relation between the angle of rotation of the polarization and the magnetic field in a trasparent material is:

$$\beta = \nu H d \tag{5.1}$$

where β is the angle of rotation, H is the magnetic flux density in the direction of propagation, d is the lenght of the path where the light and magnetic field interact, ν is the Verdet constant for the material. This constant varies with wavelength and temperature [81–83].

In Figure 5.1a is shown a scheme of this effect, where the pink shaded cilinder corresponds to the transparent material. Our setup is described schematically in Figure 5.1b.
We have to consider that the light propagation and the magnetic field are both parallel along the z-axis. Since we are in a back-scattering configuration, the Faraday effect compromises both the incoming and outcoming polarization. The effect is assumed to be the same because the incident and the back-scattered light travel the same path.

In our set-up the major contribution of the Faraday effect comes from the microscope objective and optical windows. Indeed, the sample might not play a crucial role because we are collecting the reflected beams of samples with a short penetration depth $\sim 1 - 10\,\mu m$[1]. In particular, the penetration depth for a red laser in transition metal oxides such as Ca_2RuO_4 is around $3\,\mu m$ [85]. In Sr_2RuO_4 compound δ might be even lower since the reflection is higher for its metallic behavior.

In order to estimate the polarization rotation, we rotated the $\lambda/2$ before the sample so that, at different magnetic fields, the polarization of the outcoming light is fixed. In this way, the Faraday rotation of the optical elements can be mapped as a function of the magnetic field onto the angle of the $\lambda/2$. The results are shown in Figure 5.2, where is clear the linear dependence of the angle with the magnetic field.

The angle θ has two contributions, one for the incoming beam until it interacts with the sample and the other one for the reflected beam after the interaction:

---

[1] The penetration depth is defined as $\delta = \frac{\lambda}{4\pi k}$, where k is related to absorption by the complex refractive index $\tilde{n} = n + ik$.

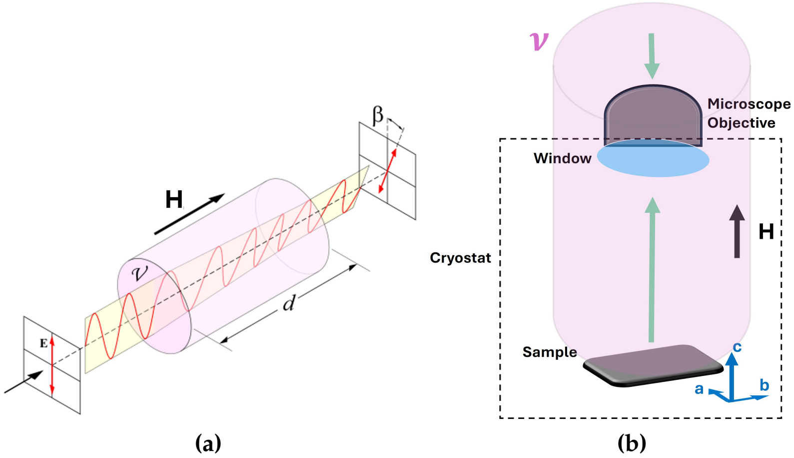

Figure 5.1: Schemes of the Faraday effect. In (a) is represented the general effect, which consists in the rotation β of the polarization of the light E in presence of a external magnetic field H. The rotation is given by $\beta = \nu H d$, which depends on the medium by the Verdet constant ν. Image is taken from [84]. In (b) is described a scheme of our set-up for these measurements. In shaded pink is shown the *medium* which contributes to the Faraday rotation. The contribution is given from the incoming beam (green light pointing downwards) and refracted one (upwards). The external magnetic field H is parallel to the propagation of the light.

$\theta = \theta_{before-sample} + \theta_{after-sample}$.
Once obtained θ of the $\lambda/2$ for each magnetic field, we rotate the first $\lambda/2$ of $\theta/2$. In this way, we correct the incoming polarization before the interaction with the sample. After that, we correct the $\theta_{after-sample}$ using a second $\lambda/2$ rotated by $\theta/2$. In this way, we correct the outgoing beam before the spectrometer. In doing that, we are assuming that $\theta_{before-sample}$ and $\theta_{after-sample}$ contribute equally, which is reasonable because the optical elements and path are the same.
It is important to note that these corrections were made using the light scattered from Sr_2RuO_4.

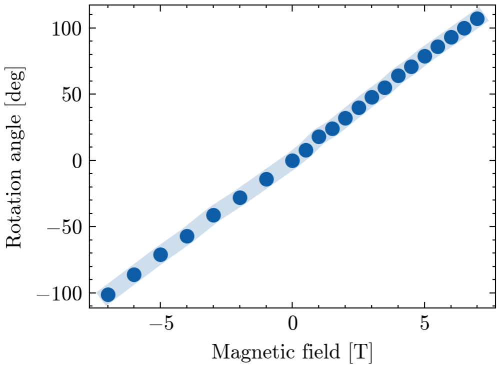

Figure 5.2: Faraday rotation characterization: Dependence of the polarization rotation of the scattered light due to the Faraday effect of the optical elements of the set-up. For this calibration we collect the light elastically scattered from Sr_2RuO_4.

5.2 SR2RUO4

5.2.1 *Magnetic field dependence*

In this section we present the Raman measurements of Sr_2RuO_4 in magnetic field. We took this sample as a benchmark material, where no magnetic behaviour is observed in its ground state, to prove the accurancy of the Faraday correction protocol. In particular, these measurements are performed at 1.8 K in both B_{1g} and A_g channels. The external static magnetic field is applied along the c-axis and is sweeped from $0\,T$ to $+7\,T$. The results are shown in Figure 5.3. The A_g channel is reported in Figure 5.3(a) and the B_{1g} channel in Figure 5.3(b).

In the A_g channel, the two A_g modes are not affected by the presence of an external magnetic field. There are no changes in energy or bandwidth. Considering the nature of these modes, as discussed in the previous chapter, the apical oxygen vibrations along the c-axis and the vibrations of the in-plane oxygen do not depend on an external magnetic field along the c-axis.
Although the sample does not exhibit any magnetic order compared to the samples $Ca_{2-x}Sr_x2RuO_4$ with $x < 0.1$, this consideration might be important for the results reported in [86]. Indeed, this work predicts the presence of an orbital-selective altermagnetic state[2], driven by octahedral distortions, which are induced by the vibrational modes, and accompanied by weak in-plane ferromagnetism through an extension of the spin-orbit coupling. Following these considerations, it seems that the magnetic field along the c-axis does not

---

[2] Altermagnetism is a new form of magnetism, which consists on an antiferromagnetic state in the real space (therefore no zero-net magnetization) and ferromagnetic state in the reciprocal space (band-splitting) [53].

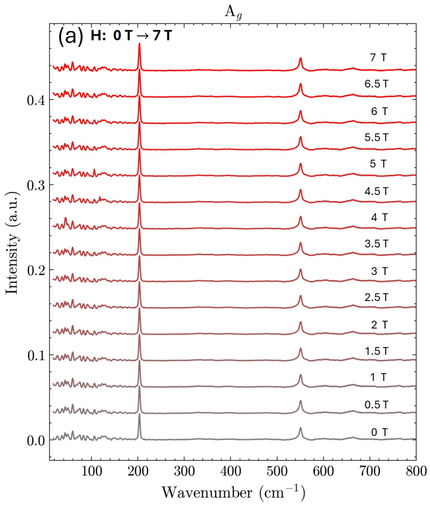

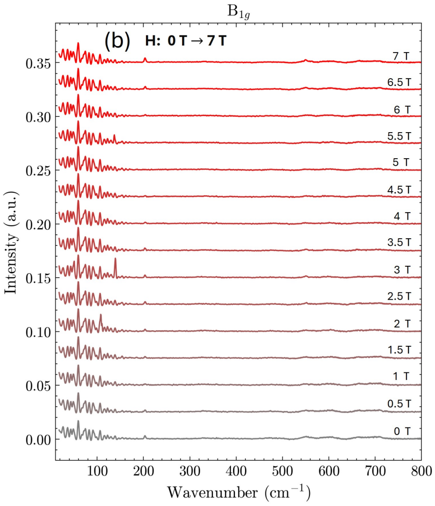

Figure 5.3: Raman spectra in magnetic field of Sr_2RuO_4 at 1.8K: in (a)-(b) are shown the Raman spectra at different magnetic field values for A_g and B_{1g} channels, respectively. The external static magnetic field is changed from 0 to 7 T and applied along the c-axis (z). In (a) the two A_g modes are not affected by the magnetic field. Similarly in (b) there are no significant changes. The spectra are shifted for clarity.

play a role in this context. Probably because it inhibits the predicted in-plane ferromagnetism or plays an opposite role to the distortions induced by the vibrational modes, which are necessary for the altermagnetic state.

In the B1g channel (Figure 5.3b), no phonon modes associated with the sample are present. Moreover, there are no significant changes in the background at low energy as observed in the temperature scans (Figure 4.30). We underline that, in Sr_2RuO_4, where no magnetic order exhist in the ground state, no significant variation of the Raman modes are observed in magnetic field. This proves that the Faraday correction protocol employed works properly.

5.3 CA2RUO4

5.3.1 *Hysteresis measurements*

Previous studies [87, 88] have reported the magnetization curves of Ca_2RuO_4. In particular, [87] showed that the S-phase, characterized by a shorter c-axis (see Chapter 3), exhibits a smaller hysteresis in the M–H curves compared to the L-phase (longer c-axis). The hysteresis is attributed to the ferromagnetic component arising from canted antiferromagnetism [87]. These measurements are shown in Figure 5.4(a).

In addition, [88] reported hysteresis when the magnetic field is applied parallel to the a or b axis. In particular, they found an evidence of a spin reorientation transition for $B = 3.5\,T$ at $T = 105\,K$ and a metamagnetic transition for $T << T_N$ at about 9 T. The metamagnetic transition consists essentially in a sudden increase in the magnetization of a material with a small change in an externally applied magnetic field. These results are presented in Figures 5.4(b)-(c).

These previous findings motivate us to investigate the microscopic behavior of Ca_2RuO_4 by examining how the Raman-active modes are modified under the influence of hysteresis when a magnetic field is applied along the c-axis in the antiferromagnetic phase of the sample at 1.8 K. The magnetic field is varied between $-7\,T$ and $+7\,T$.

Figure 5.5 shows the Raman spectra collected for the B_{1g} channel. In particular, Figure 5.5(a) displays the spectra when the magnetic field is increased from 0 T to 7 T; Figure 5.5(b) presents the spectra measured from 6.5 T to $-6.5\,T$; Figure 5.5(c) the closing loop of the hysteresis, so the Raman spectra from $-6.5\,T$ to 0 T. A similar structure is used to present the measurements for the A_g channel in Figure 5.6(a-c).

Several interesting features are present and will be discussed in detail in the following sections, including the behavior of the two magnetic modes M1 and M2 (Figure 4.17) in the B_{1g} channel (Section 5.3.1.1), the presence of a possible new magnetic mode $\sim 430 cm^{-1}$ in the same channel (Section 5.3.1.2), or the evidence of an hysteresis over the q Fano-parameter (Eq.4.1) of the mode at $\sim 322 cm^{-1}$ in the A_g channel (Section 5.3.1.3).

However, it is important to show a clear presence of the Faraday rotation, especially at high magnetic field ($H > 4T$). Indeed, the appearing of the peaks in the B_{1g} channel (Figure 5.5) are exactly the A_g modes in the A_g channel at zero magnetic field (Figure 5.6). Moreover, the presence of the A_g modes in the B_{1g} channel is accompanied by a corresponding decrease of intensity of the B_{1g} modes, and vice versa.
This phenomenon is not well corrected as in the measurements of Sr_2RuO_4

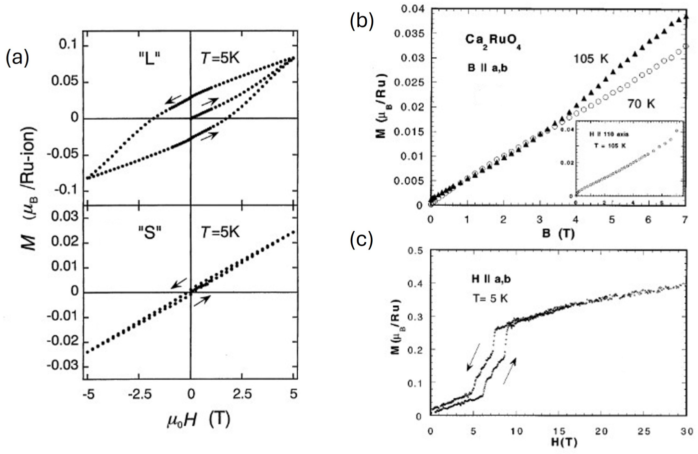

Figure 5.4: Magnetization hysteresis in Ca$_2$RuO$_4$. (a) M–H curves showing reduced hysteresis in the S-phase (shorter c-axis) compared to the L-phase (longer c-axis) [87]. Our sample remains in the S-phase for all subsequent Raman spectra. The direction of the magnetic field is not explicitly specified in [87]. (b) Magnetization versus applied field along the in-plane direction for two temperatures. The inset shows comparable data for [110] direction. The break in M vs H at 3.5 T for $T = 105$ K might be a spin reorientation transition [88]. (c) displays that at very hight field $M(H)$ shows a huge change at about 9 T, which in [88] they tentatevily associated to a metamagnetic transition. (a) is taken from [87], while (b)-(c) from [88].

(Figure 5.3) probably because we used Sr$_2$RuO$_4$ in the Faraday correction procedure, assuming that the contribution of the sample was negligible. In Figure 5.7 is shown as example the integrated intensity of the B$_{1g}$ mode at 461 cm^{-1}. It is possible to see that a decrease of the area in the B$_{1g}$ channel is accompanied by an increase in the A$_g$ channel. Specifically, this trend starts after the black dotted line inside the figures. In order to correct this effect, we plotted the sum of the integrated intensity in both channels (Figure 5.7c). This might compensate this effect, although the effect still be present.

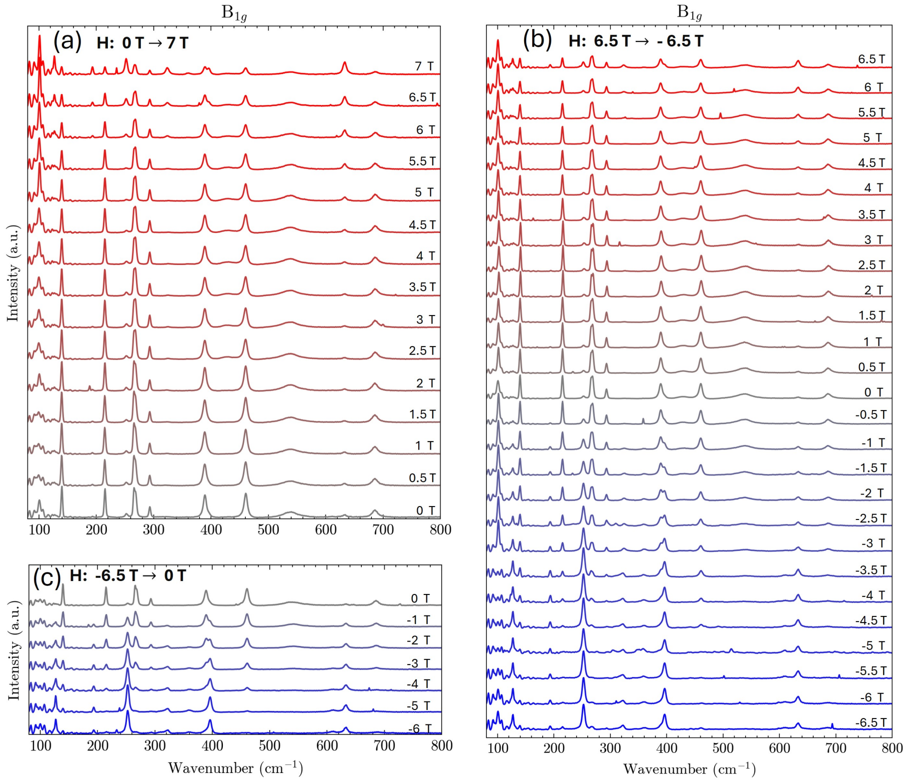

Figure 5.5: Raman measurements with external magnetic field of Ca_2RuO_4 at 1.8K in B_{1g}. The hysteresis loop is plotted starting from (a) when the magnetic field is changed from 0 to 7T, in (b) is shown from +6.5 to -6.5T and finally in (c) the closing loop from -6.5 to 0T. The presence of new modes at high magnetic field or the decrease of the intensity of the B_{1g} modes are both evidence of imperfections of the Faraday rotation correction. There is one new possible mode in the spectral window around 400-500cm^{-1}, which will be discussed in details in Section 5.3.1.2.

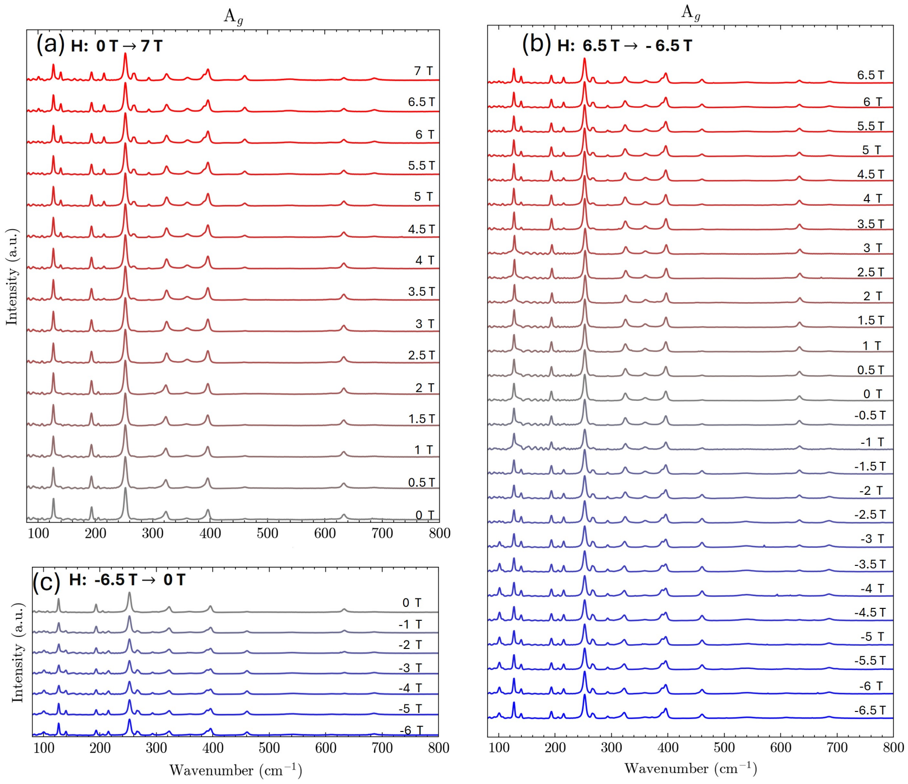

Figure 5.6: Raman measurements with external magnetic field of Ca$_2$RuO$_4$ at 1.8K in A$_g$. The hysteresis loop is plotted starting from (a) when the magnetic field is changed from 0 to 7 T, in (b) is shown from +6.5 to −6.5 T and finally in (c) the closing loop from −6.5 to 0 T. The presence of new modes at high magnetic field or the decrease of the intensity of the A$_g$ modes are both evidence of imperfections of the Faraday rotation correction. The most interesting feature in these measurements is the change of asymmetry of the peak centered at around 322cm^{-1}, which will be discussed later in Section 5.3.1.3.

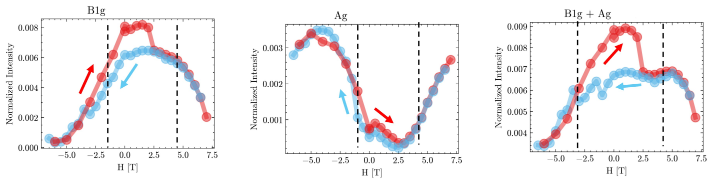

Figure 5.7: Example of integrated intensity of a B$_{1g}$ mode in the hysteresis loop. In (a)-(b) are shown the area of the peak at 461cm^{-1} in the B$_{1g}$ and A$_g$ channels, respectively, while in (c) the sum of them. It is evident the presence of the Faraday rotation that changes the relative intensity of this mode. The sum might be used in order to compensate this effect.

5.3.1.1 *Magnetic Dependence of Magnons*

In the low temperature spectrum of the previous Chapter (Figure 4.17), we showed the two magnetic modes M1 and M2. While there is general agreement in the literature about the two-magnon nature of M2 [58], the origin of M1 remains under debate. A recent theoretical study, supported by experimental data, attributes M1 to a single-magnon excitation [58].
Here, we aim to investigate how these modes are affected by the presence of an external magnetic field.

Figure 5.8(a)-(b) show a zoomed-in view of the B_{1g} Raman spectra previously presented in Figure 5.5(a). In particular, Figure 5.8(a) highlights M1, while Figure 5.8(b) focuses on M2.

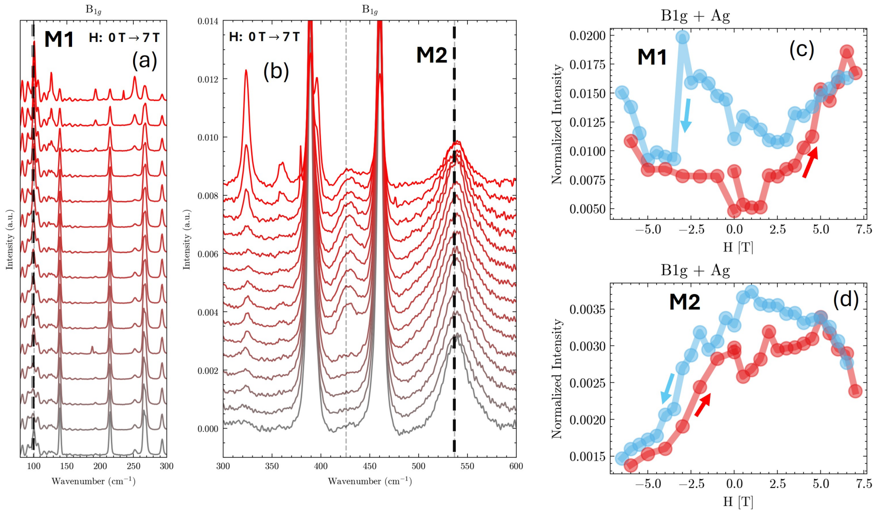

Figure 5.8: Hysteresis analysis of the two magnetic modes M1 and M2 in Ca_2RuO_4. (a)-(b) show the B_{1g} Raman spectra at 1.8 K with an external magnetic field ranging from 0 T (grey) to 7 T. Black dotted lines indicate the single-magnon (M1) and two-magnon (M2) excitations [58]. In (c)-(d) are presented the integrated intensities of M1 and M2 over the hysteresis loop, respectively. Faraday rotation is still present at high magnetic field values, but it appears to affect M1 and M2 differently. The absence of splitting of M1 might exclude its single-magnon nature.

It is clear that both modes do not exhibit splitting of its energies with an external magnetic field along the c-axis. While for a two-magnon feature is expected because it involves pairs of magnon states with opposite momenta and opposite spins with $\Delta S = 0$, it should not be visible for a single magnon feature [72]. Indeed, the latter is expected to split in an applied magnetic field due to its net magnetic moment, $\Delta S = \pm 1$ [72].
This consideration might indicate a two-magnon nature of M1, in contrast

with a recent theoretical work [58]. Further measurements with an external magnetic field along the ab plane might be useful in order to show clearly the absence of magnetic - field dependence for this mode. Indeed, the spins of the Ru ions lie along the ab plane with an ordered momentum along the b axis and small canting along c [48] (See Figure 5.9).

A more quantitative analysis is shown in Figure 5.8(c)-(d), where the integrated areas of M1 and M2 are plotted, respectively. As the external magnetic field increases, both modes exhibit lower integrated intensity compared to the opposite direction of the hysteresis loop. This trend is similar to what was observed for the B_{1g} phonon mode (Figure 5.7). This similarity suggests that the observed differences might be due to non-magnetic effects rather than intrinsic magnetic behavior. However, it is difficult to attribute this entirely to Faraday rotation, since that effect should be symmetric with respect to the magnetic field direction and is expected to contribute less at lower field values.

Overall, the intensity trend of M1 (Figure 5.8c) differs from that of M2 (Figure 5.8d). Specifically, while the area of M2 decreases with increasing magnetic field magnitude, M1 appears to increase. This behavior is particularly noticeable at high magnetic field values. Given that both modes are equally affected by Faraday rotation, this divergence suggests that the origin of the trend should originate from elsewhere. One possible explanation is that the external magnetic field modifies the magnetic excitation background underlying M2 [58], which is not present for M1. A similar argument will be discussed later to explain changes in the asymmetry parameter of the H (A_g) mode (Section 5.3.1.3).

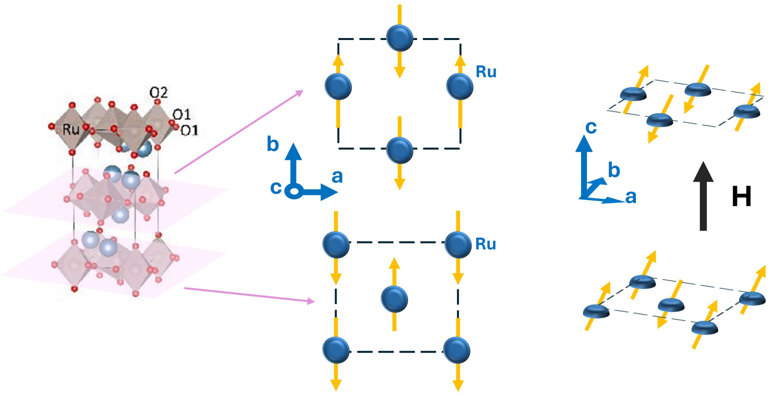

Figure 5.9: Spin configuration of Ru ions in Ca_2RuO_4. The crystal structure is adapted from [69]. Two regions are highlighted, and the corresponding spin configurations (yellow arrows) of the Ru ions (blue circles) are shown. In particular, we highlight the ab plane and its top view, where the Ru spins lie within the ab plane, with the ordered moment along the b axis and a small canting along c [48]. The external magnetic field H is shown

5.3.1.2 *Evidence of a New Magnetic Mode in Magnetic Field*

An interesting feature, is underlined in Figure 5.10(a), which shows the B_{1g} Raman spectra (Figure 5.5a) over the spectral window of $300-500\,cm^{-1}$. For $H > H_c = 2.5\,T$, a new mode appears at $\sim 432\,cm^{-1}$ between the two B_{1g} phonons (B6 and B7) discussed previously in the Low temperature spectra (Figure 4.17).

It is noticeable that this new mode is centered close to the difference value of M2 and M1,

$$M2 - M1 \sim 534 - 101 = 433\,cm^{-1}.$$

Crucially, this mode does not correspond to any A_g phonon, as shown by the A_g spectrum at 0 T in Figure 5.10(b). The lack of a counterpart in the A_g spectrum confirms that its emergence is not due to Faraday rotation, which would introduce A_g modes into the B_{1g} spectrum. Moreover, although Faraday rotation significantly affects the measurements for $H > 6$ T—as evident in Figure 5.10(a) from the two A_g phonons near 320 and 360 cm^{-1}—the M2–M1 feature appears well before, at $H_c = 2.5$ T < 6 T.

Additionally, the integrated intensity of this new mode exhibits a hysteresis as depicted in Figure 5.10(c).[3] This plot clearly shows that starting from zero-magnetic field, the hysteresis of M2-M1 mode is not symmetric respect with zero magnetic field. In particular, positive H_C is at $2.5\,T$, while negative H_C is at $-3.0\,T$.

---

[3] The integrated window is $\pm 7\,cm^{-1}$

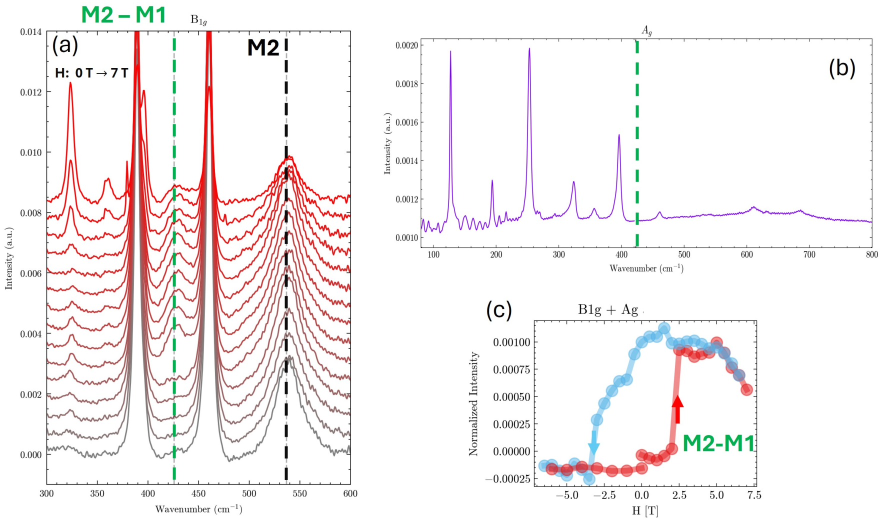

Figure 5.10: Evidence of a new mode in the Raman spectra of Ca_2RuO_4 with external magnetic field. In (a) are shown a zoom-in of the Raman spectra in Figure 5.5(a) over 300-600cm^{-1}, where the black dotted line indicates the two magnon M2, while the green one a new mode for $H > H_c = 2.5$T. The energy of this new mode (M2-M1) is comparable with the difference of the energy of M2 and M1 (see Tab.4.1). (b) shows the A_g Raman spectra at 1.8K with $H = 0\,T$. There is no phonon at the M2-M1 energy, proving that this mode is not associated with the Faraday rotation (clearly visible for the two peaks at 320 and 360 cm^{-1}). In (c) is shown the integrated intensity of M2-M1 in the hysteresis measurements presented in Figure 5.5-5.6. The integrated intensity of this new mode clearly exhibits a hysteresis, which might originate from a spin flop transition.

In order to prove the magnetic origin of this new mode, we perform a temperature scan at $H = 4\,T$ for the B_{1g} geometry. The results are presented in Figure 5.11(a)-(b), where are shown the Raman spectra from $1.8\,K$ to $190\,K$ over two spectral windows, $90 - 300\,cm^{-1}$ and $300 - 750\,cm^{-1}$, respectively. The behavior of M2-M1 is similar to M1 and M2. The integrated intensity of them clearly reveals that start to appear at $\sim 90\,K$, comparable with $T_N = 110\,K$ [49]. This analysis is displayed in Figure 5.11(c). This similarity between the intensity-dependence with temperature between the two magnons (M1 and M2) point to a magnetic origin of this emergent mode.

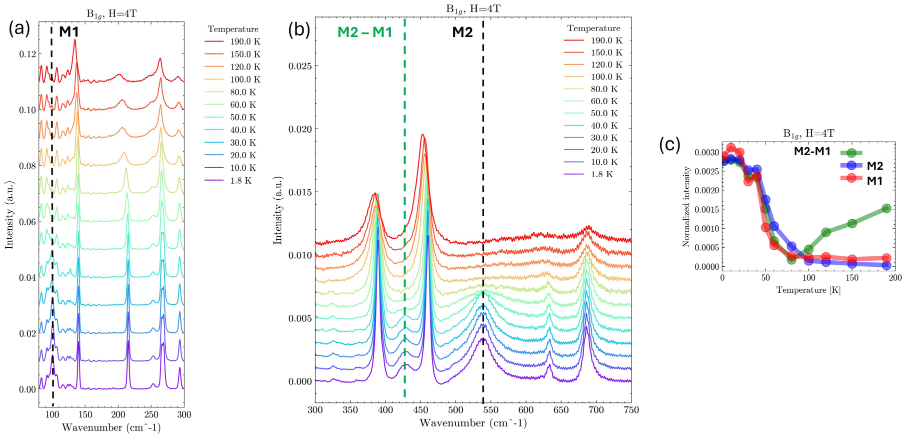

Figure 5.11: Temperature dependence of the magnetic modes in the presence of a magnetic field. In (a)-(b) are presented the B_{1g} Raman spectra at $H = 4\,T$ and $1.8K < T < 190\,K$. Dotted lines indicates M1, M2 (black) and M2-M1 (green). (c) shows the integrated intensity of these modes, which exhibits the same trend: the intensity increases for $T < T_N = 110\,K$. This strongly suggests the magnetic nature of this new mode (M2-M1).

One possible explanation might be that the system undergoes a spin-flop transition [88]. Since the system is canting along the c-axis [48], as shown in Figure 5.9, if the magnetic field is pointing along the same direction of the canting, it can induce a magnetization perpendicular to the easy axis (b) where all the Ru spins are aligned. In this new magnetic order, it might be possible that the difference between M2 and M1 is energetically favorable respect with the antiferromagnet in plane ab. The induced magnetization along the c-axis finds evidence in [87], where they attribute the hysteresis in Figure 5.4(a) to the ferromagnetic component arising from canted antiferromagnetism. For instance, this new mode might be related to a symmetry-change of the system caused by an induced magnetization along c, which might happen with an unclear re-ordering of the spins along the direction of the canting.
Further studies are needed in order to comprehend better these results, in order to clarify if the energy is related to M1 and M2 and, if not, which is its

origin. Moreover, it is strongly important to see what happens if we start the hysteresis loop with a negative magnetic field (opposite to the canting) instead with a positive one.

5.3.1.3 *Behaviour of the magnetic Higgs mode in magnetic field*

In the A_g Raman spectra shown previously (Figure 5.6), we focus on the behavior of the A_g mode at $\sim 320\,\mathrm{cm}^{-1}$, which corresponds to A6 in the DFT simulation of Chapter 4 (Figure 4.18). In particular, we report a zoom over the spectral window $200-500\,\mathrm{cm}^{-1}$ of the A_g Raman spectra from $0\,\mathrm{T}$ to $+7\,\mathrm{T}$ (Figure 5.12a). The mode under study is labeled H and indicated by a pink dotted line.
A theoretical model in [58] predicts a Higgs mode near 322.6 cm^{-1}, as shown in Figure 5.12(b). In this framework, the Higgs mode is an oscillation of the amplitude of the order parameter between (i) a state in which all Ru ions remain in the non-magnetic $J=0$ ground state and (ii) a coherently mixed state with $J=0$ and $J=1$ character produced by intersite exchange, which admixes $J=1$ even though $J=0$ is locally favored [58]. The origin of this mixed state is described by the excitonic-magnetism model of d^4 Mott insulators [57] (see Figure 3.5).
Figure 5.12(c) sketches the single-ion multiplet structure: the ground-state singlet s ($J=0$) and the triplet T_x, T_y, T_z ($J=1$). The splitting between T_z and $T_{x/y}$ arises from the tetragonal crystal field, while the further T_x–T_y splitting into T_a and T_b is due to orthorhombic distortions [58]. The set $\{s, T_a, T_b\}$ forms the basis used for the coherent phase between $J=0/J=1$ and for the magnetic model of [58], which yields the Higgs energy in Figure 5.12(b). In particular, the Higgs mode is associated with the modulation

$$\delta E = E_T\, \delta n_T, \tag{5.2}$$

where E_T is the energy difference between the singlet s and the triplet T (Figure 5.12c), and δn_T is the change in the $J=1$ (particularly T_x,T_y) occupation inside the coherent phase (grey region in Figure 5.12c). In [89], they estimate $n_T \sim 0.25$ for Ca_2RuO_4, placing the material near the critical point between the paramagnetic phase (mostly $J=0$, non-magnetic) and the antiferromagnetic phase (coexistence of $J=0$ and $J=1$).
With these considerations, we compute the integrated intensity of the H mode, as done for M1, M2, and M2–M1. The results are shown in Figure 5.12(d). Although the hysteresis is less pronounced than M2-M1 one (Figure 5.10c), it is essentially the mirror image: at the start of the cycle the H-mode intensity decreases for $H > H_c \simeq 2.5$ T, opposite to M2–M1. The critical field H_c is comparable to that reported in Figure 5.10(c).

To illustrate how the spectral weight of the H mode evolves with magnetic field, we plot, for all hysteresis measurements, the difference between each

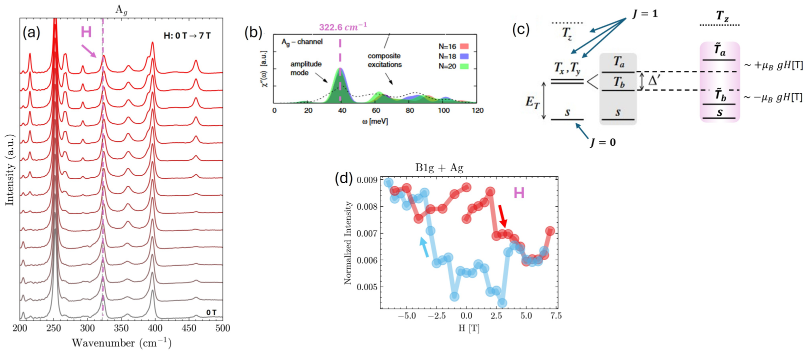

Figure 5.12: Behavior of the H mode in Ca_2RuO_4 at 1.8 K under an external magnetic field. (a) Zoom of the A_g Raman spectra in Figure 5.6a. The mode at ~ 322 cm^{-1} is labeled H (pink dotted line). It corresponds to the A_6 phonon mode in the DFT simulation of Figure 4.18. (b) Results from a theoretical model predicting an amplitude (Higgs) mode (adapted from [58]). This mode is associated with oscillations between the $J = 0$ state and the coherently mixed $J = 0/J = 1$ phase [57]. (c) Single-ion multiplet structure of Ru^{4+}: a ground-state singlet s ($J = 0$) and excited triplet levels T_x, T_y, T_z ($J = 1$). The tetragonal crystal field lifts T_z [89], and orthorhombic distortions further split T_x and T_y into T_a and T_b. The grey shaded region marks the basis used to describe the coherent $J = 0/J = 1$ phase (adapted from [58]), while the pink shaded region indicates our suggestion on how the external magnetic field modifies these energy levels via the Zeeman effect. (d) Integrated intensity of the H mode obtained from the summed A_g and B_{1g} Raman spectra (Figures 5.5–5.6). The H mode exhibits hysteresis with a trend opposite to M2–M1 (Figure 5.10c), although the corresponding H_c values are comparable.

spectrum and the initial 0 T spectrum at the beginning of the loop. The results are shown in Figure 5.13.

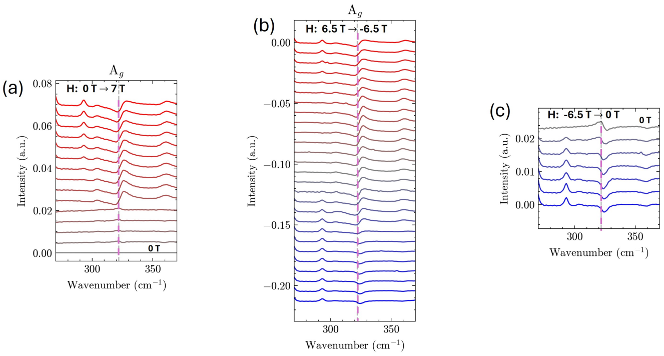

Figure 5.13: Magnetic field-induced spectral-weight changes of the H mode via difference spectra (1.8 K). For each A_g Raman spectrum in Figure 5.6, we plot the spectrum at field H minus the initial 0 T spectrum at the beginning of the loop. For $H > H_c$, a higher-energy peak develops next to the H mode; it persists upon decreasing the field and is strongly suppressed near $-H_c$. On returning to 0 T, a residual difference remains, revealing hysteresis and suggesting a field-induced shift of the Higgs-mode energy. In pink dotted line is indicated the H mode energy.

For $H > H_c$ the spectral weight around H is redistributed and a higher-energy peak appears adjacent to H. This peak persists as the field is decreased and remains visible down to $-H_c$, where it is strongly suppressed. Notably, when the system returns to 0 T, the spectral weight differs significantly from the initial reference. These observations suggest a magnetic field-induced shift of the underlying Higgs mode near H. It would be interesting to track the Higgs-mode energy versus magnetic field; a possible mechanism is Zeeman splitting of the $T_{a/b}$ levels (see pink region in Figure 5.12c), which modifies E_T and thus the Higgs-mode energy (Eq. 5.2).

In order to understand the interplay of phonons with the amplitude mode in Figure 5.12(b), we fit the H mode with a Fano-profile (Eq.4.1) and extrapolate the q parameter, which is associated with the streght of the coupling between phonon and the continuum of magnetic excitations [73]. The results are reported in Figure 5.14. In particular, in Figure 5.14(a-c) are plotted a zoom of A_g Raman measurements reported previously in Figure 5.6, while Figure 5.14(d) shows the results of the fits. The inset displays the asymmetry parameter, calculated as $1/q$.

These results clearly show an hysteresis of the q parameter. The change of asymmetry is visible also looking at the Raman spectra in Figure 5.14(a-c), where the black dotted lines indicate the change of sign of q.

The hysteresis in Figure 5.14(d) shows that H_c is centered around $\sim 2T$ when increasing the magnetic field, and ~ 2.5T in the opposite direction. Moreover, the inset suggests that the intensity of the coupling is different in the two directions. In the first cycle, the coupling is reduced by 75% of its value by $H > 2$T and this intensity is maintained until $H < -2.5$T, in which it presents similar intensities of the ones at the beginning of the loop.

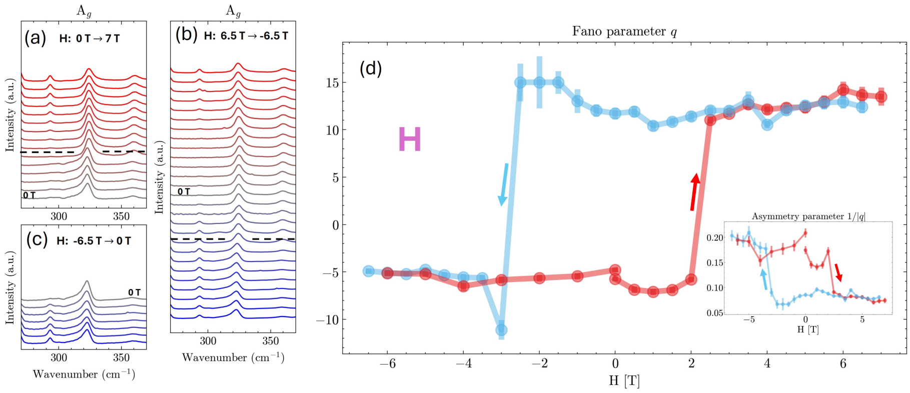

Figure 5.14: Hysteresis of the asymmetry-Fano parameter of the H mode. In (a-c) are plotted a zoom of the H mode in the A_g Raman spectra in Figure 5.6. Black dotted lines indicate the change of asymmetry for the H mode. In (d) is shown the Fano-parameter q extraded by fitting the H mode with a Fano-profile (Eq.4.1). It is noticeable the change of sign of q after a critical field, which is $H_c = 2(2.5)$T when increasing (decreasing) the magnetic field. The inset displays the asymmetry parameter $1/q$, which is proportional to the coupling between H mode with the continuum of magnetic excitations. These results strongly support the idea that the q parameter of H mode could serve as the order parameter for describing a possible first-order phase transition induced by an external magnetic field.

These results strongly support the idea that the q parameter of H mode might be used as the order parameter to describe a possible first-order phase transition induced by an external magnetic field.

A reasonable explanation of this transition might be found in the interplay of phonons with the amplitude mode in Figure 5.12(b). As discussed in [58], there are two possibilities. First, Ag phonons involving rotations and tiltings of RuO_6 octahedra modify the Ru-O-Ru bond angle, thus modulating the exchange J in a symmetric fashion. Second, deformations of the octahedra affect the splitting among t_{2g} orbitals, thus modulating E_T owing to the different orbital composition of the s and T states. Both mechanisms provide a natural coupling of phonons to oscillations of the condensate density n that is determined by the ratio E_T/J [58].

These two mechanisms are present in the H mode. In fact, as shown in Figure 4.18, H mode (A6) involves rotations and tiltings of RuO_6 octahedra. This interpretation might influence the coherent phase between $J = 0$ and $J = 1$, which is reflected to the change of coupling between H and the Higgs mode.

Another explanation might be found by studying the energy dependence of the Higgs mode in an external magnetic field, although this does not explain why the coupling exhibits hysteresis. Moreover, it remains unclear whether this transition is related to a spin-flop transition, which would link this feature to the one previously observed in the M2–M1 mode (Figure 5.10). The similar value of the critical field, $H_c \sim 2.5\,\mathrm{T}$, supports this latter interpretation.

6

TIME-RESOLVED RAMAN IN THE ANTIFERROMAGNETIC STATE OF CA2RUO4

The layered ruthenate Ca_2RuO_4 is a paradigmatic example of a 4d Mott insulator in which charge, spin, orbital, and lattice degrees of freedom are strongly entangled. Below its Néel temperature, it stabilizes an antiferromagnetic ground state whose low-energy excitations provide a sensitive window into the interplay between spin–lattice dynamics and electronic correlations. Raman spectroscopy in the B_{1g} symmetry channel is particularly well suited to probe this regime: it captures both sharp phonon features and broad magnetic continua, most notably the two-magnon excitation, whose spectral properties reflect the underlying exchange interactions.

Time-resolved Raman scattering extends this capability into the ultrafast domain, enabling direct observation of how these excitations evolve following optical perturbations. By selectively tuning the pump photon energy to target different intersite $d^4 \rightarrow d^4$ transitions—identified in the optical conductivity as the α ($\sim 1.2\,eV$) and β($\sim 2.0\,eV$) peaks—or operating far from resonance, one can disentangle thermal from non-thermal pathways in the relaxation dynamics. This approach makes it possible to track, in real time, the modification of phonon parameters, the suppression or recovery of magnetic excitations, and the emergence of transient scattering continua.

In this chapter, we present a systematic study of the ultrafast Raman response of Ca_2RuO_4 in its antiferromagnetic state using picosecond probe pulses at 532 nm in combination with a range of pump wavelengths. We will first present the static measurements of the B_{1g} spectrum with ps pulses, then move to time-resolved experiments under resonant and off-resonant excitation, and finally explore the wavelength dependence of the transient response. This methodology allows us to identify excitation-specific signatures in the spin, lattice, and electronic sectors, and to uncover evidence for both resonantly enhanced electron–phonon coupling and non-thermal suppression of antiferromagnetic correlations. Particularly, we focus on the B_{1g} channel, as we are interested in the dynamics of the two-magnon excitation (Chapter 4).

6.1 OPTICAL PROPERTIES OF CA2RUO4 AND MOTIVATION FOR THE EXPERIMENT

Ca_2RuO_4 is a prototypical Mott insulator that exhibits a rich interplay between charge, spin, orbital, and lattice degrees of freedom. The optical response of this compound reveals characteristic features associated with electronic excitations in the correlated Ru 4d shell. As shown in Figure 6.1, the optical conductivity spectrum displays two prominent peaks, commonly referred to as the α and β peaks, centered around $\sim 1.2\,\text{eV}$ and $\sim 2.0\,\text{eV}$, respectively.
These features have been interpreted as intersite $d^4 \rightarrow d^4$ transitions mediated by the strong electronic correlations inherent to the Mott insulating state. In particular:

- The α peak is associated with the $d_{xy} \rightarrow d_{xz/yz}$ transition [90, 91]. A probe photon energy tuned to the α-peak is expected to be particularly sensitive to tetragonal distortions (Q_θ) because this mode modulates the energy splitting between the d_{xy} and $d_{xz/yz}$ levels [92]. This transition is underlined with a red Lorentzian fit in Figure 6.1.

- The β peak is attributed predominantly to the $d_{xz/yz} \rightarrow d_{xz/yz}$ [90, 91]. A probe photon energy tuned to the β-peak is expected to be particularly sensitive to orthorhombic distortions (Q_ϵ), because this mode lifts the degeneracy of the $d_{xz/yz}$ bands and modulates their splitting [92]. This transition is underlined with a blue Lorentzian fit in Figure 6.1.

These assignments are supported by both theoretical models [92] and experimental studies [90] and displayed in Figure 6.1, where the insets show the real space form of the Q_θ and Q_ϵ distortions along with the induced modification of the orbital levels [92].

The low-energy excitations of Ca_2RuO_4, particularly those observed in the B_{1g} symmetry Raman spectrum, offer a window into the coupled spin-phonon dynamics of the system. In equilibrium, the B_{1g} spectrum between 150–800 cm^{-1} contains both sharp phonon lines and a broad continuum attributed to two-magnon scattering (Chapter 4). These features are sensitive to the underlying spin and lattice configurations and are thus ideal probes of ultrafast dynamics.

Building on the knowledge of the optical transitions, we propose a time-resolved Raman experiment with two pulses (one probe and one pump) to track the

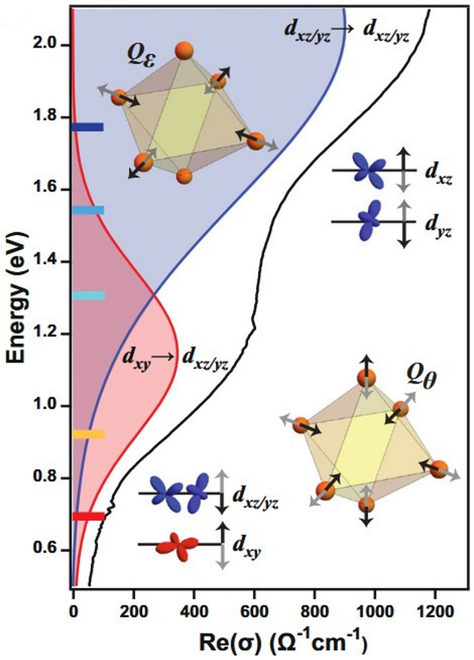

]

Figure 6.1: Optical conductivity of Ca_2RuO_4 at 11 K showing the α and β peaks. A probe photon energy tuned to the α-peak is expected to be particularly sensitive to tetragonal distortions (Q_θ), while a probe photon energy tuned to the β-peak is expected to be particularly sensitive to orthorhombic distortions (Q_ϵ). Image is taken from [92].

evolution of these low-energy modes following different photoexcitations. The setup is described in Chapter 2 (fIGURE 2.7) and involves:

- A picosecond probe pulse at 532 nm for spontaneous Raman scattering detection.
- distinct pump pulses:
  - Resonant with the α peak, designed to drive specific optical transitions.
  - Non-resonant with α and β, to disentangle thermal and electronic contributions.

By comparing the spontaneous Raman spectra acquired before and after excitation with each pump pulse, it is possible to monitor real-time changes in both phonon and two-magnon features. This approach aims to uncover the influence of selective optical excitation on spin-lattice interactions and possibly determine if the relaxation channel is dominated by magnetic, electronic or lattice excitations in the case of a resonant $d-d$ drive and an off-resonant one.

6.2 STATIC MEASUREMENTS WITH PS PULSES

Before performing the time-resolved Raman measurements, it is essential to identify the B_{1g} Raman modes in the low-temperature spectrum obtained with ps pulses at 532 nm, and to compare them with the modes observed using a continuous-wave (CW) laser, as discussed previously in Figure 4.17(a). Both spectra are collected at 1.8 K to ensure identical thermal conditions and a direct comparison. Additionally, the ps-pulse fluence is 5.6 μJ/cm², which is significantly higher than the CW fluence 3.20 nJ/cm², which is determined using a corresponding integration time of 1 ps. The integrated power of ps-pulse is much higher, and it might introduce non-linear heating since it is much shorter than the CW beam. This preliminary identification is crucial for tracking the evolution of specific modes in the subsequent time-resolved measurements, where spectral broadening from the finite pulse duration is unavoidable.

The spectral resolution in the ps-pulse spectrum is limited by the pulse duration, which is $\sim 14\,\mathrm{cm}^{-1}$ for ~ 1 ps pulses[1]. The choice of a 1 ps pulse duration represents a compromise between achieving high temporal resolution for ultrafast dynamics and maintaining a sufficient spectral resolution to distinguish the relevant modes. Measurements are performed in the B_{1g} geometry, and detection is limited by the notch filter to frequencies below $\sim 200\ \mathrm{cm}^{-1}$. The

---

[1] For a transform-limited pulse, the time–bandwidth product is approximately $\Delta\nu\Delta t = 0.44$ (for a Gaussian beam), giving $\Delta\nu \sim \frac{0.44}{1\ \mathrm{ps}} = 0.44 \times 10^{12}$ Hz $\sim 14.7\ \mathrm{cm}^{-1}$.

spectra are normalized using the same procedure described in appendix B.

The results are summarized in Figure 6.2. In Figure 6.2(a), the bottom shows the low-temperature CW spectrum discussed in Figure 4.17(a), while the top shows the corresponding spectrum measured with ps pulses. Figure 6.2(b) presents an enlarged view of the ps spectrum to highlight individual features. The observed modes in the ps spectrum are labeled as P1, P2, P3, P4, and P5 for phonon modes, and M2 for the magnon mode. They are identified by comparison with the corresponding modes in the CW spectrum, as indicated by the grey dotted arrows. In summary:

- P1: convolution of three B_{1g} phonons and a residual of one A_g phonon;
- P2 and P3: same phonon modes observed in the static measurements. Their nature is further discussed in Figure 4.26, where the intensity ratio is related to a possible orbital ordering transition [68];
- M2: two-magnon scattering [58];
- P4: phonon mode;
- P5: phonon mode.

6.3 DYNAMIC MEASUREMENTS

6.3.1 *Resonant Excitations: Pump at 700 nm*

6.3.1.1 *Pump–Probe Measurements*

Before performing time-resolved Raman measurements, we conduct pump–probe experiments to characterize the sample's transient optical response at 1.8 K. We use the *single-color PP setup* (Figure 2.9). In these experiments, the ps-probe beam wavelength was set to 532 nm, while the pump beam at 700 nm. Measurements were carried out using an optical microscope over a range of pump fluences to evaluate how the transient reflectivity change (ΔR) depends on excitation intensity. In particular, the measurements were done using a lock-in amplifier and collecting the reflected beam from the microscope with a differential detector. The probe-pulse fluence was fixed at 5.6 $\mu J/cm^2$.

The results are summarized in Figure 6.3. Figure 6.3(a) shows the transient reflectivity change as a function of the time delay between pump and probe pulses for different pump powers. In the inset, the pump–probe traces are normalized to their maximum intensity. These measurements are in good qualitative agreement with a similar fluence scan performed on the same sample

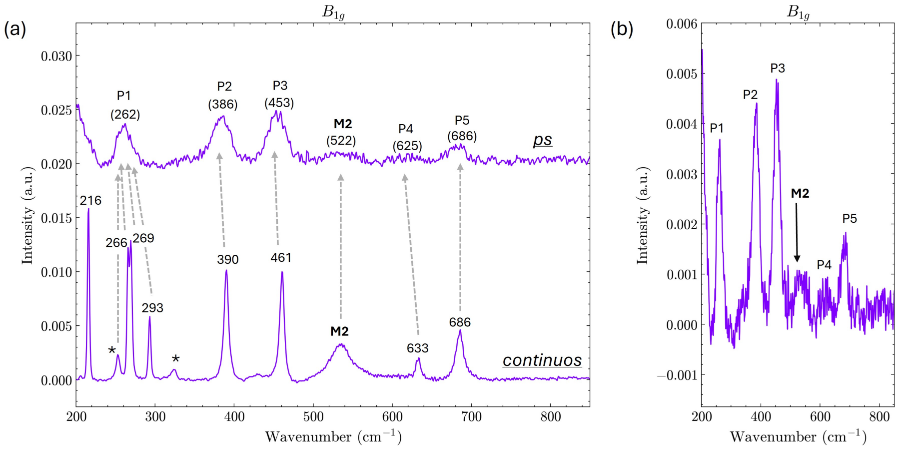

Figure 6.2: Static Raman spectra at 1.8K with ps pulses and CW laser. Comparison between static low-temperature Raman spectra obtained with a CW laser (bottom) and with 1 ps pulses at 532 nm (top) in the B$_{1g}$ geometry. Both spectra are collected at 1.8 K and normalized using the same procedure as in Chapters 4 and 5. Grey dotted arrows indicate the correspondence between the observed modes in both spectra. In (b), an enlarged view of the ps-pulse spectrum highlights the phonon (P1–P5) and magnon (M2) modes. The broader linewidth in the ps spectrum arises from the finite temporal width of the excitation, which limits the spectral resolution to ∼ 14 cm^{-1}. The Ps-pulse fluence is 5.6 μJ/cm^2, which is significantly lower than the CW fluence of 6.11 kJ/cm^2, which is determined using a corresponding integration time of 60s. The integrated power of ps-pulse is much lower, and it might introduce non-linear heating since it is much shorter than the CW beam.

using both pump and probe wavelengths at 800 nm [93].

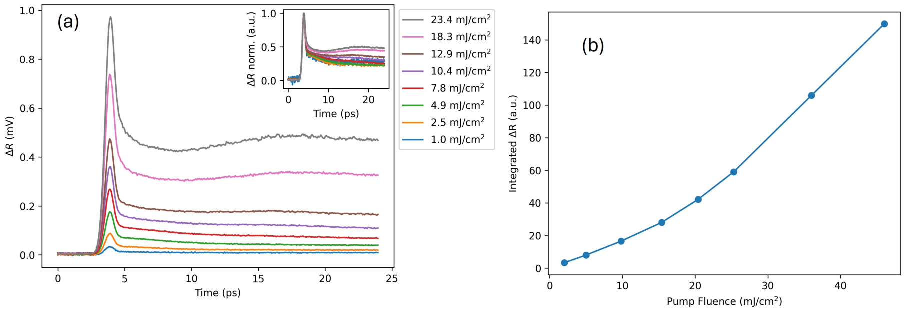

Figure 6.3: Pump–Probe measurements at 1.8 K with a 700 nm pump and 532 nm probe (ps) in B_{1g} geometry. (a) Transient reflectivity change ΔR as a function of pump–probe time delay for various pump fluences. In the inset, the traces are normalized to their maximum amplitude. At higher pump powers, a sinusoidal modulation appears, attributed to a coherent acoustic phonon mode. (b) Integrated ΔR from (a) plotted versus pump fluence, showing a linear dependence, consistent with operation in the linear excitation regime without significant nonlinear optical effects.

At high pump powers, an additional sinusoidal modulation appears superimposed on the relaxation signal. This feature is attributed to an acoustic phonon mode [94], corresponding to in-phase lattice vibrations propagating like sound waves through the crystal. Such modes are generally not observed in Raman experiments because their energies approach zero at the Brillouin zone center ($q \to 0$), making their frequencies too low—or even zero—to be Raman-active at the zone center [25].

Figure 6.3(b) presents the integrated signal from the curves in (a) plotted against pump fluence. The integrated transient reflectivity change (ΔR) increases linearly with pump fluence, indicating that the pump-induced refractive index change scales proportionally with the photoexcited carrier density. This behavior confirms that the experiment was conducted in the linear excitation regime, with no evidence of saturation or significant nonlinear optical effects within the measured range. Consequently, these conditions are well suited for subsequent measurements where avoiding nonlinear saturation effects is essential.

6.3.1.2 *Time-resolved Spontaneous Raman Measurements*

Under the same excitation conditions used in the pump–probe study, we performed time-resolved spontaneous Raman measurements to investigate the dynamics of individual phonon modes and the magnetic excitation. Each Raman spectrum was acquired with an integration time of 60 s and 40 scans. Each scan consists of one spectrum collected with the pump on and one with the pump off (see acq. scheme in Figure 2.8). The traslational stage step was set to 0.1 mm, corresponding to a temporal step of approximately $\Delta t \sim 0.67$ ps and hence compatible with the temporal resolution of the experiment governed by the ps probe.

The time-resolved (TR) Raman map is constructed as follows: the horizontal axis corresponds to Raman shift (wavenumber), the vertical axis to the pump–probe delay, and the color scale to the normalized differential signal $(\langle R_{\text{on}}\rangle - \langle R_{\text{off}}\rangle)/\langle R_{\text{off}}\rangle = \Delta R/\langle R_{\text{off}}\rangle$, where $\langle R_{\text{off}}\rangle$ denotes the average unpumped spectrum. Before computing the difference, both pumped and unpumped average spectra were normalized consistently with the static Raman measurements.

To ensure consistent excitation conditions when switching the pump wavelength, we first performed a pump–probe experiment (measured on the lock-in amplifier) and set the pump power to produce a transient reflectivity signal of approximately 1.1 mV at temporal overlap. For the present measurements, the pump fluence was 25.4 μJ/cm². The temporal overlap was then used as the reference point for the TR Raman scan.

Figure 6.4(a) presents the TR Raman map in the range 200–800 cm^{-1} and for time delays from -2 ps (before pump arrival) to $+10$ ps after excitation. Figure 6.4(b) shows the corresponding pump–probe trace. The map reveals a strong, short-lived signal near the low-energy limit at temporal overlap, which decays rapidly within a few picoseconds, as well as longer-lived features at positive times.

To better visualize these dynamics, we examine four representative horizontal cuts of the TR map: one at -2 ps (negative delay), one at overlap and near overlap at $+0.7$ ps, and one at a later delay of $+6.7$ ps. Figure 6.5(a) shows these cuts in the TR map. Figures 6.5(b–e) display the corresponding pumped and unpumped Raman spectra, while Figures 6.5(f–i) present the associated differential spectra.

At negative delay, the pumped and unpumped spectra are identical. At overlap and $+0.7$ ps, a strong low-energy enhancement appears between 200 and 300 cm^{-1}. The fast decay and broadband nature of this signal are characteristic of transient electronic Raman scattering or pump-induced continuum emission, rather than discrete vibrational modes. At $+6.7$ ps, two notable features are observed: (i) a positive signal between phonon modes P2 and P3 (approximately 412–452 cm^{-1}) and (ii) a reduction in the intensity of the M2 magnon mode. These observations indicate that the pump pulse induces a quenching of the magnon mode, an enhancement in the scattering continuum between the two phonons, and a strong, short-lived low-energy scattering component.

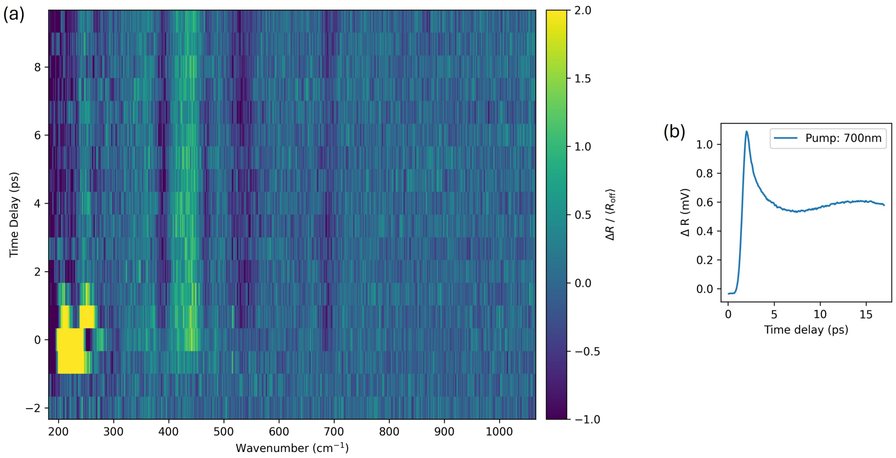

Figure 6.4: Time-resolved spontaneous Raman map and corresponding pump–probe trace at 700nm. (a) TR Raman map in the range 200–800 cm^{-1} for pump–probe delays from -2 ps to $+10$ ps. The color scale represents the normalized differential signal $(\langle R_{\text{on}}\rangle - \langle R_{\text{off}}\rangle)/\langle R_{\text{off}}\rangle$. A strong short-lived enhancement is observed at low energy near temporal overlap, along with longer-lived features at positive delays. (b) Pump–probe transient reflectivity trace measured under the same excitation conditions. Measurements are performed at 1.8K and in the B_{1g} geometry.

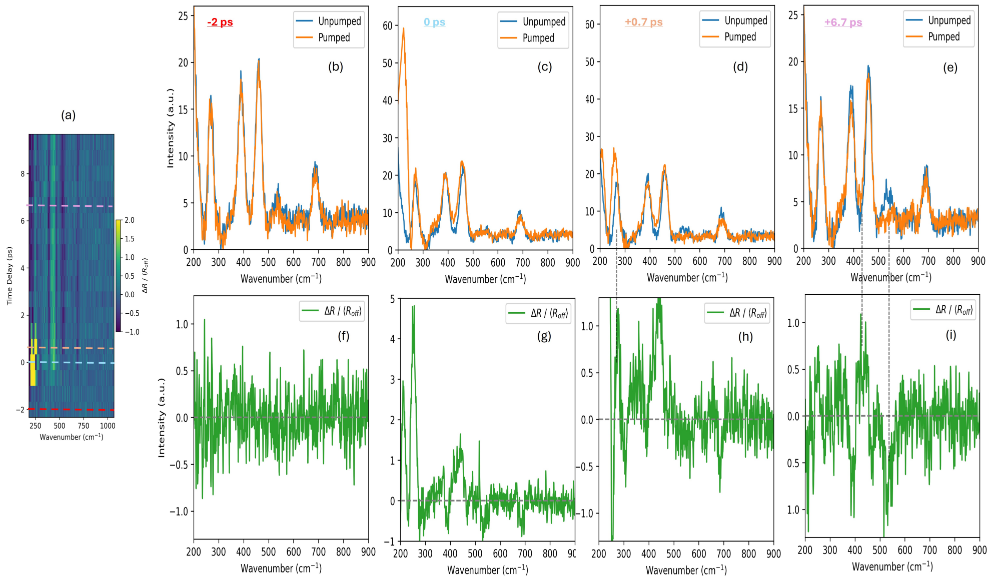

Figure 6.5: Representative time cuts from the TR Raman map. (a) TR map highlighting the four selected delay times: -2 ps, 0 ps, $+0.7$ ps, and $+6.7$ ps. (b–e) Pumped (orange) and unpumped (blue) Raman spectra at the four delays. (f–i) Corresponding differential spectra $\Delta R/\langle R_{off}\rangle$. The 0 ps and $+0.7$ ps cuts reveal a strong low-energy enhancement (arising from electronic Raman scattering), while the $+6.7$ ps cut shows increased intensity between phonon modes P2 and P3 and reduced intensity of the M2 magnon mode

To quantify these observations, we integrate the TR map over three spectral regions: the *electronic background* (EB), the *phonon* region (P), and the *magnon* region (M), as shown in Figure 6.6(a). Figures 6.6(b)–(d) display the integrated signals, which are reported by computing the difference from their average value at negative times to clearly distinguish the induced effects from the pump.

The EB signal exhibits a pronounced broadband enhancement peaking at temporal overlap and decaying within ~2 ps, consistent with nonresonant electronic Raman scattering or continuum emission followed by carrier thermalization. The P region shows a long-lived positive signal throughout the 10 ps time window, possibly arising from transient enhancement of low-energy continuum or broadened phonon wings due to pump-induced anharmonicity, compatible with a thermal origin. In contrast, the M region shows a persistent negative signal, indicating a pump-induced suppression of magnon scattering intensity and hence compatible with a pump-induced suppression of the long-range antiferromagnetic order.

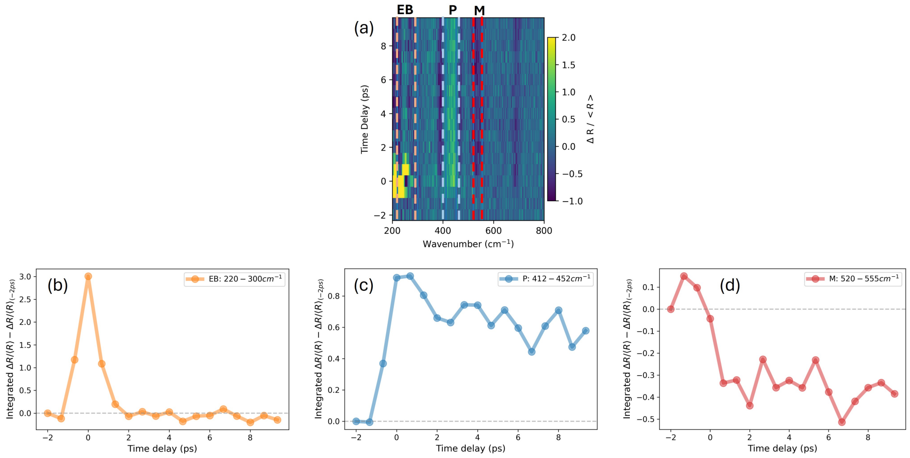

Figure 6.6: Temporal evolution of integrated TR Raman signals in three spectral regions. (a) TR map indicating the three integration ranges: electronic background (EB, orange), phonon region (P, light blue), and magnon region (M, red). (b) EB shows a strong broadband enhancement peaking at overlap and decaying within ~2 ps, consistent with transient electronic scattering. (c) P exhibits a long-lived positive signal up to 10 ps, suggesting enhanced continuum or broadened phonon wings. (d) M displays a persistent negative signal, indicating suppression of magnon scattering. The integrated signals are reported by computing the difference from their average value at negative times to clearly distinguish the induced effects from the pump.

Dyving in the M signal, another aspect we underline is that this M region is not limited to the two-magnon mode (Figure 6.7a). Indeed, without performing the preprocessing procedure (see Figure A.1), which normalizes the background, we can see that there is a quenching over a continuum of background between 500-750 cm^{-1} (Figure 6.7b). This background is consistent with our previous findings (Figure 4.20), where under the two-magnon we have found a continuum of magnetic excitations, evidenced by its temperature dependence and by comparing it with [58].

Finally, rather than relying solely on integrated intensities, in the following sections we perform full spectral fitting at each delay to extract mode positions, linewidths, and amplitudes, enabling a more precise characterization of the transient lattice and magnetic dynamics.

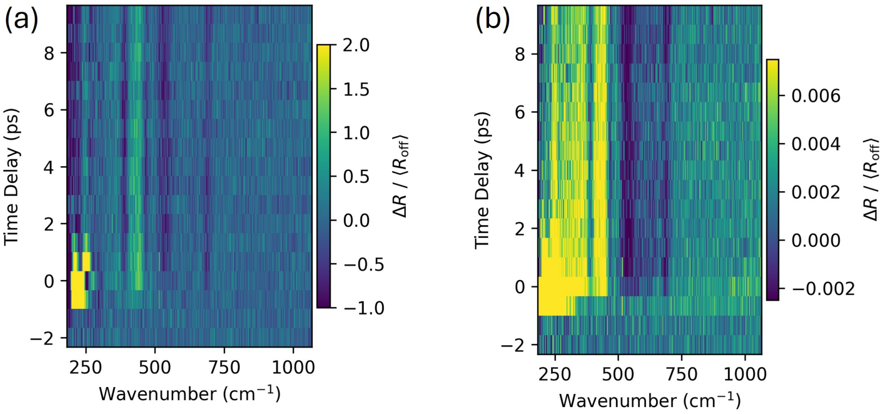

Figure 6.7: Pump-induced quenching of two-magnon background. (a) TR Raman map of Figure 6.4. (b) TR Raman map without the background processing. This comparison shows that the quenching of the two-magnon is extending over a broad continuum between 500–750 cm^{-1}, which is consistent with our previous findings (Figure 4.20), where we observe a continuum of magnetic excitations underlying the two-magnon feature, supported by its temperature dependence and by comparison with [58].

6.3.1.3 *Fit analysis of Raman modes*

We fit the average spectrum at each pump–probe delay with the pump at 700 nm (see an example of these spectra in Figure 6.5b-e). No additional background term was included because the spectra were already normalized following the same procedure used for the static measurements. Since the transient modes are broader than in the continuous-wave (CW) Raman spectra, we model each mode with a Gaussian profile. For each mode we extract the peak position, integrated intensity, and full width at half maximum (FWHM). The modes are summarized in Figure 6.2. We focus on the dynamics of P2 and P3 to clarify the origin of the positive signal (P) observed in the TR map, and on M2 to interpret the magnetic (M) response.

The main results for P2 and P3 are summarized in Figure 6.8. Figures (a) and (b) show the pump-induced peak shifts for P2 and P3, respectively, defined as $\Delta\Omega(t) = \Omega_{\mathrm{on}}(t) - \Omega_{\mathrm{off}}(t)$. Panels (c) and (d) report the corresponding FWHM changes, $\Delta\Gamma(t) = \Gamma_{\mathrm{on}}(t) - \Gamma_{\mathrm{off}}(t)$.

The trends indicate that P2 hardens (shift to higher energy), whereas P3 softens (shift to lower energy), with a larger response for P3. In particular, for positive delays the pump decreases the P3 frequency by up to ~ 3 cm^{-1}, and this softening persists for the entire 10 ps window. In contrast, P2 shows a smaller hardening of about ~ 1.5 cm^{-1} that relaxes after ~ 5 ps. The energy shifts are accompanied by broadening of both modes (Figs. 6.8c–d): the pump induces a maximal broadening of up to ~ 12 cm^{-1} for P2 and ~ 4 cm^{-1} for P3. These effects quantitatively account for the positive signal between the two phonons in Figure 6.6: the combination of dynamic broadening and opposite shifts (P2 to higher energy, P3 to lower energy) increases the spectral weight in the intermediate region.

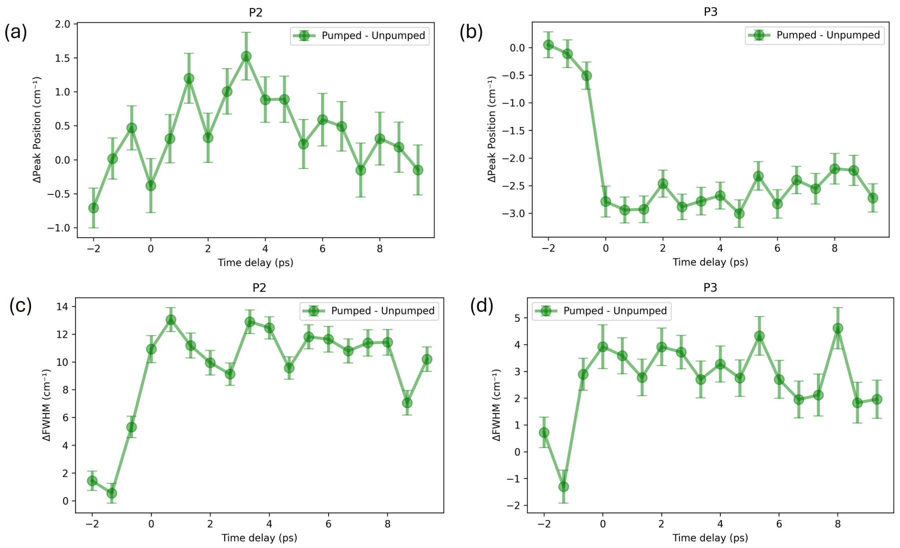

Figure 6.8: Pump-induced evolution of P2 and P3. (a,b) Peak shifts $\Delta\Omega(t) = \Omega_{\mathrm{on}} - \Omega_{\mathrm{off}}$ for P2 and P3. (c,d) FWHM changes $\Delta\Gamma(t) = \Gamma_{\mathrm{on}} - \Gamma_{\mathrm{off}}$ for P2 and P3. P2 hardens weakly and broadens, while P3 softens more strongly and also broadens.

The intensities of P2 and P3 both decrease under resonant pumping (Figures. 6.9a–b). To clarify the mechanism, we compar the ratio I_{P2}/I_{P3} to the same ratio obtained from the static temperature scan (Figure 4.26). The time-resolved ratio is plotted in Figure 6.9(c), while the static temperature dependence is shown in Figure 6.9(d). The ratio for the unpumped spectra matches the static value, whereas for the pumped spectra it drops to a lower value during temporal overlap and then remains approximately constant at positive delays.

The pump-induced change of the intensity ratio is compatible with the thermal evolution of the phononic modes observed in the temperature-dependent Raman spectra. This is consistent with a transient increase of the lattice temperature induced by the 700 nm $d-d$ resonant excitation.. By comparing the absolute ratio to the static results, we estimate a transient temperature rise of approximately ~ 20 K.

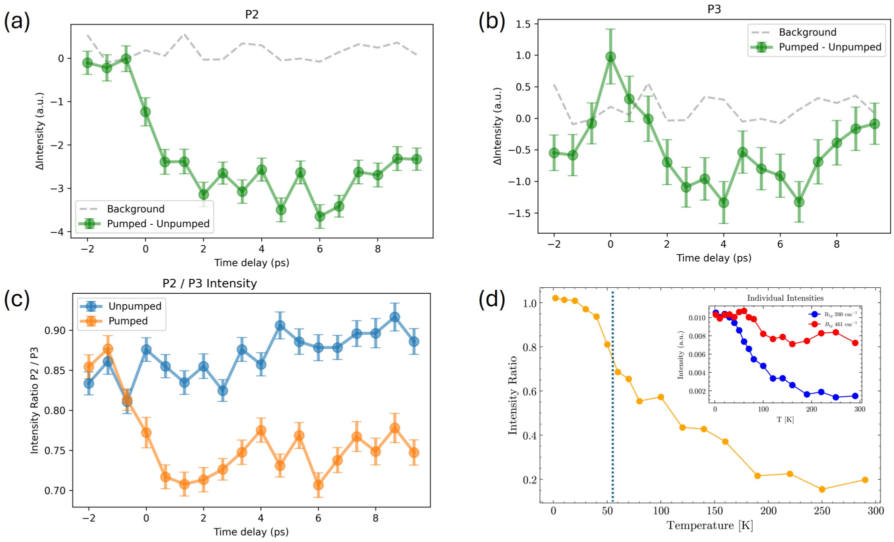

Figure 6.9: Pump-induced phonon intensities and intensity ratio of P2 and P3. (a,b) Differential intensity of the P2,P3 modes. It is noticeable that the pump induces an intensity decrease for P2 and P3. (c) Intensity ratio I_{P2}/I_{P3}. (d) Static temperature dependence of I_{P2}/I_{P3} for comparison (adapted by Figure 4.26). The blue dotted line shows the temperature at which the static measurement has the same intensity ratio of the pumped spectra for positive times in (c). The pump-induced change of the intensity ratio mirrors the trend in the static, temperature-dependent measurements, consistent with a transient increase of lattice temperature. By comparing the absolute ratio to the static results, we estimate a transient temperature rise of the lattice of approximately ~ 20 K.

For the M2 mode, the intensity results are shown in Figure 6.10. Under our pump conditions this mode is suppressed to the background level, estimated as the average signal in the 750–800 cm^{-1} window. This indicates that the pump strongly perturbs the magnetic excitations and effectively extinguishes the two-magnon feature within our signal-to-noise ratio. Similar pump-induced softening and broadening of magnonic excitations have been reported in time-resolved spontaneous Raman studies [36].

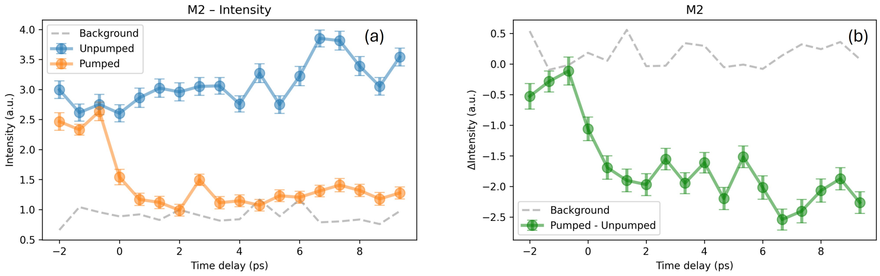

Figure 6.10: Suppression of the M2 mode. (a) Time dependence of the M2 intensity of pumped and unpumped spectra compared to the baseline estimated from 750–800 cm^{-1} and in (b) its corresponding differential intensity. The pump strongly perturbs the magnetic excitations and effectively extinguishes the two-magnon feature within our signal-to-noise ratio.

6.3.2 *Off Resonance Excitations: Pump at 2000 nm*

6.3.2.1 *Pump-Probe Measurements*

Similarly to the analysis with a pump at 700 nm, we perform pump-probe experiments with differential detector and lock-in in order to characterize the sample's transient optical response at 1.8 K, with the pump beam operating at 2000 nm. The only difference between these experimental conditions and those for the 700 nm pump-probe measurements, as reported in Figure 6.3, is the pump fluence, which is in the mJ/cm^2, range instead of µJ/cm^2. This is reasonable because the optical conductivity typically decreases with increasing wavelength (Figure 6.1).[2]

The results are summarized in Figure 6.11. Panel (a) shows the differential reflectivity, ΔR, normalized to its maximum value for the selected pump powers. The presence of an acoustic phonon is again observed at higher pump powers. In panel (b), the integrated signal of the curves from panel (a) is plotted against pump power. The integrated transient reflectivity change increases linearly with pump power, indicating that the experiment was conducted in the linear excitation regime. These conditions were maintained for subsequent measurements.

---

[2] Additionally, since the average powers are measured before the optical windows of the cryostat, the windows and air might absorb more in this frequency range and therefore lead an effective fluence into the sample less than what actually reported.

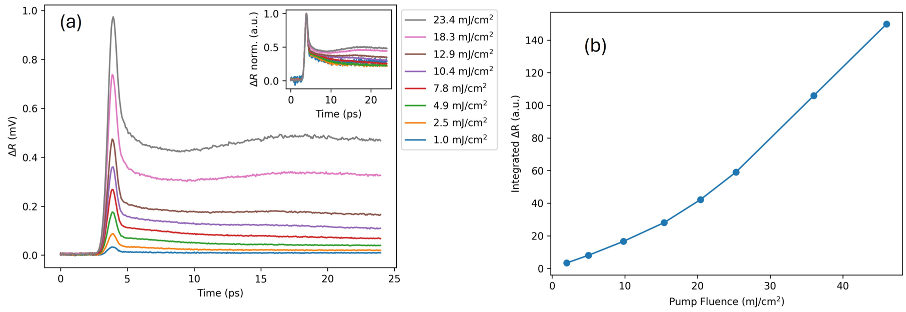

Figure 6.11: Pump–Probe measurements at 1.8 K with a 2000 nm pump and 532 nm probe (ps) in B_{1g} geometry. (a) Transient reflectivity change ΔR as a function of pump–probe time delay for various pump fluences. In the inset, the traces are normalized to their maximum amplitude. At higher pump powers, a sinusoidal modulation appears, attributed to a coherent acoustic phonon mode. (b) Integrated ΔR from (a) plotted versus pump fliuence, showing a linear dependence, consistent with operation in the linear excitation regime without significant nonlinear optical effects.

6.3.2.2 *Time-resolved Spontaneous Raman Measurements*

Under the same excitation conditions used in the pump–probe study, we perform time-resolved spontaneous Raman measurements. Each Raman spectrum was acquired with an integration time of 60 s, averaging 40 scans. The stage step of the ps path was set to 0.1 mm, as for the previous measurements performed with the pump at 700 nm (Figure 6.4). We first perform a pump–probe experiment and set the pump fluence to $23.4 mJ/cm^2$, producing a transient reflectivity signal of approximately 1.1 mV at temporal overlap, which correspond to the same transient reflectivity observed with the resonant 700 nm at the overlap.

Figure 6.12(a) presents the TR Raman map in the range 200–800 cm^{-1} for time delays from -2 ps (before pump arrival) to $+10$ ps after excitation. Figure 6.12(b) shows the corresponding pump–probe trace. The map shows neither the strong, short-lived low-energy response at temporal overlap nor the longer-lived positive feature at positive delays that are observed for 700 nm (Figure 6.4a). This is consistent with off-resonant pumping at 2000 nm, which does not resonantly excite the 4d-orbital transition (Figure 6.1). Importantly, however, a sizeable negative signal persists in the M region at positive delays.

By integrating the intensity over this spectral window (Figure 6.6), we find a clear negative signal emerging for $t+2$ ps (Figure 6.13). Curves are referenced to the average value at negative times to isolate pump-induced changes. By contrast, the EB and P regions show no significant response. Taken together with the results in Figure 6.6, this indicates that when the system is pumped off resonance the electronic background and phonons are essentially unperturbed, whereas the magnetic sector is suppressed. To address this phenomenon, we fit the individual Raman modes in the following section.

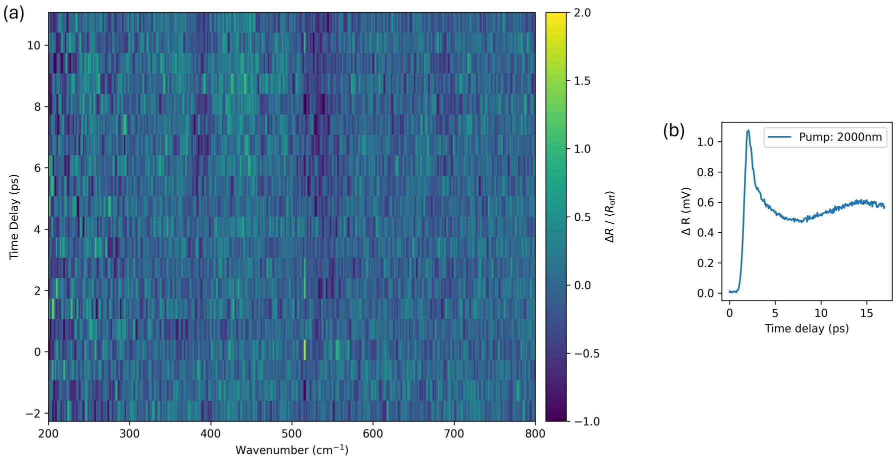

Figure 6.12: Time-resolved spontaneous Raman map and pump–probe trace at 2000 nm. (a) TR Raman map in the range 200–800 cm^{-1} for pump–probe delays from -2 ps to $+10$ ps. The color scale represents the normalized differential signal $(\langle R_{\mathrm{on}}\rangle - \langle R_{\mathrm{off}}\rangle)/\langle R_{\mathrm{off}}\rangle$. In contrast to the 700 nm case, the map shows no strong, short-lived low-energy response at temporal overlap and no longer-lived positive feature at later delays, consistent with off-resonant pumping. (b) Corresponding pump–probe transient reflectivity trace under the same experimental conditions. Measurements were performed at 1.8 K in the B_{1g} geometry.

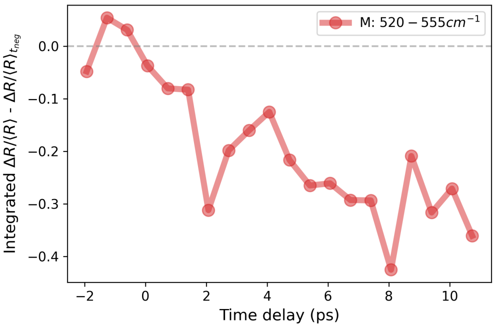

Figure 6.13: Temporal evolution of the integrated M region. Integrated intensity of the M region referenced to its average at negative delays. A persistent negative signal is observed for positive delays, indicating a suppression of magnon scattering even when the system is pumped off resonance at 2000 nm.

6.3.2.3 *Fit analysis of Raman modes*

We fit the Raman modes as in Section 6.3.1.3. To quantitatively compare with the 700 nm case in Figure 6.8, we report the pump-induced peak shift and

FWHM change for P2 and P3 in Figure 6.14. No abrupt energy shift is observed at temporal overlap (a-b); the maximal changes are $\sim +1$ cm^{-1} for P2 and ~ -1.5 cm^{-1} for P3. Relative to Figure 6.8(a)–(b), the amplitudes are reduced by $\sim$ 50%. Only P2 exhibits a clearly resolved shift immediately after overlap; for P3 the change is within the error bars. The signs match the 700 nm case—P2 hardens while P3 softens—consistent with the P-region signal in Figure 6.6(a). P2 relaxes by $\sim +5$ ps, similar to Figure 6.8(a).

From Figure 6.14(c)–(d), there is no clear trend of broadening in the FWHM changes, in contrast to the 700 nm case.

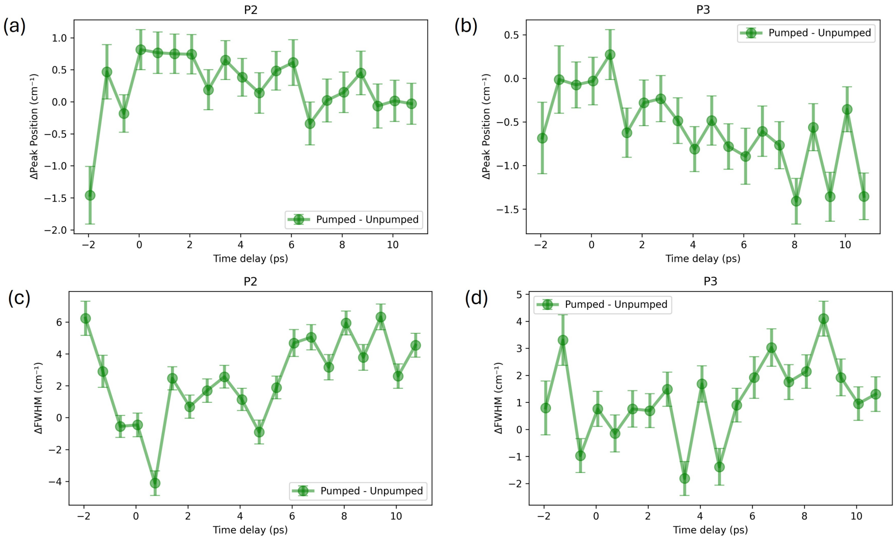

Figure 6.14: Pump-induced evolution of P2 and P3 at 2000 nm. (a,b) Peak shifts $\Delta\Omega(t) = \Omega_{\text{on}} - \Omega_{\text{off}}$ for P2 and P3. (c,d) FWHM changes $\Delta\Gamma(t) = \Gamma_{\text{on}} - \Gamma_{\text{off}}$ for P2 and P3. P2 hardens weakly while P3 softens weakly; no clear broadening trend is observed. Compared with 700 nm (Figure 6.9), the overall energy shifts are reduced by approximately 50%.

We use the intensity ratio I_{P2}/I_{P3} as a qualitative lattice thermometer, as in Figure 6.9. The results in Figure 6.15 show that the ratio for the pumped spectra does not decrease at positive delays; instead, it follows the same trend as the unpumped spectra. This supports the conclusion that there is no measurable increase in the lattice temperature at 2000 nm. By comparison with Figure 6.9(c)–(d), this suggests that the 700 nm pump is resonantly absorbed and couples strongly to the lattice (and electronic system), while the 2000 nm pump is off-resonant/weakly absorbed, therefore producing negligible lattice heating.

To quantify the negative signal in the M region (Figure 6.13), we perform the same analysis as in Figure 6.10. The results are shown in Figure 6.16. We observe that the pump induces a decrease of the two-magnon intensity; however,

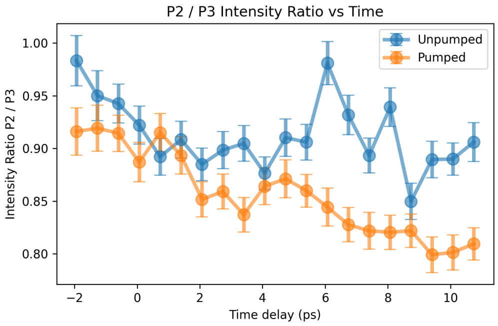

Figure 6.15: Intensity ratio of P2 and P3. Intensity ratio I_{P_2}/I_{P_3} for unpumped (blue) and pumped (orange) spectra. The lack of a systematic change at positive delays indicates no appreciable lattice heating at 2000 nm, in contrast to the resonant 700 nm case (Figure 6.9c).

in contrast to the 700 nm case, the mode is not completely quenched. Since no lattice-temperature increase is detected via P2/P3, this points to a non-thermal origin of the suppression.

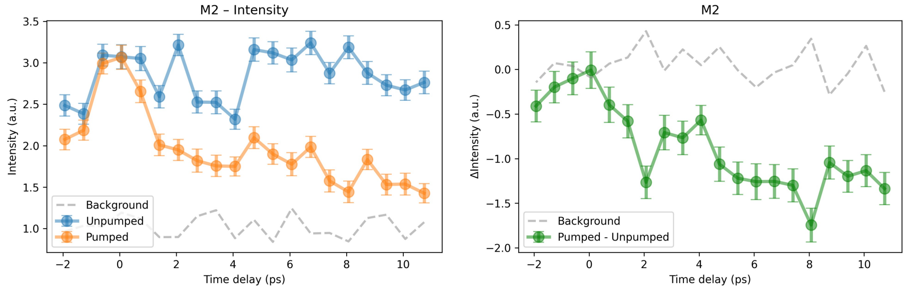

Figure 6.16: Pump-induce decrease of M2 intensity. Time dependence of the M2 intensity of pumped and unpumped spectra compared to the baseline estimated from 750–800 cm^{1}. A clear pump-induced reduction of the M2 intensity is observed for positive delays, but the mode is not fully quenched, in contrast to the 700 nm case.

One possible explanation is a pump-induced, non-thermal reduction of short-range AF correlations, as reported for the insulating compound $YBa_2Cu_3O_{6.1}$ in [95]. Such a mechanism modifies the exchange J and the correlation length ξ, which would affect the two-magnon energy [72] and linewidth. However, as shown in Figure 6.17(a)–(b), no significant shift or broadening is resolved within our error bars. Another possibility is a renormalization of J predicted for a high-frequency, nonresonant drive in time-resolved Raman [96][3]. In that scenario [96], a measurable shift of the two-magnon (2M) energy is expected,

$$\omega_{2M} \simeq \omega_{2M}(0)\, C(I, \lambda),$$

---

[3] The system used as test is a single-band Hubbard model on a square lattice in the large-U limit, mapping to a Heisenberg AF. The drive renormalizes J via a periodic (time-dependent) field.

where $\omega_{2M}(0)$ is the equilibrium (unpumped) value, I is the pump intensity, λ is the pump wavelength, and $C(I, \lambda)$ is a dimensionless renormalization factor that contains material-specific constants (see Eq. (28) in [96]). However, no such shift is clearly resolved in our data (Figure 6.17). Further studies and considerations are needed in order to understand the deeper nature of this feature.

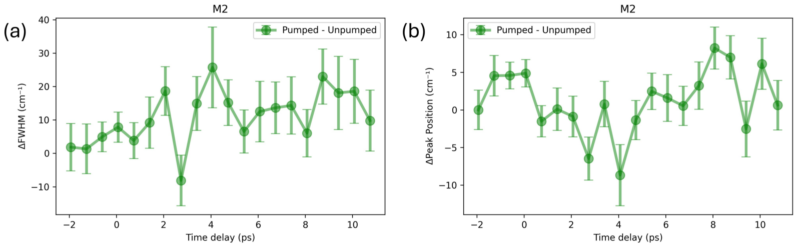

Figure 6.17: M2 peak shift and linewidth at 2000 nm. (a) Peak shift $\Delta\Omega_{M2}(t) = \Omega_{on} - \Omega_{off}$ referenced to negative delay. (b) FWHM change $\Delta\Gamma_{M2}(t) = \Gamma_{on} - \Gamma_{off}$. Within uncertainties, neither a systematic energy shift nor a broadening is resolved, indicating that the off-resonant pump suppressing of the M2 intensity is not primarily due to a change of the exhange constant J or the spin-correlation length ξ.

6.3.3 *Pump Wavelength Dependence*

6.3.3.1 *Time-resolved Spontaneous Raman Measurements*

To disentangle how the pump photon energy controls the time-resolved Raman (TR) response, we repeat the measurement for different pump wavelength across the $d-d$ orbital transitions of the Ru atoms. In particular, we use $\lambda_{\text{pump}} = 750$, 800, 850, and 1500 nm, in addition to the 700 and 2000 nm cases discussed above.[4] At each wavelength we adjust the pump fluence to reproduce the same peak pump–probe signal at temporal overlap ($\Delta R \simeq 1.1$ mV). To do that, we use 61.1, 177.7, 163 µJ/cm² for $\lambda_{\text{pump}} = 750$, 800, 850 nm, while 15.3 J/cm² for $\lambda_{\text{pump}} = 1500$ nm. Pumped and unpumped spectra were normalized as in the static measurements and the TR signal is reported as $(\langle R_{\text{on}}\rangle - \langle R_{\text{off}}\rangle)/\langle R_{\text{off}}\rangle$. All of the other experimental conditions are the same as reported previously for the TR maps at 700 nm and 2000 nm.

Figure 6.18 compares the TR maps side by side. In particular, Figure 6.18(A)–(F) correspond to $\lambda_{\text{pump}} = 700, 750, 800, 850, 1500$, and 2000 nm, respectively. The phenomenology established for 700 nm—a prompt, broadband low-energy enhancement (EB), a longer-lived positive signal in the phonon window (P), and a negative response in the magnon region (M)—persists across the near-IR, but its amplitude depends strongly on λ_{pump}. The response is clearly maximal at 750–800 nm, weakens at 850–1500 nm, and is strongly suppressed at 2000 nm.

To quantify this, we integrate the TR maps over the same three spectral windows used above (see Figure 6.6a). The average value at negative delays was subtracted in all cases. As summarized in Figures 6.19(a)-(b), the EB burst at overlap and the long-lived P signal both increase at 750–800 nm, while for λ_{pump} >850 nm exhibit a decrease of the integrated intensity. By contrast, the M signal remains negative at all wavelengths, including 1500 and 2000 nm, although with reduced magnitude off resonance (Figure 6.19c).

Two conclusions follow. First, the EB and P trends indicate a resonance-enhanced coupling when exciting with $\hbar\omega_{\text{pump}} \sim 1.55$–$1.65$ eV: even though this range does not coincide with the α or β maxima of the optical spectrum, as evidenced in Figure 6.19(d), it evidently optimizes the intermediate electronic states that mediate energy transfer to the low-energy Raman sector. This same window maximizes the pump-induced P2 hardening/P3 softening and the transient broadening (see fit analysis in Section 6.3.1.3). We highlight that the supression of the 2-magnon Raman resonance is present with both resonant and off-resonant excitations. This evidence may imply that the spin de-excitation is active even off-resonance with the $d-d$ orbital transitions.

Secondly, the persistence of a negative M signal for 1500–2000 nm pumps

---

[4] Energies (eV) are $E = 1240/\lambda(\text{nm})$: $700 \to 1.77$, $750 \to 1.65$, $800 \to 1.55$, $850 \to 1.46$, $1500 \to 0.83$, $2000 \to 0.62$.

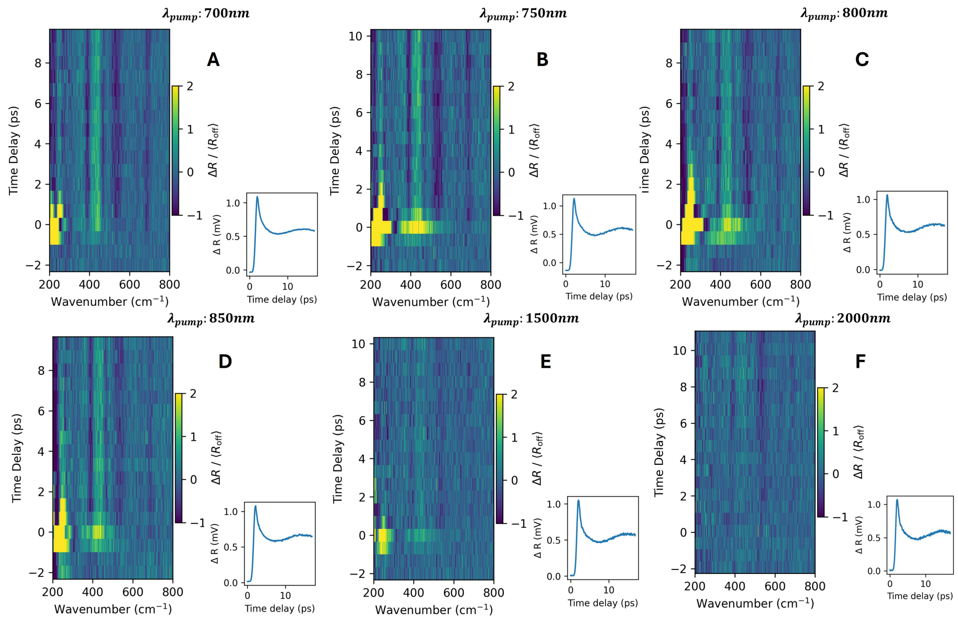

Figure 6.18: TR-Raman maps versus pump wavelength. Time-resolved Raman response ($\langle R_{on}\rangle - \langle R_{off}\rangle)/\langle R_{off}\rangle$ for $\lambda_{pump} = 700(A)$, $750(B)$, $800(C)$, $850(D)$, $1500(E)$ and $2000(F)$ nm. The prompt low-energy electronic background (EB) near temporal overlap and the longer-lived positive signal in the 412–452 cm^{-1} window (P) are both strongest at 750–800 nm, decrease at 850-1500 nm, and are strongly suppressed at 2000 nm. The magnon region (M, ~520–555 cm^{-1}) exhibits a negative signal at all wavelengths, with the largest amplitude near 750–800 nm. Pump fluences were adjusted at each wavelength to yield the same peak pump–probe amplitude (~1.1 mV) for a fair comparison, as shown by each corresponding pump-probe measurements at the bottom right of each TR map.

while EB and P are weak argues for a partly non-thermal route to suppress short-range AF correlations and/or modify exchange interaction J under off-resonant drive, whereas at 750–800 nm both thermal (lattice) and non-thermal contributions are active.

In addition, we evaluate the TR response by integrating the signals in Figure 6.19 over fixed time windows and plotting them as a function of pump photon energy. The EB region is integrated from ~ -1 to ~ 3 ps, while the P and M regions are integrated from ~ 3 to ~ 10 ps. The results, presented in Figure 6.20, are consistent with the trends discussed above. In particular, the EB contribution shows a pronounced resonance around 800 nm, which is an order of magnitude stronger than M and P. The P signal decreases steadily with increasing wavelength and is completely suppressed for $\lambda > 1500$ nm, whereas the M response persists at all pump energies, showing only a weak dependence on detuning (Figure 6.20b).

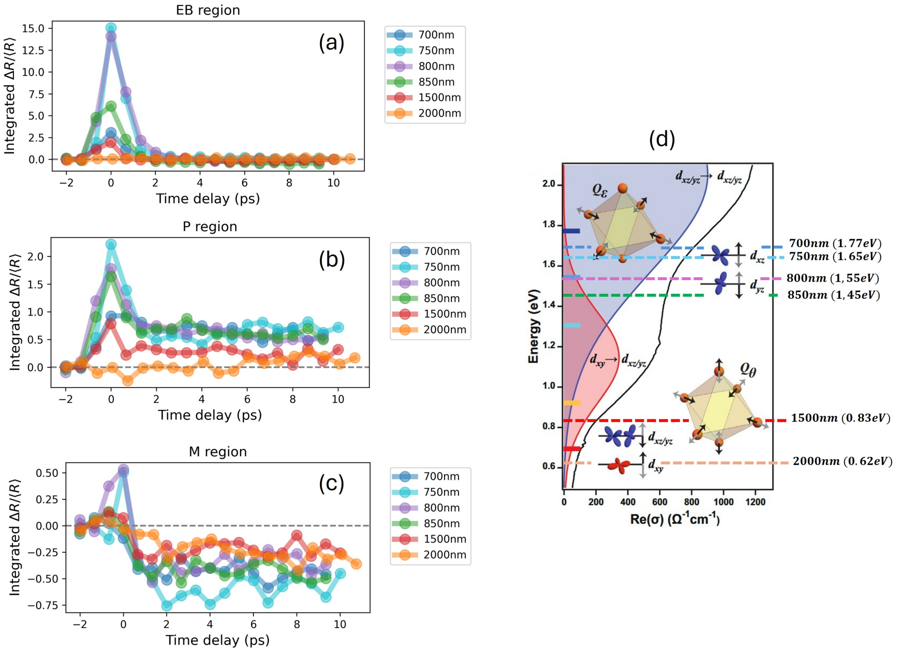

Figure 6.19: Integrated TR signals in fixed spectral regions. Panels (a)-(b)-(c) show temporal evolution of integrated TR Raman signal over EB (200–300 cm^{-1}), P (412–452 cm^{-1}), and M (520–555 cm^{-1}) for $\lambda_{\mathrm{pump}} = 700, 750, 800, 850, 1500,$ and 2000 nm. EB and P signals peak at 750–800 nm and decrease with detuning (850 nm → 2000 nm), while M remains negative at all wavelengths, including 1500 and 2000 nm, indicating a robust pump-induced suppression of the two-magnon intensity even off resonance with the $d - d$ transitions. The corresponding photon energies at the selected wavelengths are displayed in (d), on top of the absorption spectrum presented in Figure 6.1 [92].

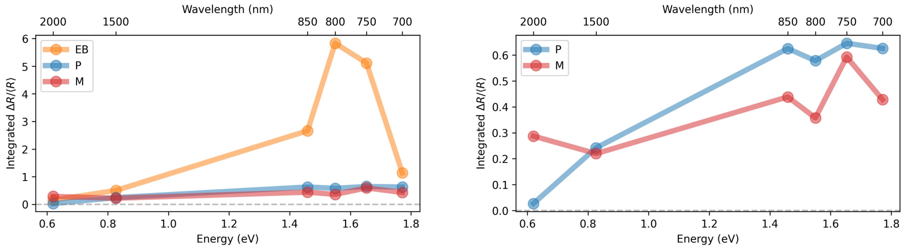

(a)

(b)

Figure 6.20: TR Raman signals of different spectral regions as a function of the pump energy. (a) Time-integrated TR signals from the EB, P, and M regions defined in Figure 6.19. EB is integrated from ∼ −1 to ∼ 3 ps, while P and M are integrated from ∼ 3 to ∼ 10 ps. (b) Same data as in (a), highlighting only the P and M contributions. The EB response displays a clear resonance near 800 nm, the P signal decreases with detuning and vanishes for $\lambda > 1500$ nm, while the M signal remains present at all pump energies, with only a weak dependence on resonance conditions.

SUMMARY AND OUTLOOK

The work presented in this thesis demonstrates the design, implementation, and application of a novel time-resolved spontaneous Raman (TRSR) platform to investigate complex quantum materials such as the ruthenate compounds. The main results achieved can be summarized as follows.

First, we developed a unique tunable TRSR setup, among the few of its kind worldwide. The system combines two independently tunable pump pulses with a picosecond tunable Raman probe, integrated with the acquisition system of a static Raman spectrometer. This platform not only enables single-color pump–probe experiments, but also extends the capabilities of conventional Raman spectroscopy into the time domain, allowing for direct access to the ultrafast dynamics of lattice, electronic, and magnetic excitations. We presented benchmark measurements on the phonon dynamics in Silicon to test the capability of our setup.

Second, we characterized the family of ruthenate compounds, $Ca_{2-x}Sr_xRuO_4$, through a systematic static Raman study. In Ca_2RuO_4 we identified clear magnetic features and found possible evidence of a spin–orbital transition. In the doped compounds with $x = 0.2$ and $x = 0.3$, we observed signatures of a structural phase transition from tetragonal to orthorhombic symmetry. Remarkably, for $x = 0.2$ this transition had not been previously reported in the literature, thus representing a novel contribution to the understanding of this system.

Third, we presented the first Raman experiments under external magnetic fields on the ruthenates. While no additional features were detected in Sr_2RuO_4, consistent with its absence of magnetic ordering, Ca_2RuO_4 exhibited striking new behavior. In particular, we identified a new B_{1g} Raman mode with a pronounced hysteretic behavior, whose temperature dependence points to a magnetic origin. Additionally, an A_g phonon mode displayed a Fano lineshape with hysteresis. Since its energy coincides with the amplitude (Higgs) mode associated with transitions between two magnetic ordered states, our results provide new insight into the behavior of the Higgs mode in Ca_2RuO_4 under a magnetic field applied along the c-axis, where canting is present.

Fourth, the first TRSR experiments in Ca_2RuO_4 revealed distinct relaxation channels depending on whether the antiferromagnetic state of Ca_2RuO_4 is excited resonantly or off-resonantly with respect to an optical transition. Resonant pumping led to a broadening of phonon modes, consistent with a transient lattice heating, an effect absent under off-resonant excitation. Similar behavior was observed in the electronic Raman response. Interestingly, the two-magnon mode behaved differently: in both resonant and off-resonant conditions, it exhibited a pronounced negative signal, a result that was unexpected for off-resonant excitation and points to unconventional relaxation dynamics of magnetic excitations.

In conclusion, this thesis establishes time-resolved spontaneous Raman spectroscopy as a powerful and versatile tool to probe the ultrafast dynamics of correlated materials. The combination of static, magnetic field-dependent, and time-resolved Raman studies on the ruthenates demonstrates the potential of TRSR to uncover new physical phenomena, from structural transitions to Higgs mode dynamics and out-of-equilibrium relaxation pathways.

OUTLOOK

This work opens a number of promising directions for future research.

On the methodological side, further optimization of the TRSR setup will be crucial. Until now, the system has been optimized for a Raman probe centered at 532 nm using narrowband filters. A natural next step is to extend the filtering scheme by implementing a folded grating-based pulse shaper [36], which can serve as a tunable spectral filter for the Raman probe, thereby eliminating the need to swap fixed filters.

On the materials side, several directions appear particularly compelling:

- **Ruthenates.** The spin–orbital transition in Ca_2RuO_4 and the newly identified structural transition in $Ca_{2-x}Sr_xRuO_4$ at $x = 0.2$ deserve closer examination. In particular, new compounds in the range $0 < x < 0.2$ could help track the temperature dependence of this structural transition and refine the phase diagram (Figure 3.6). Combining these Raman studies with transport measurements would fill an important gap in the literature.

- **Higgs mode.** The hysteretic behavior of the Higgs mode observed in Ca_2RuO_4 calls for further theoretical studies of how excitonic magnetism [57] is influenced by an external magnetic field. Raman spectroscopy is uniquely positioned to reveal both the symmetry and dynamics of such modes. In particular, the Fano asymmetry parameter could be used as a case study for detecting Higgs modes in 2D antiferromagnets [58, 89]. A theoretical analysis of the two-magnon density of states would also clarify whether the emergence of a new B_{1g} mode is expected.

- **Two-magnon dynamics.** The unexpected off-resonant behavior of the two-magnon response in Ca_2RuO_4 points to new, unexplored mechanisms of magnetic relaxation. These merit both experimental and theoretical work. Future measurements on both Stokes and anti-Stokes sides would allow us to distinguish thermal from non-thermal effects, as suggested by the two-magnon decay.

The TRSR setup also enables re-examining static results from a new perspective. For example: what is the dynamics of the Higgs mode, and does it behave similarly to the two-magnon when pumped on and off resonance? Assuming similar optical property, if we pump resonantly at the α peak in Ca_2RuO_4, which is particularly sensitive to tetragonal distortion (Figure 6.1), could we induce measurable modifications of the structural transition temperature observed in the doped compounds?

Beyond ruthenates, TRSR is well positioned to address emerging frontiers in light–matter interactions in quantum materials. For instance, it could probe selective photoexcitation of dd electronic transitions in the antiferromagnet TiOCl [97], investigate two-magnon behavior on and off resonance in $RbNiF_3$ [98, 99], or follow the non-equilibrium population dynamics during photoinduced superconducting melting in unconventional superconductors [22]. Furthermore, TRSR could be crucial to track effective temperatures in cavity quantum materials. For example, as shown in [11], light–matter coupling can modify the metal–insulator transition (MIT) temperature T_{MI}. Could similar effects be expected in the MIT of the ruthenate phase diagram (Figure 3.6) thereby for dopings with $x < 0.1$?

In this perspective, TRSR provides not only a new experimental window into the ultrafast dynamics of quantum materials but also a potential bridge between equilibrium spectroscopy and light-driven control of matter. Its continued development and application promise to illuminate some of the most pressing questions in condensed matter physics.

A

RAMAN SPECTRA PROCESSING

In this section, the background changes of the Si spectra are underlined using the pre-processing in [30], which consists of cosmic-ray removal, Gaussian filtering, baseline correction with Asymmetric Least Squares, and normalization to the area under the curve. The Raman spectra presented here are a zoom-in of the spectra shown in Figure 2.4 in the windows $\pm(100-500)\,\mathrm{cm}^{-1}$ and $\pm(550-900)\,\mathrm{cm}^{-1}$. The results are displayed in Figure A.1(a) for the Stokes side and in Figure A.1(b) for the anti-Stokes. This process is always applied to the Raman spectra in this thesis unless explicitly stated.

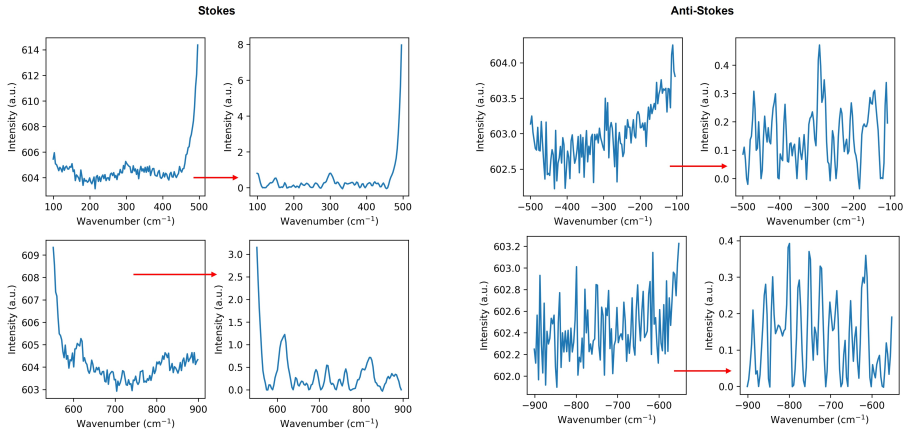

(a) (b)

Figure A.1: Example pre-processing procedure in Si. A zoom-in of the background regions $\pm(100-500)\,\mathrm{cm}^{-1}$ and $\pm(550-900)\,\mathrm{cm}^{-1}$ of the Raman spectra shown in Figure 2.4 is presented. Red arrows indicate the resulting spectra after the pre-processing procedure [30], which consists of cosmic-ray removal, Gaussian filtering, baseline correction with Asymmetric Least Squares, and normalization to the area under the curve. Panel (a) shows the Stokes side, and panel (b) displays the anti-Stokes.

B

STATIC RAMAN SETUP COUPLED TO THE TIME-RESOLVED SETUP

In this section, we present the scheme showing how the Static Raman setup described in Sect. 2.1 is coupled to the tunable Time-Resolved version described in Sect. 2.2. A translational stage is used to easily shift the two beamsplitters and therefore permits to the CW beam to easyly goes into the optical microscope.

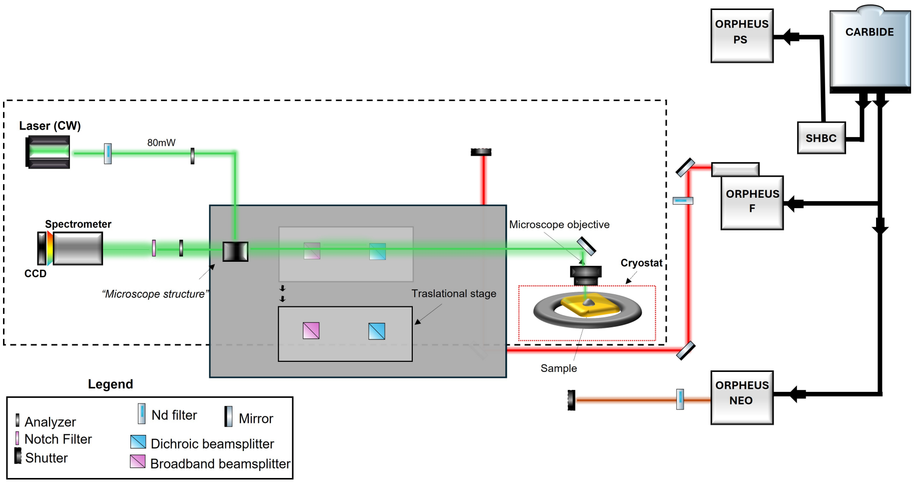

Figure B.1: Scheme of the Static Raman setup coupled to the Time-Resolved version. A translational stage is used to easily shift the two dichroic beamsplitters.

C

ANOMALOUS BEHAVIOR IN I-V MEASUREMENTS

Fig.C.1(a)-(b) displays the Voltage versus current measurements performed by Antonio Vecchione et al. for the doped samples with $x = 0.3$ and $x = 0.2$, respectively. The measurements are taken at different temperatures, from 77K to room temperature.
Fig.C.1(a) shows a characteristic metallic behavior for the entire set of temperatures, while Fig.C.1(b) presents a dome in the temperature range from 77 K to 140 K, which is typical in the Ca_2RuO_4 mott-insulator [100].
Moreover, the sample with $x = 0.2$ exhibits a metallic behavior for T200K, similar to the one observed in the $x = 0.3$ sample in Fig.C.1(a) for the entire set of temperatures. Although the phase diagram in Fig.4.16 predicts insulating behavior only for the samples with $0 < x < 0.2$, it is notable that the sample with $x = 0.2$ still present insulating behavior below 200 K.
Considering $T' \approx 140K$ as the temperature at which is present the transition between insulating and metallic state in the doped sample with $x = 0.2$, we try to compare it with $T_0 \approx 250K$ (see Figure 4.32 in Chapter 4). The difference between the two temperatures is approximately $\approx 110K$.
However, one possible suggestion is that these two behaviors are linked, as the metal-insulator transition in Ca_2RuO_4 is accompanied by a structural deformation [52]. Following this idea, in Fig.C.1(a) is not present any insulating behavior because the T' should be less than 77K measured ($T' \approx 180K - 110K = 70K$).
These considerations need further investigations, including measuring the I-V curve of x=0.3 at lower temperatures and trying to repeat the Raman measurements and I-V curves for the doping x=0.1, which has a metal-insulator transition [59].
Moreover, the samples used for the Raman measurements are not the same used in the I-V measurements. In order to compare better the results, it should be better to use the same samples and see if we measured the same features.

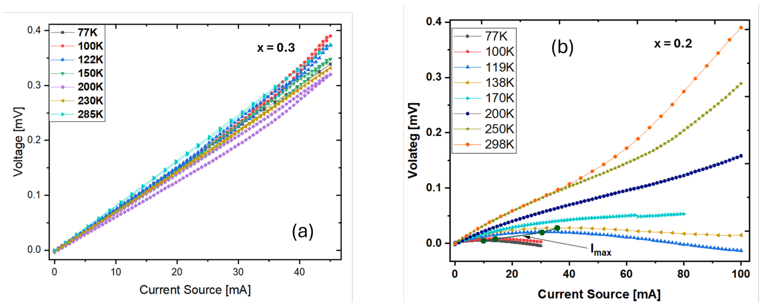

Figure C.1: Voltage versus current measurements for the doped samples from 77K to room temperature. The measurements are performed by Antonio Vecchione et al. (a) shows the metallic behavior of the doping with x=0.3 for the entire range of temperatures; (b) presents the results for x=0.2, which has a dome for $77K < T < 140K$, which is typical for the insulating phase of Ca_2RuO_4 [100]. For higher temperatures the x=0.2 doping exhibits similar metallic behavior of x=0.3. Further investigations are needed in order to understand if this behavior might be related with the structural transition observed in the Raman measurements (Chpater 4).

BIBLIOGRAPHY

[1] The Nobel Foundation. *The Nobel Prize in Physics 1930*. `https://www.nobelprize.org/nobel_prizes/physics/laureates/1930/`. Awarded to C. V. Raman “for his work on the scattering of light and for the discovery of the effect named after him”. 1930.

[2] Daniele Fausti, Riccardo I. Tobey, Nicole Dean, Stefan Kaiser, Alexander Dienst, Marie C. Hoffmann, Sung-Jin Pyon, Takasada Takayama, Hidenori Takagi, and Andrea Cavalleri. “Light-induced superconductivity in a stripe-ordered cuprate.” In: *Science* 331.6014 (2011), pp. 189–191.

[3] Wanzheng Hu, Stefan Kaiser, Daniele Nicoletti, Craig R. Hunt, Isabella Gierz, Marie C. Hoffmann, Matthieu Le Tacon, Toshinao Loew, Bernhard Keimer, and Andrea Cavalleri. “Optically enhanced coherent transport in YBa2Cu3O6.5 by ultrafast redistribution of interlayer coupling.” In: *Nature Materials* 13.7 (2014), pp. 705–711.

[4] Matteo Mitrano et al. “Possible light-induced superconductivity in K3C60 at high temperature.” In: *Nature* 530.7591 (2016), pp. 461–464.

[5] Tomás F. Nova, Andrea Cartella, Andrea Cantaluppi, Roman Mankowsky, Aitor Ferrer, Michael Först, and Andrea Cavalleri. “Metastable ferroelectricity in optically strained SrTiO3.” In: *Science* 364.6445 (2019), pp. 1075–1079.

[6] Alexandre Marciniak, Dominik M. Juraschek, Michael Fechner, Paolo Andrich, Michael Buzzi, Michael Först, Roman Mankowsky, and Andrea Cavalleri. “Vibrational coherent control of localized d–d electronic excitation.” In: *Nature Physics* 17.3 (2021), pp. 368–373.

[7] Z. Zeng, M. Först, M. Fechner, M. Buzzi, E. Amuah, C. Putzke, P. J. W. Moll, D. Prabhakaran, P. Radaelli, and A. Cavalleri. “Photo-induced chirality in a non-chiral crystal.” In: *Science* 387 (2025), pp. 431–436.

[8] Frank Schlawin, Dante M. Kennes, and Michael A. Sentef. “Cavity quantum materials.” In: *Applied Physics Reviews* 9.1 (2022), p. 011312.

[9] I-Te Lu, Dongbin Shin, Mark Kamper Svendsen, Hannes Hübener, Umberto De Giovannini, Simone Latini, Michael Ruggenthaler, and Angel Rubio. “Cavity-enhanced superconductivity in MgB2 from first principles quantum electrodynamics (QEDFT).” In: *Proceedings of the National Academy of Sciences* 121.5 (2024).

[10] Wonshik Ahn, Juan Felipe Triana, A. Eugene DePrince, Joel Yuen-Zhou, and Renan F. Ribeiro. “Modification of ground-state chemical reactivity via light–matter strong coupling.” In: *Science* 380.6650 (2023), pp. 1165–1169.

[11] G. Jarc et al. “Cavity-mediated thermal control of metal-to-insulator transition in 1T-TaS2.” In: *Nature* 622 (2023), pp. 487–492.

[12] Adolf Smekal. “Zur Quantentheorie der Dispersion.” In: *Naturwissenschaften* 11.46 (1923), p. 873.

[13] C. V. Raman and K. S. Krishnan. “A New Type of Secondary Radiation.” In: *Nature* 121.3048 (1928), pp. 501–502.

[14] G. Landsberg and L. Mandelstam. “Eine neue Erscheinung bei der Lichtzerstreuung in Krystallen.” In: *Naturwissenschaften* 16 (1928), pp. 557–558, 772–773.

[15] G. Placzek. “Rayleigh-Streuung und Raman-Effekt.” In: *Handbuch der Radiologie*. Ed. by E. Marx. Leipzig: Akademische Verlagsgesellschaft, 1934.

[16] H Kuzmany. *Solid-State Spectroscopy: An Introduction*. Springer Berlin Heidelberg, 2009.

[17] Daniele Fausti. “Phase transitions and optically induced phenomena in cooperative systems.” PhD thesis. University of Groningen, 2008.

[18] Anuja Sahasrabudhe. “Raman scattering on -RuCl under high magnetic fields: surprises of the field-induced phase.” Inaugural-Dissertation zur Erlangung des Doktorgrades der Mathematisch-Naturwissenschaftlichen Fakultät. Köln, Germany: Universität zu Köln, 2023.

[19] A. Zawadowski and M. Cardona. “Theory of Raman scattering on normal metals with impurities.” In: *Physical Review B* 42.16 (1990), p. 10732.

[20] Y. S. Ponosov and S. V. Streltsov. “Measurements of Raman scattering by electrons in metals: The effects of electron-phonon coupling.” In: *Physical Review B* 86.4 (2012), p. 045138.

[21] T. P. Devereaux and R. Hackl. “Inelastic Light Scattering From Correlated Electrons.” In: *Reviews of Modern Physics* 79.1 (2007), pp. 175–233.

[22] F. Giusti et al. “Signatures of Enhanced Superconducting Phase Coherence in Optimally Doped BiSrYCaCuO Driven by Midinfrared Pulse Excitations.” In: *Phys. Rev. Lett.* 122 (2019), p. 067002.

[23] T. Holstein and H. Primakoff. “Field Dependence of the Intrinsic Domain Magnetization of a Ferromagnet.” In: *Physical Review* 58 (1940), pp. 1098–1113.

[24] F. Bloch. “Zur Theorie des Ferromagnetismus.” In: *Zeitschrift für Physik* 61 (1930), pp. 206–219.

[25] Charles Kittel. *Introduction to Solid State Physics*. 8th ed. New York: Wiley, 2004.

[26] M. G. Cottam and D. J. Lockwood. *Light Scattering in Magnetic Solids*. New York: John Wiley & Sons, 1986.

[27] M. F. Thorpe. "Two-magnon Raman scattering and infrared absorption in MnF_2." In: *Journal of Applied Physics* 41.3 (1970), pp. 892–893.

[28] C. Castellani, F. Leoni, and C. R. Natoli. "A study of the two-magnon Raman scattering in the Heisenberg antiferromagnets CoF2 and FeF2 using a realistic model Hamiltonian." In: *Journal of Physics C: Solid State Physics* 7.7 (1974), p. 1353.

[29] *TriVista Additive Mode Scheme*. Accessed: 2025-09-05. URL: https://www.s-and-i.de/files/inhalte/Produkte/TriVista/TriVista-Detail_Additive-Mode.jpg.

[30] D. Georgiev et al. "RamanSPy: An Open-Source Python Package for Integrative Raman Spectroscopy Data Analysis." In: *Analytical Chemistry* 96 (2024), pp. 8492–8500.

[31] David Tuschel. "Raman thermometry." In: *Spectroscopy* 31.8 (2016).

[32] Shawn D. McGrane, David S. Moore, Peter M. Goodwin, and Dana M. Dattelbaum. "Quantitative Tradeoffs between Spatial, Temporal, and Thermometric Resolution of Nonresonant Raman Thermometry for Dynamic Experiments." In: *Applied Spectroscopy* 68 (2014), pp. 1279–1288.

[33] J. J. Gallardo, J. Navas, D. Zorrilla, R. Alcántara, D. Valor, C. Fernández-Lorenzo, and J. Martín-Calleja. "Micro-Raman spectroscopy for the determination of local temperature increases in TiO2 thin films due to the effect of radiation." In: *Applied Spectroscopy* 70 (2016), pp. 1128–1136.

[34] B. J. Kip and R. J. Meier. "Determination of the local temperature at a sample during Raman experiments using Stokes and anti-Stokes Raman bands." In: *Applied Spectroscopy* 44 (1990), pp. 707–711.

[35] D. Fausti and P. H. M. van Loosdrecht. "Time-Resolved Resonant Raman Spectroscopy." In: *Optical Techniques for Solid-State Materials Characterization*. Ed. by R. P. Prasankumar and A. J. Taylor. Boca Raton; London; New York: CRC Press, 2012. Chap. 14.

[36] R. B. Versteeg et al. "A tunable time-resolved spontaneous Raman spectroscopy setup for probing ultrafast collective excitation and quasiparticle dynamics in quantum materials." In: *Structural Dynamics* 5 (2018), p. 044301.

[37] D. Fausti, O. V. Misochko, and P. H. M. van Loosdrecht. "Ultrafast photoinduced structure phase transition in antimony single crystals." In: *Phys. Rev. B* 80 (2009), p. 161207.

[38] Y. Uesugi, Y. Mizutani, and T. Kitagawa. “Developments of widely tunable light sources for picosecond time-resolved resonance Raman spectroscopy.” In: *Review of Scientific Instruments* 68 (1997), pp. 4001–4008.

[39] M. Braden, A. H. Moudden, S. Nishizaki, Y. Maeno, and T. Fujita. “Structural analysis of Sr2RuO4.” In: *Physica C: Superconductivity* 273 (1997), pp. 248–254.

[40] M. Udagawa et al. “Phonon Raman scattering of SrRuO.” In: *Physica B: Condensed Matter* 219–220 (1996), 222–224.

[41] Bohm-Jung Kim, Sergey Khmelevskyi, Cesare Franchini, Igor I. Mazin, and Kwang Kim. “SrRuO–SrTiO heterostructure as a possible platform for studying unconventional superconductivity in SrRuO.” In: *Phys. Rev. B* 101 (2020), p. 220502.

[42] Y. Maeno, H. Hashimoto, K. Yoshida, et al. “Superconductivity in a layered perovskite without copper.” In: *Nature* 372 (1994), 532–534.

[43] Y. Maeno, S. Yonezawa, and A. Ramires. “Still Mystery after All These Years—Unconventional Superconductivity of Sr2RuO4.” In: *J. Phys. Soc. Jpn.* 93 (2024), p. 062001.

[44] Y. Maeno, A. Ikeda, and G. Mattoni. “Thirty years of puzzling superconductivity in Sr2RuO4.” In: *Nature Physics* 20 (2024), pp. 1712–1718.

[45] C. Bergemann, A. P. Mackenzie, S. R. Julian, D. Forsythe, and E. Ohmichi. “Quasi-two-dimensional Fermi liquid properties of the unconventional superconductor SrRuO.” In: *Advances in Physics* 52.7 (2003), 639–725.

[46] Z. V. Pchelkina et al. “Evidence for strong electronic correlations in the spectra of SrRuO.” In: *Phys. Rev. B* 75 (2007), p. 035122.

[47] H. Rho, S. L. Cooper, S. Nakatsuji, H. Fukazawa, and Y. Maeno. “Lattice dynamics and the electron–phonon interaction in CaRuO.” In: *Phys. Rev. B* 71 (2005), p. 245121.

[48] D. G. Porter et al. “Magnetic anisotropy and orbital ordering in CaRuO.” In: *Phys. Rev. B* 98 (2018), p. 125142.

[49] S. Nakatsuji, S. Ikeda, and Y. Maeno. “New layered perovskite ruthenates: CaRuO.” In: *Physica C: Superconductivity* 282–287 (1997), 729–730.

[50] M. Braden, G. André, S. Nakatsuji, and Y. Maeno. “Crystal and magnetic structure of CaRuO: Magnetoelastic coupling and the metal–insulator transition.” In: *Phys. Rev. B* 58 (1998), 847–861.

[51] P. Steffens et al. “High-pressure diffraction studies on CaRuO.” In: *Phys. Rev. B* 72 (2005), p. 094104.

[52] O. Friedt et al. “Structural and magnetic aspects of the metal–insulator transition in CaSrRuO.” In: *Phys. Rev. B* 63 (2001), p. 174432.

[53] Forte F. Romano A. Cuono G. and C. Noce. "Emerging new phases in correlated Mott insulator CaRuO." In: *Journal of Physics: Condensed Matter* 37 (2024), p. 053002.

[54] P. Steffens et al. "High-pressure diffraction studies on CaRuO." In: *Phys. Rev. B* 72 (2005), p. 094104.

[55] C. Cirillo et al. "Emergence of a metallic metastable phase induced by electrical current in CaRuO." In: *Phys. Rev. B* 100 (2019), p. 235142.

[56] I. Vergara et al. "Spin-orbit coupling and crystal-field splitting in Ti-doped CaRuO studied by ellipsometry." In: *Phys. Rev. B* 106 (2022), p. 085103.

[57] Giniyat Khaliullin. "Excitonic magnetism in Van Vleck–type d Mott insulators." In: *Phys. Rev. Lett.* 111 (2013), p. 197201.

[58] S.-M. Souliou et al. "Raman scattering from Higgs mode oscillations in the two-dimensional antiferromagnet CaRuO." In: *Phys. Rev. Lett.* 119 (2017), p. 067201.

[59] S. Nakatsuji and Y. Maeno. "Quasi-two-dimensional Mott transition system CaSrRuO." In: *Phys. Rev. Lett.* 84 (2000), 2666–2669.

[60] S. Acharya, D. Dey, T. Maitra, and A. Taraphder. "Quantum criticality associated with dimensional crossover in the iso-electronic series CaSrRuO." In: *Journal of Physics Communications* 2 (2018), p. 075004.

[61] Zhong Fang, Kiyoyuki Terakura, and Naoto Nagaosa. "Orbital physics in ruthenates: first-principles studies." In: *New Journal of Physics* 7 (2005), p. 66.

[62] T. C. Damen, S. P. S. Porto, and B. Tell. "Raman Effect in Zinc Oxide." In: *Phys. Rev.* 142 (1966), pp. 570–574.

[63] S. Sakita et al. "Anisotropic properties of the excitation spectrum of SrRuO crystals (Tc = 1.4 K) in the normal state investigated by Raman scattering." In: *Phys. Rev. B* 63 (2001), p. 134520.

[64] H. Rho, S. L. Cooper, S. Nakatsuji, H. Fukazawa, and Y. Maeno. "Raman scattering studies of spin, charge, and lattice dynamics in CaSrRuO (0 < x < 0.2)." In: *Phys. Rev. B* 68 (2003), p. 100404.

[65] H. Rho, S. L. Cooper, S. Nakatsuji, and Y. Maeno. "Second-order phase transition in: A Raman study." In: *Journal of Magnetism and Magnetic Materials* 310 (2007), e266–e268.

[66] C. S. Alexander et al. "Destruction of the Mott insulating ground state of CaRuO by a structural transition." In: *Phys. Rev. B* 60 (1999), R8422–R8425.

[67] S. Nakatsuji, T. Ando, Z. Mao, and Y. Maeno. "Metal–insulator transition in CaSrRuO." In: *Physica B: Condensed Matter* 259–261 (1999), 949–950.

[68] I. Zegkinoglou et al. “Orbital ordering transition in CaRuO observed with resonant x-ray diffraction.” In: *Phys. Rev. Lett.* 95 (2005), p. 136401.

[69] Andreas Raphael German. “Raman Spectroscopy on Selected Cooperative Systems.” PhD thesis. University of Köln, 2022.

[70] C. S. Snow et al. “Pressure-tuned collapse of the Mott-like state in CaRunO (n = 1, 2): Raman spectroscopic studies.” In: *Phys. Rev. Lett.* 89 (2002), p. 226401.

[71] W. Weber. “Adiabatic bond charge model for the phonons in diamond, Si, Ge, and –Sn.” In: *Phys. Rev. B* 15 (1977), 4789–4803.

[72] P. A. Fleury and R. Loudon. “Scattering of light by one- and two-magnon excitations.” In: *Phys. Rev.* 166 (1968), 514–530.

[73] Ugo Fano. “Effects of configuration interaction on intensities and phase shifts.” In: *Phys. Rev.* 124 (1961), 1866–1878.

[74] P. Nyhus, S. L. Cooper, and Z. Fisk. “Electronic Raman scattering across the unconventional charge gap in FeSi.” In: *Phys. Rev. B* 51 (1995), 15626–15629.

[75] J. D. Axe and G. Shirane. “Influence of the superconducting energy gap on phonon linewidths in NbSn.” In: *Phys. Rev. Lett.* 30 (1973), 214–216.

[76] P. B. Allen. “Neutron spectroscopy of superconductors.” In: *Phys. Rev. B* 6 (1972), 2577–2579.

[77] W. L. McMillan. “Transition temperature of strong-coupled superconductors.” In: *Phys. Rev.* 167 (1968), 331–344.

[78] T. Mizokawa et al. “Orbital state and metal–insulator transition in CaS-rRuO (x = 0.0 and 0.09) studied by x-ray absorption spectroscopy.” In: *Phys. Rev. B* 69 (2004), p. 132410.

[79] J.-C. Philippe et al. “Orbital dichotomy of Fermi liquid properties in SrRuO revealed by Raman spectroscopy.” In: *Phys. Rev. B* 103 (2021), p. 235147.

[80] G. Blesio, S. Beck, O. Gingras, A. Georges, and J. Mravlje. “Signatures of Hund metal and finite-frequency nesting in SrRuO revealed by electronic Raman scattering.” In: *Physical Review Research* 6 (2024), p. 023124.

[81] D. Vojna, O. Slezák, A. Lucianetti, and T. Mocek. “Verdet constant of magneto-active materials developed for high-power Faraday devices.” In: *Applied Sciences* 9 (2019), p. 3160.

[82] D. Vojna et al. “Faraday rotation of DyO, CeF and YFeO at the mid-infrared wavelengths.” In: *Materials* 13 (2020), p. 5324.

[83] D. Vojna et al. “Verdet constant of potassium terbium fluoride crystal as a function of wavelength and temperature.” In: *Optics Letters* 45 (2020), 1683–1686.

[84] *Faraday effect (illustration)*. Accessed: 2025-09-05. URL: `https://en.wikipedia.org/wiki/Faraday_effect#/media/File:Faraday-effect.svg`.

[85] K. Fürsich et al. "Raman scattering from current-stabilized nonequilibrium phases in CaRuO." In: *Phys. Rev. B* 100 (2019), p. 081101.

[86] C. Autieri, G. Cuono, D. Chakraborty, P. Gentile, and A. M. Black-Schaffer. "Conditions for orbital-selective altermagnetism in SrRuO: Tight-binding model, similarities with cuprates, and implications for superconductivity." In: *Phys. Rev. B* 112 (2025), p. 014412.

[87] S. Nakatsuji et al. "CaRuO: New Mott insulators of layered ruthenates." In: *J. Phys. Soc. Jpn.* 66 (1997), p. 1868.

[88] G. Cao, S. McCall, M. Shepard, J. E. Crow, and R. P. Guertin. "Magnetic and transport properties of single-crystal CaRuO: Relationship to superconducting SrRuO." In: *Phys. Rev. B* 56 (1997), R2916–R2919.

[89] A. Jain et al. "Higgs mode and its decay in a two-dimensional antiferromagnet." In: *Nature Physics* 13 (2017), 633–637.

[90] J. H. Jung et al. "Change of electronic structure in CaRuO induced by orbital ordering." In: *Phys. Rev. Lett.* 91 (2003), p. 056403.

[91] Z. Fang, N. Nagaosa, and K. Terakura. "Orbital-dependent phase control in CaSrRuO (0 < x < 0.5)." In: *Phys. Rev. B* 69 (2004), p. 045116.

[92] H. Ning et al. "A coherent phonon-induced hidden quadrupolar ordered state in CaRuO." In: *Nature Communications* 14 (2023), p. 8258.

[93] M.-C. Lee et al. "Abnormal phase flip in the coherent phonon oscillations of CaRuO." In: *Phys. Rev. B* 98 (2018), p. 161115.

[94] R. Liu et al. "Femtosecond pump–probe spectroscopy of propagating coherent acoustic phonons in InGaNGaN heterostructures." In: *Phys. Rev. B* 72 (2005), p. 195335.

[95] J.-A. Yang, N. Pellatz, T. Wolf, R. Nandkishore, and D. Reznik. "Ultrafast magnetic dynamics in insulating YBaCuO.1 revealed by time-resolved two-magnon Raman scattering." In: *Nature Communications* 11 (2020), p. 2548.

[96] Yao Wang, Thomas P. Devereaux, and Chunjing Chen. "Theory of time-resolved Raman scattering in correlated systems: Ultrafast engineering of spin dynamics and detection of thermalization." In: *Phys. Rev. B* 98 (2018), p. 245106.

[97] Montanaro Angela. "Non-equilibrium response of quantum materials to resonant low-energy electronic photo-excitations." PhD thesis. University of Trieste, 2021.

[98] Enrico Maria Rigoni. "Ultrafast non-equilibrium studies of complex materials through pump-probe and stochastic spectroscopies." PhD thesis. University of Trieste, 2023.

[99] Giovanni Tartaglia. "Studio dinamico delle eccitazioni a bassa energia in un campione di RbNiF3." MA thesis. University of Trieste, 2023.

[100] C. Cirillo et al. "Emergence of a metallic metastable phase induced by electrical current in CaRuO." In: *Phys. Rev. B* 100 (2019), p. 235142.

ACKNOWLEDGMENTS

"In this chapter we will explore the fascinating interplay of the spins, lattice..." ah no?

Alla fine (finalmente) eccoci qua.

Dopo tutto questo lavoro, non posso che ringraziarTI Daniele per tutto.

Ringraziarti per avermi dato questa possibilità sarebbe riduttivo... grazie per le diverse chiacchierate, da quelle scientifiche in cui mi hai trasmesso tutta la tua passione per la ricerca, a quelle in pausa caffè in cui mi hai dato nuovi punti di vista e massime di vita (come quella calcistica: "se vuoi giocare la domenica impara ad allenarti dal lunedì!"), oppure a quelle in cui mi parlavi schiettamente e in dialetto. Grazie per l'infinita pazienza e stima che hai avuto per me. Mi hai insegnato tanto.

Grazie Giacomo, perché senza di te nulla di tutto questo lavoro sarebbe stato possibile. Ti devo ringraziare perché con te ho imparato tantissimo. Magari non ti rendi conto, ma grazie a te mi porto a casa un bagaglio enorme, forse troppo pesante per fare le ferrate o camminate in Friuli che mi hai suggerito. Grazie per la pazienza e tempo dedicato, ma soprattutto grazie per la compagnia e sostegno nel "Kitbuuuuu-el", la lista infinita di meme, come i laser "Aldo, Giovanni, e Giacomo", oppure i miei typo in inglese che li hai resi storia, come i cavi (*caves*) e i *boarder pillar*. Sicuramente mi sarò dimenticato qualche meme (*Ullah!*). Sopra tutto, però, ti devo ringraziare per avermi insegnato un aspetto fondamentale: la RESILIENZA. Poi si sa, entrambi dobbiamo ringraziare due persone tra tutte: il maestro *Maeno* e il king *Bello Figo* ("quaaatro, duemila e quaatro... (...) ... oouh (..) no-ve—no-ve no-nna").

Grazie in particolare a tutto il team q4q, per me siete stati come una famiglia. Grazie Shala che tra una cosa e un'altra sono più le volte che ci incrociamo fuori a Trieste (tipo le riprese del film); Grazie Angela perché dal punto di vista scientifico ho continuato a imparare da te (anche solo per osmosi) sin dalla triennale, e dal punto di vista umano hai sempre avuto grande sensibilità; Grazie Enrico, anche solo perché probabilmente non ti avevo ringraziato a sufficienza alla tesi triennale ("e sì, il piacere di essere stato tuo studente è più che ricambiato!"); Grazie Antonio, perché alle volte sei stato un faro (non come la ciminiera) nella "ridente" cittadina di Erlangen. Grazie per avermi reso più leggero e spensierato il periodo in Germania ("a partire dalla focaccia di Bari... Ulah!"); Grazie Nitesh, per il sostegno e compagnia dei miei viaggi all'ultimo minuto (Colonia, Stoccarda, Bamberga) e per il "coding", abbiamo

una cena di "momo" in arretrato!; Grazie Costi e Barto, perché è stato bellissimo poter condividere il gruppo con due persone come voi, che prima della "Quantum Spectrosc...." per me siete stati (e rimarrete) amici dell' uni! Siete stati la ciliegina sulla torta di questo fantastico gruppo!
Ad Erlangen, devo ringraziare in particolare Ruth e Anni, che (non so come) avete valso la pena ritornare ad Erlangen!
Devo ringraziare poi tutte le persone di questi 5 anni di università, tra associazioni, eventi, calcetti, Cus, pause... grazie alle persone e amici del dip, chi alla triennale, chi alla magistrale, e chi ad entrambe. Mi avete fatto trascorrere 5 anni indimenticabili. Ringrazio per i meme di questi ultimi due anni e tutti i ragazzi del Real Matrix (insieme ai supporters) per i risultati importanti ottenuti ("due coppe chiosco!").
Di questi 5 anni, ci tengo in particolare a ringraziare Gaz, Ale e Sofi, che tra uno (o due) viaggi in Spagna (Ale e Sofi) e un calcetto o fanta (Gaz) siete stati sempre una costante per me a Trieste (anche te Simo anche se ora sei via).
Ci tengo a ringraziarti nuovamente Sofi, perché sei sempre stata presente (pur facendoti in quattro) e ti sei subita il mio stress pre-tesi (non una, ma ben due volte!). Un semplice grazie penso non basti a trasmetterti quanto tu sia stata (e sei) importante per me in questo viaggio.
Ringrazio Luke, Dave, e Anto: il legame che ho avuto con voi (e rimarrà tale) è più "fraterno" che di semplice "convivenza".
Passando a Vittorio, non posso che ringraziare tutti voi di Parkour, siete davvero degli amici speciali: sono molto fortunato ad avervi, siete una di quelle amicizie in cui il tempo è come se si fermasse.
Grazie a voi di "Dem". Anche se abbiamo smesso di fare musica assieme, siete stati cruciali per come ho vissuto questi 5 anni di uni.
Grazie Elena e Anna, che con una semplice chiamata mi siete state vicine in questo percorso.
Grazie Carlot perché sei così come sei, un' amica rara.
Grazie Andre e Grazie Simo, con voi non c'è bisogno di altre parole. Siete gli storici.
Grazie alla mia famiglia.

Grazie Mamma, Grazie Babbo, Grazie Ste. Voi siete stati casa e rifugio in questi anni. Non avete mai smesso di sostenermi e essermi vicino, anche nei miei momenti più di dubbio e confusione. Il più grande grazie non può che andare a voi. Non so quanto sia fortunato ad avervi, davvero.

Per finire, grazie Trieste per essere stata una splendida cornice per tutto questo. Sei l'unica città con cui mi emoziono ogni volta che arrivo, che sia dalla costiera o dall'obelisco. La tua *scontrosa grazia* si è trasformata in *caldo abbraccio* in questi ultimi 2 anni.

Mi piacerebbe finire con delle mie parole, dette un bel po' di anni fa, in cui non pensavo di rivedermi a distanza di tempo:

Corro corro col ninja, mettendo la quinta, tu sali dietro andiamocene da qui
Lascio la mia provincia, un pezzo del mio cuore, come fosse l'ultimo bacio alla Klimt
*Mi guardo dall'alto, penso ciò che ho fatto, sono soddisfatto merito a ~~due V~~**
Sono a studiare fisso qua a Trieste, viaggiare per fare ricerca è il mio dream

Ninja - Demiurgency (Gioskybeat)

*** tutti Voi, grazie**